Spatial behavior of whispering-gallery “wedge” mode in optical microcavities

陳, 聰

出版情報：九州大学, 2018, 博士（工学）, 課程博士
バージョン：
権利関係：

Doctoral Thesis

Jan. 2019

Spatial behavior of whispering-gallery "wedge" mode in optical microcavities

Graduate School of Information Science

and Electrical Engineering,

Kyushu University

Cong Chen

A Doctoral Thesis

submitted to Graduate School of Information Science and Electrical Engineering, Kyushu University

Cong Chen

Thesis Committee:

Professor Yuji Oki	(Supervisor)
Professor Kenshi Hayashi	(Co-Supervisor)
Professor Kazutoshi Kato	(Co-Supervisor)
Associate Professor Daisuke Nakamura	(Co-Supervisor)

Contents

List of Figures

List of Tables

Chapter 1

Introduction

1.1. Background and motivation

Laser (Light Amplification by Stimulated Emission of Radiation) science is a new research field which is developed since twentieth Century. It is an important achievement of modern physics, and a brilliant result of the combination of science and technology. As early as 1916, A. Einstein proposed the basic theory for supporting lasing phenomenon, but he did not achieve the light amplification by stimulated emission of radiation [1]. In 1946, Swiss scientist F. Block observed the signal of population inversion in experiments. Then, in 1953, C.H. Townes excited ammonia molecules to realize "Microwave Amplification By Stimulated Radiation (MASER)", which laid the foundation for light amplification in visible range [2–4].

After this, the American physicist T. H. Maiman developed the world's first laser based on these previous researches in 1960 [5–7]. From that time to the present, laser has been used for many devices including personal computer, audio equipment, printer, scanner, optical communication, spectroscopy, laser treatment, laser processing, etc. Nowadays laser has become an indispensable device

in our life.

Similar to the history of computer, the development of lasers are also evolving from the very first large type to miniaturization with high performance. The the applications of traditional huge laser generators are limited due to large size. Therefore, laser miniaturization is an urgent matter in front of our eyes. Generally, the laser consists of an excitation source, a medium and a resonator. Among these components, the resonator is directly related to the size of a laser. As a well-known resonator, a Fabry-Perot resonator is generally composed of two mirrors with high reflectivity [8–10]. Light waves are constantly reflected back and forth in the mirrors placed parallel to each other to achieve light amplification. Traditional lasers need a long distance of resonant to achieve light amplification in the visible wavelength, which directly leads to a large size.

On the other hand, since the first publication of Whispering Gallery, the research on the Whispering-Gallery Mode (WGM) microcavity become more and more active [11–15]. Different from the traditional Fabry-Perot cavity, the WGM microcavity amplifies light by locking light through total reflection on the boundary surface of a circular or spherical dielectric material [16–20]. Since optical losses are relatively low, such WGM microcavities usually have a high quality factor(Q-factor) [21–23], wide mode interval, small mode volume and so on. As representative of the widely studied WGM resonators, micro-3D geometries such as microspheres [24–26], microrings [27–29] and microdisks [30–32] are the mainstream structures.

Based on the excellent performance of such WGM microcavities, more and more studies focus on its derivative applications. For example, the low threshold laser [33–35], the optical comb [36], the atomic clock [37], time delayer [38], optical filter [39] and other applications based on high Q-factor microcavities. Among these applications, high-sensitivity sensors have always been one of the

most popular studies due to the sensitive evanescent field of WGM microcavities [41–43].For example, F. Vollmer published the single-molecule sensing with WGM microcavity in 2008 [40]. Although a variety of sensing applications have been published, the research on the relationship between mode characteristics and sensing of WGM cavity still has great potential.

To fabricate these WGM microcavities, there are many different methods. For example, V. Lefevre- Seguin demonstrated a very high Q-factor silica microspheres by heat-fusing a silica fiber [44]. K. J. Vahala group fabricated a microtoroid with photolithography method [45]. L. Jay Guo group demonstrated a microring with imprinting method [46]. Besides, there are many other methods, such as the D. Nakamura group using laser ablation to make microspheres [47]. Among all these methods, lithography is the most popular method since it has merits of high-precision, mass manufacturing and so on. However, such methods have demerits of high cost complex steps and unsuitable for on-demand fabrication. In addition, it is difficult to conduct all fabrication steps under normal temperature and pressure conditions because of the heating-reflow step. Under these considerations, our group (Y. Oki group) demonstrated an ink-jet printing method as a novel, simple fabrication process for a WGM polymeric microdisk in 2015 [48]. With the help of ink-jet technology, an on-demand fabrication method with low consumption under normal temperature and pressure conditions has been achieved. In this thesis, as the main object, the microdisks was fabricated by ink-jet method. On the other hand, as a test and reference object, the reconfigurable microring laser based on a lithography fabricated ring groove platform which is in collaboration with H. Chandrahalim [49,50]. The reason why we chosen this method as reference object because the reconfigurable ring groove can be easy for us to test by using same ink material as the ink-jet method, and the side walls of nearly ninety degrees can help us investigate WGMs in a high edge angle.

Although many methods and applications of WGM microcavities have been reported, most of these researches focus on improving Q-factor, threshold and sensitivity. Actually, the research on spatial position of WGM is also very interesting since studying the factors affecting WGM's spatial location will help us to control the mode position.The controlling of WGM spatial position will expand microcavity's potential. However, although some researches have studied the relation between cavity shape and WGM [51, 52], few researcher have studied the effects of other factors on the spatial position of WGM, especially on the wet-process fabricated cavity due to the difficulty of cavity shape control.

In this thesis, the author participated in the research reported for the first time in the world about the simple fabrication of self-forming WGM microdisks by using ink-jet technology as a unique fabrication method. In this method, droplets form thin film sharp angles on the edges of closed microdisks under the action of surface tension. In this sharp edge microdisk, WGM rotates closer to the inside of the cavity along the radius direction. The author named this kind of WGM as whispering-gallery "wedge" mode (WGWM). The thesis mainly discussed the effects of external factors on the spatial position of WGWM. The effects of cavity edge angle and the gain on spatial position of WGWM were mainly studied. In addition, wedge cavity based sensors and long-durability quantum dots doped microcavities based on WGWM research were also developed. It is believed that the results of this study will open the door of WGWM analysis in microcavities. It is also hoped that this work can help to realize the precise controlling of WGWM.

1.2. Chapter overview

This thesis consists of six chapters which are Chapter1 (Introduction), Chapter2 (Theory), Chapter3 (The effects of edge angles on whispering-gallery wedge

modes in printable microdisk lasers), Chapter4 (Sensing applications based on WGM microring lasers and WGWM microdisk lasers), Chapter5 (Effects of gain intensity on spectroscopic behavior of WGWM in quantum dots doped microcavities), and Chapter6 (Conclusion).

The 1st chapter is the introduction chapter. In this chapter, the background and motivation of this research are discussed. The importance of the research about effects of factors on whispering-gallery modes in wedge microcavity lasers is introduced.

The theory of WGM is discussed in the 2nd chapter. In this chapter, the basic principles of laser, optical waveguide and WGM microcavity are briefly introduced first. Then, the fabrication processes of ink-jet printed microdisks and the reconfigurable on-chip solid-state ring lasers are introduced. The sensing theory and numerical analysis of WGM are discussed at last.

In the 3rd chapter, the effects of edge angles on ink-jet printed WGWM microcavity are introduced. Initially, we found a phenomenon about some small peak shifts when we evaluated the laser properties of ink-jet printed microdisks. (This discovery was published at SPIE photonics west 2015) [53]. For this phenomenon, we practically experiment and numerically calculate the WGWM microdisks. As a result, we found that the spatial position difference between TE and TM will change with the change of angle. (The result was published at Optics Express) [54].

In the 4th chapter, a high sensitive temperature sensor with a reconfigurable WGM microring and a non-specific biosensing with a printable WGWM microdisk were demonstrated by lithography groove platform and ink-jet method, respectively. Based on the results in 3rd chapter, it was found WGWM microcavity can be applied to sensors since WGWM has a wider evanescent filed. In order to lay the foundation of WGWM sensor, temperature sensors were successfully devel-

oped by the R6G-doped SU-8 and R6G-doped TZ-001 normal WGM microring lasers (The result are published at Applied Physics Letters. Reproduced from [55], with the permission of AIP Publishing.). Based on the above result, a non-specific biosensor was demonstrated by an ink-jet printed Rhodamine 590 doped WGWM microdisk which successfully detected the BSA solution with a concentration of 100 ppm, and the thickness of adsorbed protein layer was calculated as 10 15 nm. This result provided the feasibility of a specific biosensor with the ink-jet printed WGWM microdisk. (The results are published at CLEO Europe 2017.) [56]

In the 5th chapter, spectroscopic behaviors in long-durability quantum dots (QDs) microcavities under different excitation power are introduced. We found a problem and another phenomenon in the results of the previous chapters. The problem is that the intensity of lasing weaken and the peaks shifted when the dye degraded. The phenomenon is that the peaks shifted with the changing of excitation power. (Part of the content appeared at SPIE proceeding.) [57] Both the problem and the phenomenon affect the performance of WGM applications. In order to solve the problem of photobleaching, we developed long-durability QDs doped microcavities. (Part of the content has been published at Optics Letters) [59] Based on the QDs doped microcavities, the effects of gain on WGWM spatial position in microcavities are analyzed out with numerical calculation.

In the 6th chapter, the demonstrated achievements so far are summarized, and the future work is prospected.

Chapter 2

Theory

2.1. Optical resonator

As mentioned in foregoing chapter, the optical resonator is the main part of a laser device since the performance of the optical resonator greatly affects the oscillation characteristics of the laser. A light will be amplified when the light go through a laser medium with a population inversion, so it is necessary to cause optical oscillation to achieve laser. In order to achieve optical oscillation, a parallel reflecting mirror may be installed to reciprocate the light many times in the medium to reach the standing wave condition. A light gains when two mirrors are placed on both sides of the laser medium and the optical axis of the mirror is adjusted so that the light can move repeatedly in the medium. When the gain is larger than the loss from diffraction, reflection, scattering and absorption in the mirror and medium, the laser oscillation can be achieved. In this way, what is composed of two or more reflecting mirrors and keeps the electromagnetic field of light internally by reflection on the reflecting surface is called an "optical resonator", and it also known as "optical cavity". As most common structure of optical cavity which is shown in figure 2.1, a light is amplified by reflecting back

and forth between two highly reflective mirrors, this cavity is known as Fabry-Perot resonator [8–10].

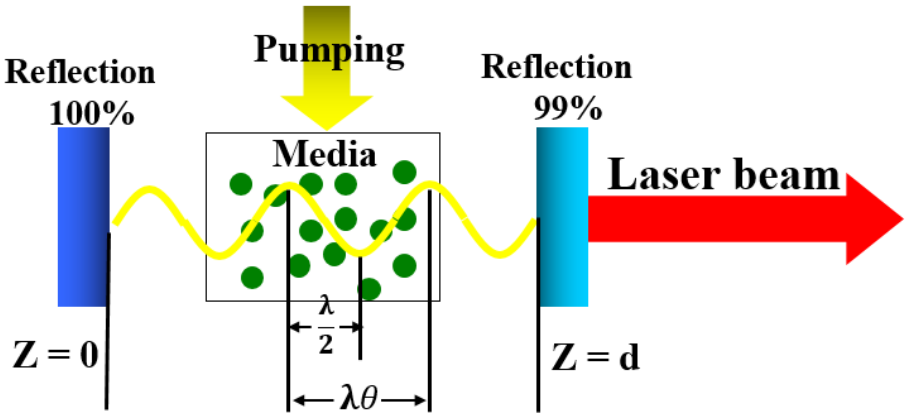

Figure 2.1: Fabry-Perot resonator

In an ideal resonator without any loss, the transverse component of the electric field can be represented by the wave function [60]

$$E(\mathbf{z},t) = \mathbf{Re}\{F(\mathbf{z})e^{i2\pi\nu t}\} \tag{2.1}$$

of a monochromatic light with frequency ν. The complex amplitude $U(\mathbf{r})$ satisfies the Helmholtz equation

$$\nabla^2 F(\mathbf{z}) + k^2 F(\mathbf{z}) = 0 \tag{2.2}$$

Here, the wave number k is

$$k = 2\pi\lambda = \frac{2\pi\nu}{c} \tag{2.3}$$

where c and λ denote the speed of light and the wavelength, respectively. The resonance mode is obtained by solving the Helmholtz equation under appropriate boundary conditions. The transverse component of electric field does not exist on the surface of the mirror in a lossless resonator, hence $F(\mathbf{z}) = 0$ when z=o , z=d which is as shown in figure 2.1. When the wave number k satisfies $kd = m\pi(m =$

$1, 2, \ldots$), the standing wave $F(\mathbf{z}) = A \sin kz (A : constant)$ at z=0, z=d satisfies Helmholtz equation. Here, wave number k can be shown as

$$k_m = \frac{m\pi}{d}, \qquad (m = 1, 2, \ldots) \tag{2.4}$$

Because the mode has a complex amplitude,

$$F(\mathbf{z}) = A_m \sin k_m z \tag{2.5}$$

can be obtained where A_m is a constant. m with a negative value does not constitute an independent mode since $\sin k_{-m} z = -\sin k_m$ In addition, $m = 0$ is related to the modes that do not generate energy because $k_0 = 0, \sin k_0 z = 0$. Therefore, the modes in a resonator can be shown as a standing wave of $A_m \sin k_m z$, and positive integers $m = 1, 2, \ldots$ is called mode number.

An arbitrary wave in the resonator is represented by

$$F(\mathbf{z}) = \sum_m A_m \sin k_m z \tag{2.6}$$

which is a superposition of resonance modes. Here, the resonance frequency for each mode is

$$\nu_m = \frac{mc}{2d}, \qquad (m = 1, 2, \ldots) \tag{2.7}$$

and as shown in figure 2.1, the resonance frequency interval between adjacent modes is represented by

$$\Delta\nu_f = \nu_{m+1} - \nu_m = \frac{c}{2d\cos\theta} \quad or \quad \Delta\lambda_f = \frac{\lambda^2}{2d\cos\theta} \tag{2.8}$$

which is called free spectral range (FSR).

This thesis mainly introduces the WGM resonator. Unlike the Fabry-Perot resonator, the WGM resonator does not achieve light amplification with the light back and forth reflection. In a WGM resonator, the light amplification is realized by a light advancing along the cavity boundary with total reflection when the

refractive index of the cavity is larger than that of the external environment. As shown in figure 2.2, the optical path length is Nd when a beam of light reflects N times circle the resonant. [16, 60].

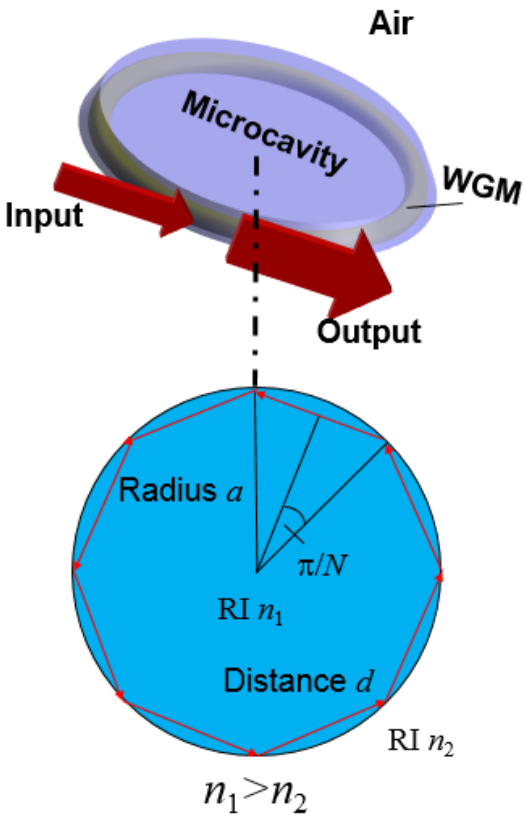

Figure 2.2: Whispering-gallery mode resonator

Here, the distance d is

$$d = 2a \sin(\frac{\pi}{M}) \tag{2.9}$$

The resonance frequency is determined when the optical path length is equal to an integral multiple of the wavelength, so the resonance frequency ν_m can be described as

$$\nu_m = \frac{mc}{Mdn_{eff}} \quad (m = 1, 2, \ldots) \tag{2.10}$$

hence the FSR is

$$\begin{aligned} \Delta\nu_f &= \frac{c}{Mdn_{eff}} \\ &= \frac{c}{2aM\sin(\frac{\pi}{M})n_{eff}} \end{aligned} \tag{2.11}$$

At this time, the number of light reflection in the resonant cavity tends to (infinity$N \to \infty$) , and the length of the optical path can approximate as $Md = 2\pi a$, hence

$$\Delta\nu_f = \frac{c}{2\pi an_{eff}} \quad or \quad \Delta\lambda_f = \frac{\lambda^2}{2\pi an_{eff}} \tag{2.12}$$

The light beam travels along the boundary of the resonator while repeating incidence and reflection at an angle close to the grazing angle which is shown in figure 2.2. Such optical mode is defined as Whispering Gallery Mode(WGM) [18].

2.1.1 Quality factor

Quality factor (Q-factor) is a most important indicator to evaluate the quality of an optical resonator [21–23]. It is a parameter for quantifying the energy storage capacity of a resonator. The Q-factor of the mode with natural frequency ω_0 is determined by the ratio of the energy stored inside the resonator to the energy lost in one cycle of the wave. When the Q-factor is expressed by the photon lifetime τ of the resonant [61, 62],

$$\mathrm{Q} = \omega_0 \frac{P}{-dP/dt} = \omega_0\tau \tag{2.13}$$

Where P and $(-dP/dt)$ denote stored energy and lost energy, respectively. According to equation 2.13, the Q-factor of the resonator can be obtained directly

by measuring the time decay of energy, and this method is called the "Cavity ring down method". [63] However, it is difficult to measure the time decay of energy, so measuring the resonance linewidth in the frequency domain can be also used to obtain the Q-factor. The amplitude of electromagnetic wave in the resonator can be expressed as

$$a(t) = A_0 e^{-t/2\tau} \cos \omega_0 t \tag{2.14}$$

By Fourier transforming the equation, the Lorenz intensity distribution of the resonance frequency can be described as

$$g(\omega) = \frac{1}{2\pi} \frac{\Delta\omega}{(\omega - \omega_0)^2 + (\Delta\omega/2)^2} \tag{2.15}$$

According to the Lorentzian waveform, the full width at half maximum(FWHM) can be given by

$$\Delta\omega = \frac{1}{2\pi\tau} \tag{2.16}$$

hence the Q-factor can be obtained by

$$\mathrm{Q} \approx \frac{\omega_0}{\Delta\omega} \approx \frac{\lambda_0}{\Delta\lambda} \tag{2.17}$$

The Q-factor also can be expressed by losses. By considering all possible losses, the equation of Q-factor can be given by [64, 65]

$$\mathrm{Q}_{Tol}{}^{-1} = \mathrm{Q}_{Abs}{}^{-1} + \mathrm{Q}_{Rad}{}^{-1} + \mathrm{Q}_{Sca}{}^{-1} + \mathrm{Q}_{Cou}{}^{-1} \tag{2.18}$$

where Q_{Tol} is the total Q-factor , Q_{Abs} is the Q-factor related to absorption loss, Q_{Rad} is the Q-factor related to radiation loss, Q_{Sca} is the Q-factor related to scattering loss , Q_{Cou} is the Q-factor related to coupling loss. Q_{Abs} is mainly limited by the material absorption loss, and also this is the maximum Q-factor that an ideal WGM resonator without any other losses. Different materials have different absorption, and the same material have different absorption in different

wavelength ranges. In a WGM resonator, both absorptions from gain material and matrix material can lead to losses. The absorption loss related Q-factor is defined by [66]

$$Q_{Abs} = \frac{2\pi n_{eff}}{\alpha\lambda} \tag{2.19}$$

where n_{eff} is the effective refractive index, λ is the wavelength of the propagating light in the cavity, α is absorption coefficient. The absorption coefficients of the polymeric materials used in this thesis are all about 10^{-2}, so the absorption limit Q of the resonator in the visible wavelength range of about 600 nm can be calculated as $10^6 \sim 10^7$.

In a WGM resonator, the propagation of light can be equivalent to the propagation of light in a curved waveguide. However, a curved waveguide can not block the light completely which is different with a straight waveguide, hence it lead to an energy consumption. This energy loss mechanism is known as bending loss [67]The radiation loss is related to bendiness of a waveguide, in the other words, the loss can be neglected when the cavity radius is much larger than the wavelength. When the radius approaches the wave growth time, the loss will increase. The radiation loss will increase when the radius of resonator decrease to near the order of light wavelength.

Since contamination or roughness can lead to imperfections of internal and surface, it result a discontinuity in refractive index. Thus, it will scatter the energy out of the waveguide, this energy loss is known as scattering loss. The scattering loss related Q can be expressed as [68],

$$Q_{Sca} = \frac{\lambda^2 D}{2\pi^2\sigma^2 B} \tag{2.20}$$

where D is the diameter of resonator, σ is the root mean square (rms) size which shows roughness, and B is the correlation length of surface inhomogeneities. Obviously, scattering losses can be minimized by using a homogeneous media or

improving surface smoothness.

The coupling loss comes from the energy dissipated when the resonator is coupled with other resonant or waveguides. In this work, we did not used any coupling methods to measure the resonator.

2.1.2 Finesse factor

Finesse factor (F-factor) is another parameter to evaluate the performance of a resonator. It is defined as the free spectral range (FSR) to the linewidth (FWHM : full width at half maximum)of resonances [69]:

$$\mathrm{F} = \frac{\omega_{FSR}}{\omega_{FWHM}} \tag{2.21}$$

Since the number of different frequencies can be distinguished by finesse, the finesse can evaluate the resolution of the resonator as an interferometer. Finesse also relate to Q-factor, it can be expressed as

$$\mathrm{F} = \mathrm{Q}\frac{\omega_{FSR}}{\omega_0} = \frac{\mathrm{Q}}{M} \tag{2.22}$$

Where Q is the Q-factor, ω_0 is resonant frequency, and M is the azimuthal number of WG mode. In this equation, the F can also tell us its physical meaning about the round trip number of photons in a resonator.

2.2. Fabrication methods of WGM microcavities

There are many different fabrication methods of WGM microcavities. For example, V. Lefevre- Seguin demonstrated a very high Q-factor silica microspheres by heat-fusing a silica fiber [44]. K. J. Vahala group fabricated a microtoroid with photolithography method [45]. L. Jay Guo group demonstrate a microring with imprinting method [46]. Among all these methods, lithography is the most

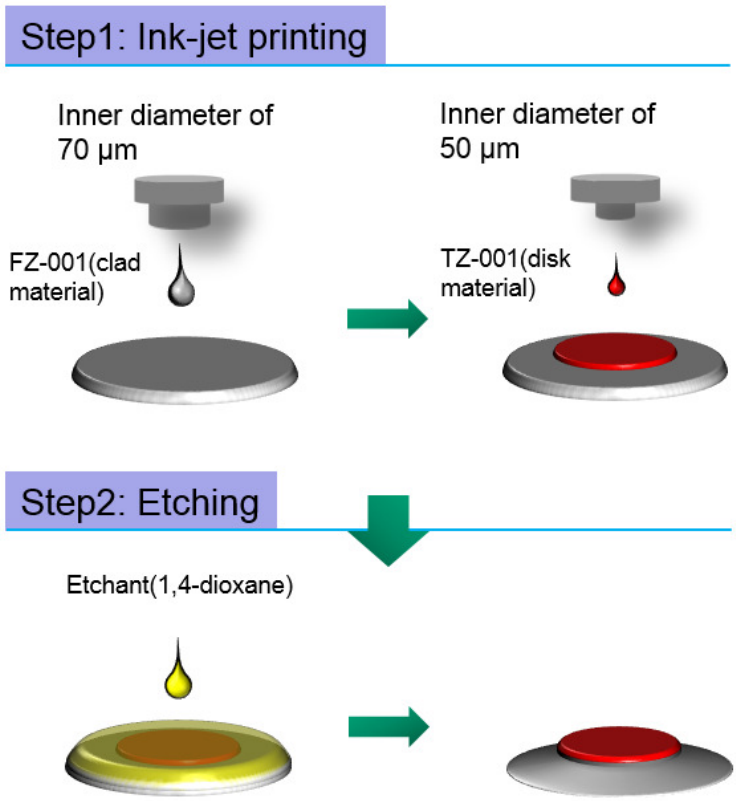

Figure 2.3: Ink-jet fabrication process of microdisk

popular method since it has merits of high-precision, mass manufacturing, on-chip integration and so on. In this paper, we mainly discuss about two kinds of fabrication techniques. One is ink-jet printing method which was published by our group (Y. Oki group) in 2015 [48]. The other is the reconfigurable microring laser based on a lithography fabricated ring groove platform which is collaborated with H. Chandrahalim [49]. The reason why we use these two methods is that both two methods have a potential for on-chip integration optical system. In particular, ink-jet printing technology, which is based on the printable photonics technology of our lab, has been studied for many years. Since ink-jet method is excellent at low materials wasting, fabricating in standard ambient temperature

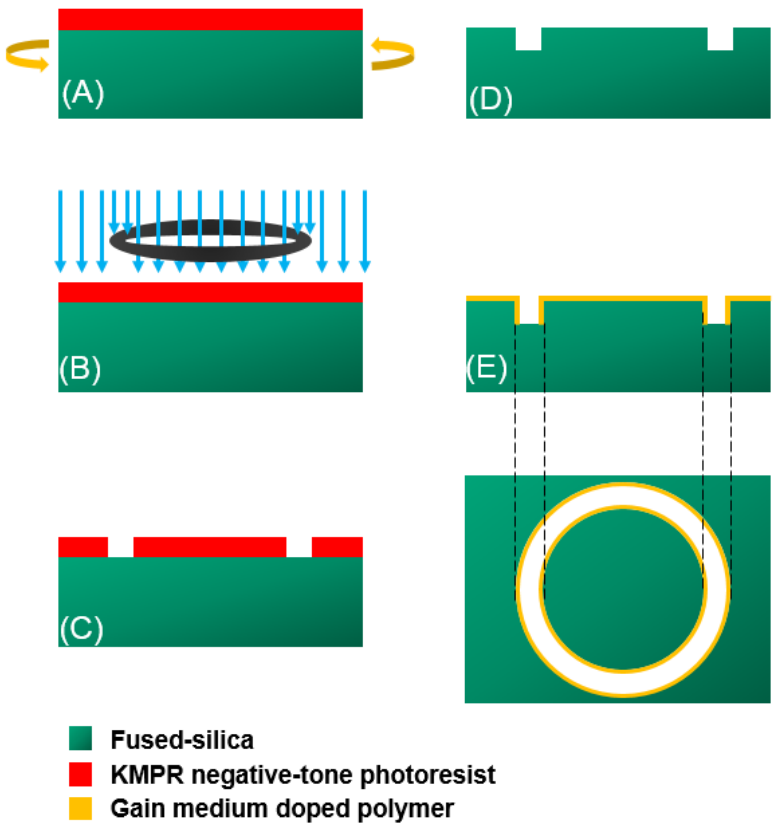

Figure 2.4: Fabrication process flow of microring

and pressure, low energy cost, and it is also can realize on-demand fabrication, it provide simple fabrication way for a WGM polymeric microdisk laser. As it was shown in figure 2.3, compared with lithography method, this method is very simple which can be concluded in two steps: (1) printing of the cladding layer and waveguiding disk layer by using ink-jet technique, and (2) etching the cladding layer. Owing to the two steps can be operated in a very short time, the rapid fabrication can be expected. With the forming by surface tension, both pedestal layer and disk layer can realized very smooth surfaces which provide a low optical loss condition.

In addition to ink-jet printed microdisk, a configurable on-chip solid-state microring also be used in this thesis. The fabrication process of the microring can be shown in figure 2.4. Firstly, negative photoresist was coated on the silica wafer and then exposed it under the UV light (A∼B). Then, the photoresist on the fused-silica wafer was developed (C). Next, the resist coated silica wafer was etched by using a reactive-ion etcher (D). Finally, a gain doped polymer layer was coated and dried on the microring platform (E). The microring was used as a device for comparison and testing. In addition, relevant sensing applications will also be mentioned. Although this method is relatively complex, once the host chip is fabricated, the device can be reused many times by replace the gain medium doped polymer. This is the attractive point for the configurable on-chip solid-state microring.

Here, we will discuss the effect of edge angles on WGM by combining two methods, in which ink-jet printed microdisks are the small angle cavity for subject object and the microrings are the large angle cavity for reference object.

2.3. Simulation and calculation of WGM

2.3.1 Plane model for simulation

The WGM resonator can be equivalent to a curved waveguide, hence we can simulate WGM with the numerical analysis of a curved waveguide. In order to analyze the field distribution of a curved waveguide, we also need to analyze and compare the straight waveguides since the calculation of a curved waveguide can be transformed into a straight waveguide. For a waveguide, effective refractive index is a key parameter, and the biggest difference between straight a waveguide and a curved waveguide is the difference of effective refractive index. Therefore,

the refractive index distribution of a curved waveguide can be converted to the refractive index distribution in an equivalent straight waveguide with equivalent refractive index. As shown in figure 2.5 (a), in a curved waveguide, when the width of the waveguide d is much smaller than the radius of curvature R, meanwhile the relative refractive index difference between core and clad

$$\Delta = n_{core}^2 - n_{clad}^2/2n_{core}^2 \tag{2.23}$$

is very small, the refractive index distribution can be converted to a straight waveguide as shown in figure 2.5(b).

$n'(x)$ can be expressed as follow

$$n'(x) = n(x)\left(1 + \frac{x}{R}\right) \tag{2.24}$$

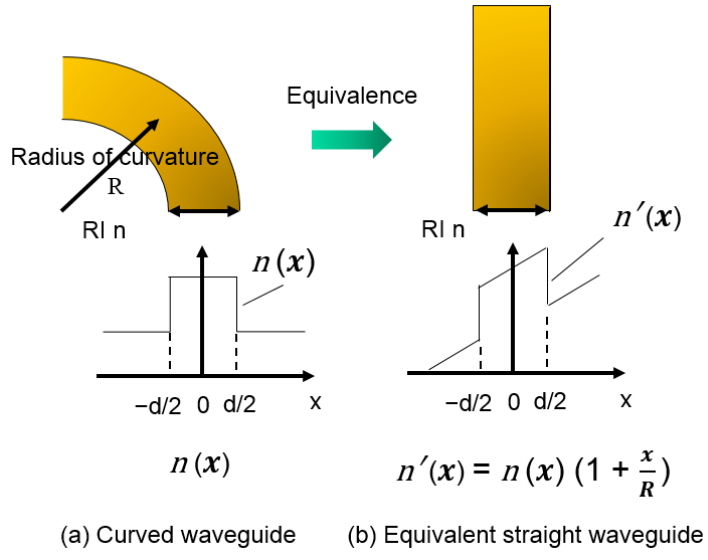

Figure 2.5: Equivalent refractive index

Based on the result of conversion from equivalent refractive index, the propagation of optical modes in curved waveguides can be calculated. As shown in

figure 2.6, in a cylindrical coordinate system, a TE mode propagates along the direction. The electric field is defined as $E = E_z \exp\{j(\omega t - \beta\theta)\}$, when $\frac{\partial}{\partial z} = 0$,

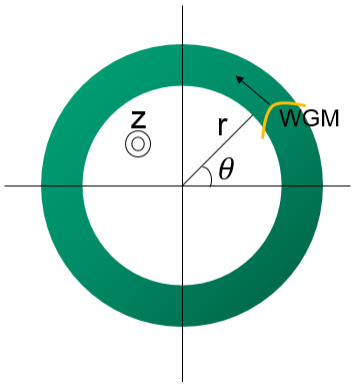

Figure 2.6: Cylindrical coordinates

the wave equation can be expressed as

$$\nabla^2 E = \varepsilon\mu\frac{\partial^2 E}{\partial t^2}$$

$$\left(\frac{\partial^2}{\partial r^2} + \frac{1}{r}\frac{\partial}{\partial r} + \frac{1}{r^2}\frac{\partial^2}{\partial\theta^2}\right) E = \varepsilon\mu\frac{\partial^2 E}{\partial t^2}$$

$$\frac{\partial^2 E}{\partial r^2} + \frac{1}{r}\frac{\partial E}{\partial r} + \left(k_0^2 n^2 - \frac{\beta^2}{r^2}\right) E = 0 \tag{2.25}$$

Here, $k_0^2 = \omega^2\mu_0\varepsilon = (2\pi/\lambda)^2$, and n is the refractive index. If $x = k_0 nr$,

$$x^2\frac{\partial^2 E}{\partial x^2} + x\frac{\partial E}{\partial r} + (x^2 - \beta^2)E = 0 \tag{2.26}$$

which is called Bethel equation. Thus, the electric field distribution is expressed by the following equation,

$$E = AJ_\beta(k_0 nr) + BY_\beta(k_0 nr). \tag{2.27}$$

Here we assume to solve a planar WGM cavity model. With $r = 0$ in the core, $Y_\beta(k_0 nr)$ becomes inappropriate because Bessel functions of the second kind diverges. Outside of the core, $J_\beta(k_0 nr)$ is ignored because it is impossible to solve the dispersion formula if $J_\beta(k_0 nr) + Y_\beta(k_0 nr)$. It should be noted here that this calculation method is not accurate for evanescent outside the core because we assume that the whole inside and outside environment is continuous. In fact, refractive index inside and outside core is not continuous. In addition, the phase after light travels one circle must be consistent with the original, hence β is a discrete integer value. Therefore the solution can be assumed as

$$E = AJ_\beta(k_0 n_{core} r) \qquad (r \leq a) \tag{2.28}$$

$$E = BY_\beta(k_0 n_{clad} r) \qquad (r > a) \tag{2.29}$$

Set the differential form of a function $f(x)$ to $f'(x)$. Since the electromagnetic field components parallel to the boundary surface are continuous,

$$AJ_\beta(u) = BY_\beta(v)$$

$$AJ'_\beta(u) = BY'_\beta(v)$$

$$u = k_0 n_{core} a$$

$$v = k_0 n_{clad} a$$

Due to the characteristics of Bethel function, it can be derived as

$$J'_\beta(u) = \frac{\beta}{u} J_\beta(u) - J_{\beta+1}(u)$$

$$Y'_\beta(v) = \frac{\beta}{v} Y_\beta(v) - Y_{\beta+1}(v)$$

Hence, the dispersion formula is as follows.

$$\frac{\beta}{u} - \frac{J_{\beta+1}(u)}{J_\beta(u)} = \frac{\beta}{v} - \frac{Y_{\beta+1}(v)}{Y_\beta(v)} \tag{2.30}$$

The calculation result of this dispersion formula under the condition of $a = 50\mu$m, $n_{core} = 1.78$, $n_{clad} = 1.45$, $\beta = 913$ is shown in figure 2.7.

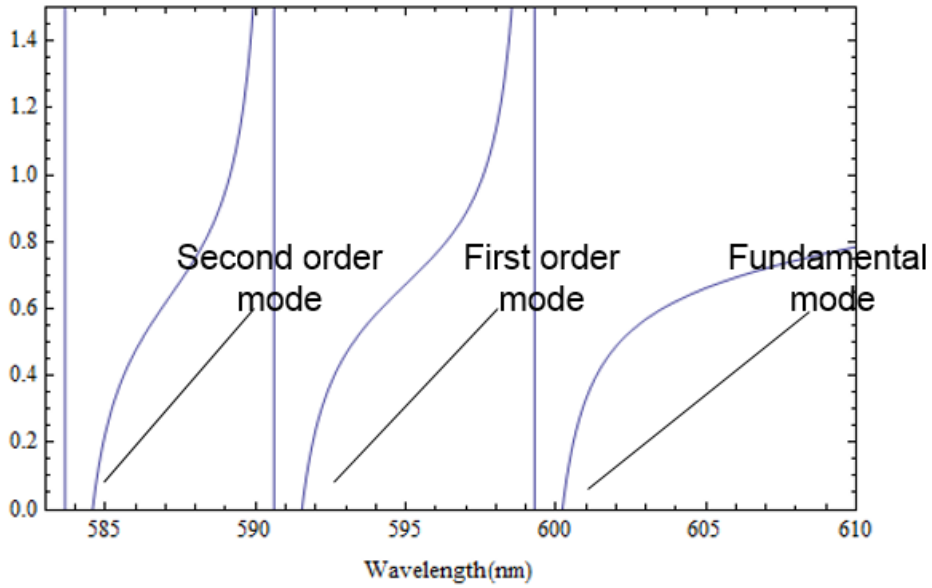

Figure 2.7: WG mode field

As described above, the wavelengths of the fundamental mode, first order mode, and second order mode are obtained. The electric field distribution in each mode is shown in figure (2.8, 2.9, 2.10).

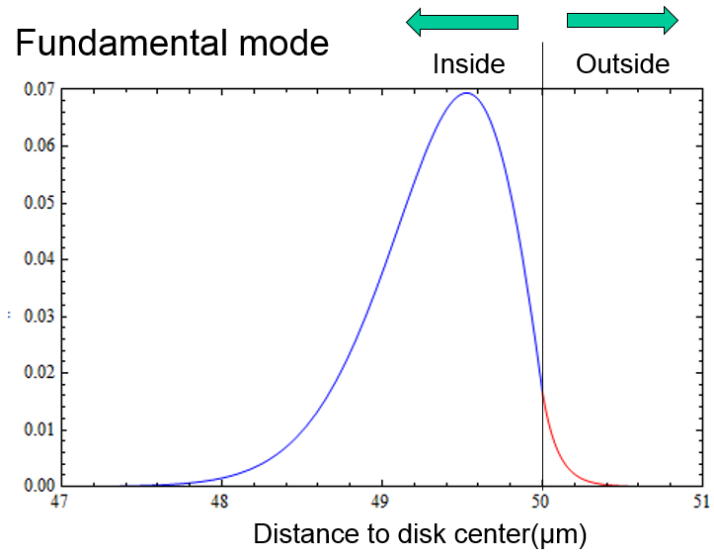

Figure 2.8: Fundamental mode

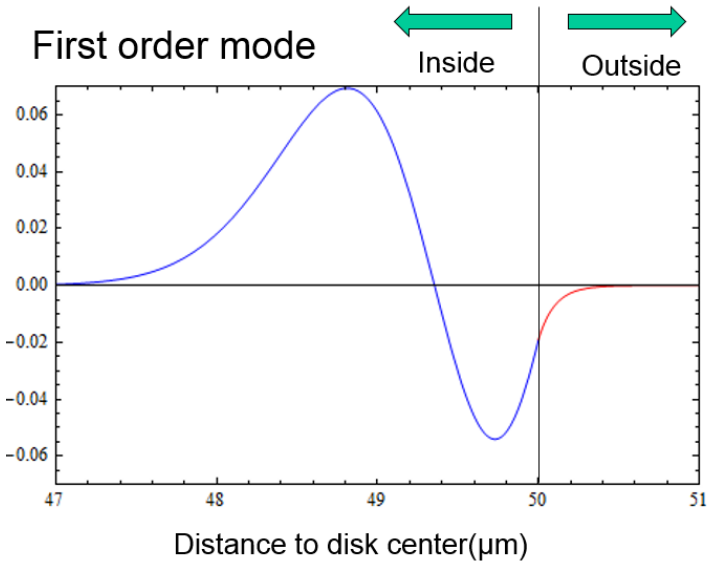

Figure 2.9: First order mode

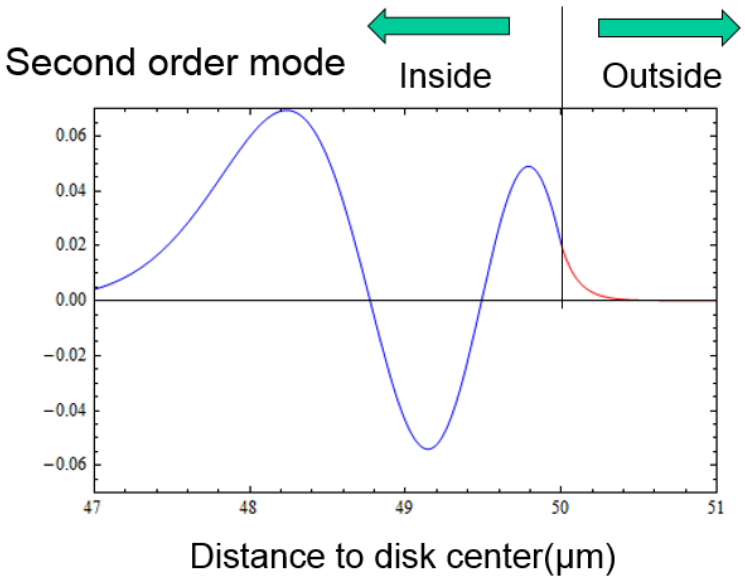

Figure 2.10: Second order mode

2.3.2 Cross-section model for simulation

The previous section introduced a rough WGM calculation by equivalent refractive index of curved waveguides method. This calculation can only roughly calculate the two-dimensional WGM plane resonator. Since this thesis mainly discusses the effect of wedge angle on WGM, a 3D simulation is needed for obtain a cross-section view. There are several ways to simulate three-dimensional WGM resonators, such as finite-difference time-domain (FDTD) [70]. and finite-element method (FEM). Most of these methods use approximate computation to solve the complex Maxwell's equations in WGM resonators. Regardless of which method to choose, the computation of three dimension is very huge. In order to simplify calculation and remove the resonator size limitation, Mark Oxborrow developed the model of axisymmetric WGM cavities based on FEM in COMSOL. In Oxborrow's model, the complicated computation of 3D WGM resonators is transformed into a simple 2D cross-section computation. Thereafter, M. Imran Cheema modified Oxborrow's model with implementing the perfectly matched layer (PML) along boundaries of domain . In this way, the model is more precise and excellent. In this thesis, the Oxborrow's model with PML modified by Cheema was used to calculate the eigenfrequencies of modes using the FEM in COMSOL software [71–74]. In Oxborrow's model, FEM equations based on Maxwells equations in the weak form can be expressed as [71]:

$$\int_V [(\bigtriangledown \times \widetilde{\mathbf{H}}^*)\epsilon^{-1}(\bigtriangledown \times \mathbf{H}) - \alpha((\bigtriangledown \cdot \widetilde{\mathbf{H}}^*)(\bigtriangledown \cdot \mathbf{H}) + c^{-2}\widetilde{\mathbf{H}}^* \cdot \frac{\partial^2 \mathbf{H}}{\partial t^2}]dV \tag{2.31}$$

where $\mathbf{H}$ denotes the magnetic field, $\widetilde{\mathbf{H}}$ denotes the test magnetic field, $\int_V$ denotes the volume integral over the resonator's interior space, ϵ^{-1} denotes the inverse relative permittivity tensor and * denotes magnetic field strength. In axisymmetric resonators, the time independent part of the magnetic field strength can be ex-

pressed with cylindrical coordinates system as:

$$\mathbf{H}(\mathbf{r}) = e^{iM\phi}\left\{H^x(x,y), H^\phi(x,y), H^y(x,y)\right\} \tag{2.32}$$

where M and ϕ denote WGM's azimuthal mode order and azimuthal coordinate, respectively. Applying Laplacian weak term to the equation, it can be given by:

$$\widetilde{\mathbf{H}}^* \cdot \frac{\partial^2 \mathbf{H}}{\partial t^2} = c^{-2}x(\widetilde{H}^x H^x_{tt} + \widetilde{H}^\phi H^\phi_{tt} + \widetilde{H}^y H^y_{tt}) = -\bar{c}^2 f^2 x(\widetilde{H}^x H^x + \widetilde{H}^\phi H^\phi + \widetilde{H}^y H^y) \tag{2.33}$$

Here, there is no any components depend on the azimuthal coordinate ϕ in axisymmetric cavities, so that it is resulted in transferring a 3D simulation to a 2D simulation. Based on this equation, Cheema applied PMLs as an anisotropic absorber to modify the diagonal permittivity and permeability tensors which is shown in [73]:

$$\bar{\epsilon} = \epsilon\bar{\Lambda}, \bar{\mu} = \mu\bar{\Lambda}, \tag{2.34}$$

$$\bar{\Lambda} = \left(\frac{\tilde{r}}{r}\right)\left(\frac{s_z}{s_r}\right)\hat{r} + \left(\frac{r}{\tilde{r}}\right)(S_z S_r)\,\hat{\phi} + \left(\frac{\tilde{r}}{r}\right)\left(\frac{s_r}{s_z}\right)\hat{z} \tag{2.35}$$

$$s_r = \begin{cases} n_{medium} & 0 \le r \le r_{pml} \\ n_{medium} - jG\left(\frac{r-r_{pml}}{t_{rpml}}\right)^N & r > r_{pml} \end{cases}$$

$$s_z = \begin{cases} n_{medium} - jG\left(\frac{z_{lpml}-z}{t_{lpml}}\right)^N & z < z_{lpml} \\ n_{medium} & z_{lpml} \le z \le z_{upml} \\ n_{medium} - jG\left(\frac{z-z_{upml}}{t_{upml}}\right)^N & z > z_{upml} \end{cases}$$

$$\tilde{r} = \begin{cases} r & 0 \le r \le r_{pml} \\ r - jG\left(\frac{(r-r_{pml})^{N+1}}{(N+1)t^N_{rpml}}\right) & r > r_{pml} \end{cases}$$

where n_{medium} denotes refractive index of the medium, N denotes order of the PML, and G denotes a positive integer. t_{rpml}, t_{upml}, t_{lpml} denote the PML thicknesses in the radial, +z and -z directions, respectively. r_{pml}, z_{upml}, z_{lpml} denote

the start locations of PML in the radial, +z and -z directions, respectively. With the applying of PMLs the master equation of Oxborrow's model can be modified as

$$\int_V [(\bigtriangledown \times \widetilde{\mathbf{H}}^*)\bar{\epsilon}^{-1}(\bigtriangledown \times \mathbf{H}) - \alpha(\bigtriangledown \cdot \widetilde{\mathbf{H}}^*)(\bigtriangledown \cdot \mathbf{H}) + c^{-2}\widetilde{\mathbf{H}}^* \cdot \bar{\mu} \cdot \frac{\partial^2 \mathbf{H}}{\partial t^2}]dV \qquad (2.36)$$

In this way, with the contributions of Oxborrow and Cheema, such an excellent model can be realized. The detailed deduction process of these equations can be found in papers of Oxborrow and Cheema [71,73]. By casting these equations into the FEM software COMSOL, a calculation model of cross-section WGM resonator can be obtained. As shown in figure 2.11, a microdisk model with a diameter of 120 μm and a thickness of 1 μm is built for simulation. The simulation result of fundamental mode, first order mode, and second order mode are shown in figure 2.12, figure 2.13, figure 2.14, respectively. A cross-section of half cavity can be observed in the figures. The rainbow part in the figures are the electric field distributions of WGM, and the color represents the intensity of the electric field (red is the strongest, blue is the weakest, as shown by the color contrast on the right side of each figure). In addition, the white arrow represents the direction of electric field vibration, which can help us to observe TE and TM modes. Since the results show very accurate cross-sectional maps of the electric field distribution of WGM, it can be very helpful for us to discuss the change of mode position due to external factors.

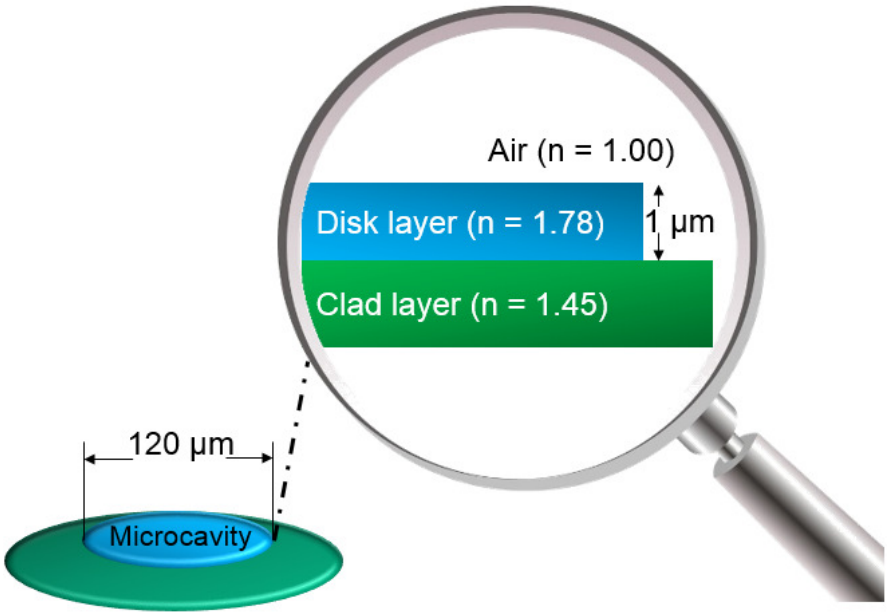

Figure 2.11: Schematic of microdisk model

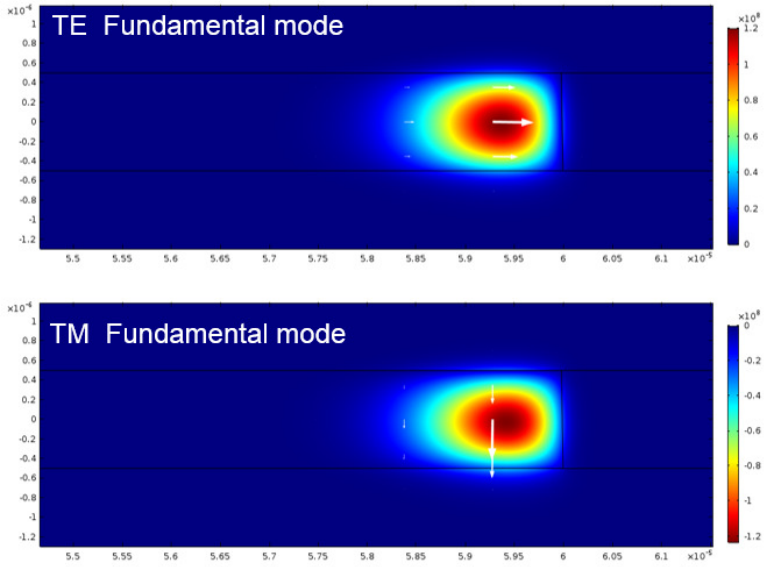

Figure 2.12: Fundamental mode of TE and TM

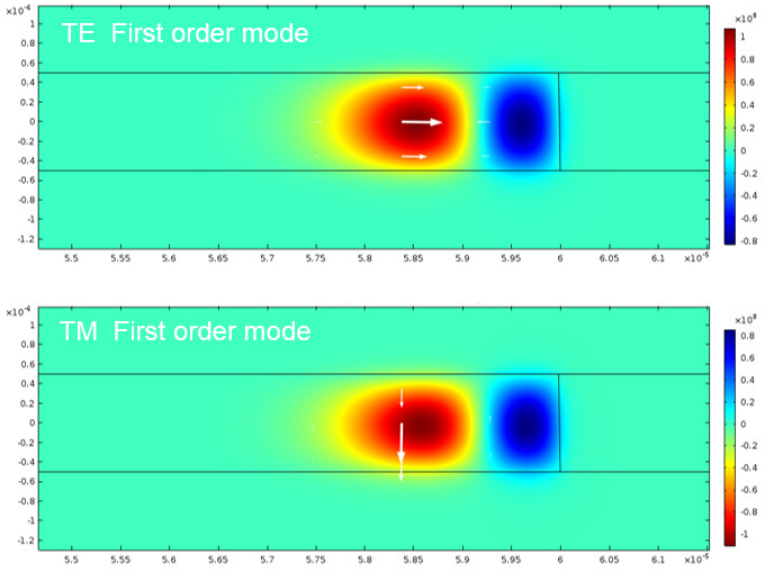

Figure 2.13: First order mode of TE and TM

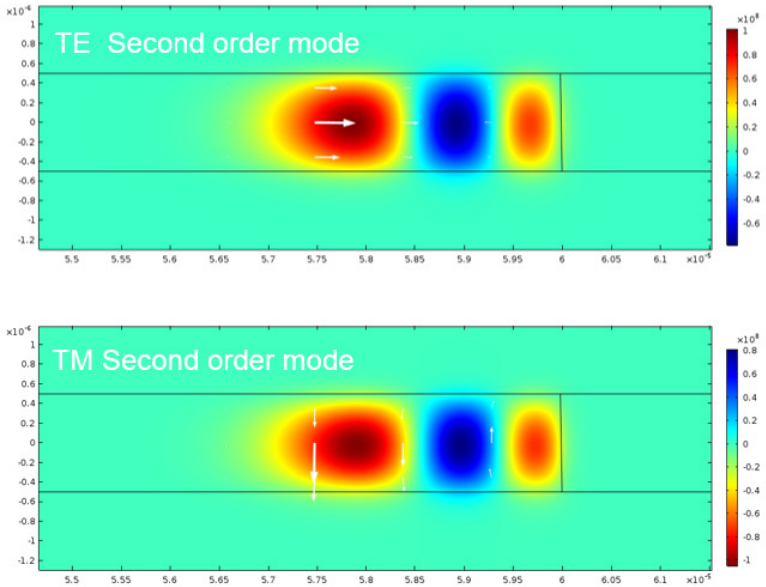

Figure 2.14: Second order mode of TE and TM

Chapter 3

The effects of edge angles on whispering-gallery wedge modes in printable microdisk lasers

3.1. Introduction and purpose

As mentioned in chapter 1, WGM microcavities can be used for many applications because of its many advantages, especially for sensing devices with high sensitivity. Many researchers started to work on WGM microcavities sensing since high sensitivity sensing (such as single molecular sensing) by using WGM microcavities was realized [40–43]. Currently, although many works of high sensitivity sensors have been reported, researchers are still trying hard to improve the microcavities. This is because there is still potential to further improve performance to make higher sensitivity sensors and to develop other applications.

A highly sensitive WGM sensing is mainly achieved by tracking of the resonance spectrum shift. Therefore, the linewidth of resonance spectrum will directly

affect the sensitivity of WGM sensor when the resolution of spectrometer or other detector is sufficient. As described in equation 2.17, the FWHM of resonance frequency will decrease with the increasing of Q-factor, and this is the reason why high-Q cavity is always a topic for sensing. According to the property of microcavity, it can be divided into two kinds, one is active cavity, the other is passive cavity [75, 76]. The active cavity mainly realizes the resonance spectrum by the lasing of the gain medium, hence using a strongly gain medium to compensate round-trip propagation loss is a method to improve the Q-factor. To improve the Q-factor of a passive cavity, a process such as a thermal reflowing [45] or a chemical etching [52] for smoothing the microcavitys surface is a common method. In addition, on the basis of optimizing the design of the microdisk cavity, in order to balance the limitation of the optical field and the interaction with the interface material, a lot of research has been done to improve the Q-factor [77].

Since the main fabrication methods of this thesis are wet process, we mainly focus on the research of active microcavity. The research of active WGM microcavities are very interesting due to the excellent optical characteristics [78,79], and high sensitivities for sensing [76,80]. Generally, the high-Q wedge WGM resonator with gain medium emits multimode, and it includes TE modes and TM modes in a wedge microdisk laser. The emitting of multimode results in mode overlaps. With the shape changing of wedge microdisk by fabrication process, this mode overlaps may broaden or narrow the linewidth of lasing spectral, which directly affects the accurate estimations of FSR and sensitivity. Although it is very interesting, there are few systematic researches on TE and TM mode distributions in a wedge microcavity because of the above challenges. To open the entrance of the research about multimode emission, it is worth to start studying the mode distribution with different shape of wedge microcavities. This is because the stability and identifiability of multimode emission spectra are related not only to the gain

material, but also to the shape of wedge-shaped microcavities.

Currently, due to the merits of the high precision and good reproducibility, photolithograph method is the most common fabrication method of microcavities. The disk formation is facility to be realized with a mask and light exposure by photolithograph method [45].Although there are many advantages by using lithography method, the method is limited in active cavity fabrication due to high-energy or high temperature will inactivate the gain material. In order to fabricate high performance active WGM microdisk under normal temperature and pressure, a low threshold dye-doped polymeric microdisk laser was developed with ink-jet technology [48]. In addition, ink-jet method can achieve cavity fabrication on arbitrary substrate, which makes the fabrication method flexible. A small wedge angle will be naturally formed near the edge of the ink-jet printed microdisk under the action of surface tension. The evanescent field on the edge of wedge-shaped microdisk provides an attractive platform for high precise sensing technology and basic quantum optical research, for example, Heisenberg-limited displacement sensor [81], ultrasensitive force sensor [82].In a wedge-shaped microdisk, WGM rotates closer to the inside of the cavity along the radius direction. The author named this kind of WGM as whispering-gallery "wedge" mode (WGWM).

Generally, since the distribution of evanescent field is related to the edge angle of a wedge microdisk, the optical coupling strength is sensitive to the relative position between the measuring object and the wedge microdisk. Considering the requirements of high precise sensing applications, it is significant to investigate the relations between mode distribution and edge angle. Furthermore, the investigation will also help to achieve the control of WGWM.

In this chapter, two parts of contents were discussed, the first part is about ink-jet printed low threshold microdisk lasers, and the second part is about the

effect of edge angle on WGWM spatial position. In the first part, we used ink-jet method to fabricated LDS 798 doped microdisk and Rhodamine 590 doped microdisk, and relatively low lasing thresholds were obtained. Then WGM mode split were also confirmed. In the second part, to clarify the mode split, the lasing spectrum of the polymeric wedge microdisk lasers with the edge angles of relatively smaller degree and relatively larger degree were measured. By analyzing the lasing spectrum of the two kinds of microdisks, the changes of FSR and resonance wavelength difference between the TE and adjacent TM modes were analyzed with the numerical simulation. By investigating effects of the edge angles on several parameters of modes, we theoretically clarified the relations between the fundamental TE and left adjacent TM modes in the lasing spectra. (Two partial contents of this chapter has been published at SPIE and Optics Express, respectively) [53, 54].

3.2. Ink-jet printed microdisk lasers

3.2.1 Experiments

To achieve optical waveguide, the thickness of micron order is needed. However, thicker film requires a high concentration which lead to a high viscosity, and high viscosity will block the micro nozzle. Here, we used hyperbranched polymer because it has a lower viscosity than linear polymers [83]. For fabricating microdisks, a fluorine-based hyperbranched polymer FZ-001 with RI were used for forming clad layer. A triazine-based hyperbranched polymer TZ-001 with RI of 1.78 were used for forming disk layer.

Figure 3.1 shows the fabrication steps of a wedge microdisk with ink-jet method. First step, ink-jet printing technology was used for fabricating the clad layer and

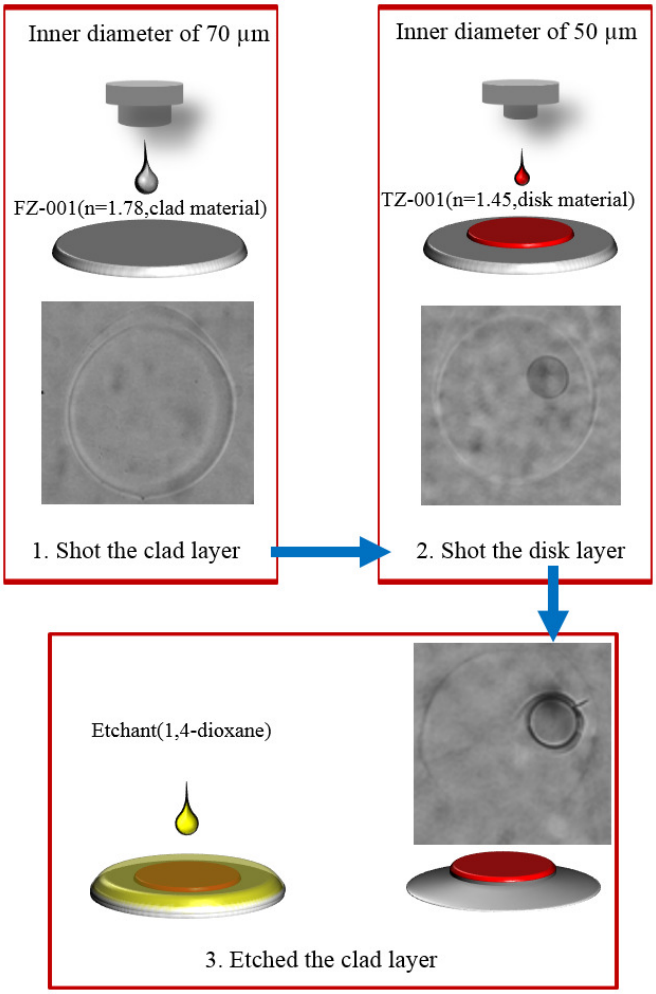

Figure 3.1: The fabrication steps of a wedge microdisk laser by using ink-jet printing(insets represent the microscopic images of each step).

core disk layer. This is the main step of ink-jet printing method. In order to guarantee the stable droplets for forming homogeneous microdisk several printing parameters need to be adjusted. For example, the distance form substrate to nozzle were adjusted to control the landing status of droplets. The moving speed of micro nozzle were adjusted to prevent turbulence. The pulse voltage and pulse width were used to adjust the injection velocity and droplet size. The fabrication

parameters of LDS798 doped microdisk and Rhodamine 590 doped microdisk are shown in table 3.1.

Table 3.1: The fabrication parameters of LDS798 doped microdisk and Rhodamine 590 doped microdisk.

	Clad layer	LDS798 disk	Rhodamine 590 disk
Distance	∼1 mm	∼1 mm	∼1 mm
Moving speed	2 mm/s	2 mm/s	2 mm/s
Concentration	10 wt.% FZ-001	10 wt.% TZ-001	10 wt.% TZ-001
Gain meterial	0mM	5mM LDS 798	5mM Rhodamine 590
Solvent	1,4-dioxane	Cyclohexanone	Cyclohexanone
Pulse voltage	104 V	146 V	160 V
Pulse width	26 μs	44 μs	20 μs
Shots number	5	1	1
Nozzle diameter	70 μm	50 μm	50 μm

Based on above parameters, a clad layer with a diameter of 250∼300 μm can be formed with five shots printing by using a 70 μm diameter microdrop nozzle (MD-K-130, Microdrop Technologies GmbH.) on a polyethylene terephthalate (PET) substrate. After clad layer dried ,core disk layer will be printed on it. Herein, all microdisks in this thesis are between 70 and 120 μm in diameter. Size control can be mainly realized by adjusting of environmental conditions, nozzle parameters, and ink concentration. As shown in the figure, in each batch of fabrication, because the fabrication conditions are exactly the same, the errors of all disk diameters are within 1 μm. However, since different batches of disks are made at different times, it is very difficult to ensure that the fabrication conditions are identical (such as temperature and humidity), so different batches of disks will have different sizes with a maximum variation of 30%.

After first step of printing, the Second step, which is the etching step was operated by dropping a small amount of 0.2 μL 1,4-dioxane with micropipet on microdisk. After etching for about 1 s, the residual liquid was removed.

The SEM and microscope images of microdisks are shown in figure 3.2. Herein, figure 3.2 (a) shows arrayed microdisks which demonstrated that ink-jet method can realize mass fabrication. The single LDS798 doped microdisk and Rhodamine 590 doped microdisk are shown in figure 3.2 (b), (c), and both disks shows fine and smooth edge. By optimizing the printing parameters, similar diameters microdisks with different ink can be obtain although the dye-doped TZ-001 has different wettability to the FZ-001. Meanwhile, it can be found that the Rhodamine 590 doped microdisk was thinner than LDS798 doped microdisk by comparing (b) and (c). It is worthy to note that, in our ink-jet fabrication method, the process time can be complimented within 20 seconds, and the fabrication area can be concentrated within 1 mm^2.

Based on the lasing spectra and lasing threshold, the LDS798 doped and Rhodamine 590 doped TZ-001 microdisks WGM laser were evaluated. As mentioned in section 3.1, a spectrum of passive microdisk which fabricated by typical photolithography method is generally measured by optical coupling with fiber taper. In this research, since our microdisks are active laser, the lasing signal was collected the leaked lasing light from a microdisk edge with a optical microscope based setup which is shown in figure 3.3. As a pumping light, a Q-switched Nd:YAG laser was used with wavelength, pulse duration and repeat rate of 532 nm, $\sim$ 0.5 ns and 100 Hz, respectively. A tunable reflective neutral density (ND) filter was used for adjusting the pumping power. The pumping power was measured by using a powermeter set at position 2 which is shown in figure 3.3. Here, the loss of optical system was taken into account when we calculated the excitation intensity. A plano-concave lens with the focal length of 20 mm for focusing

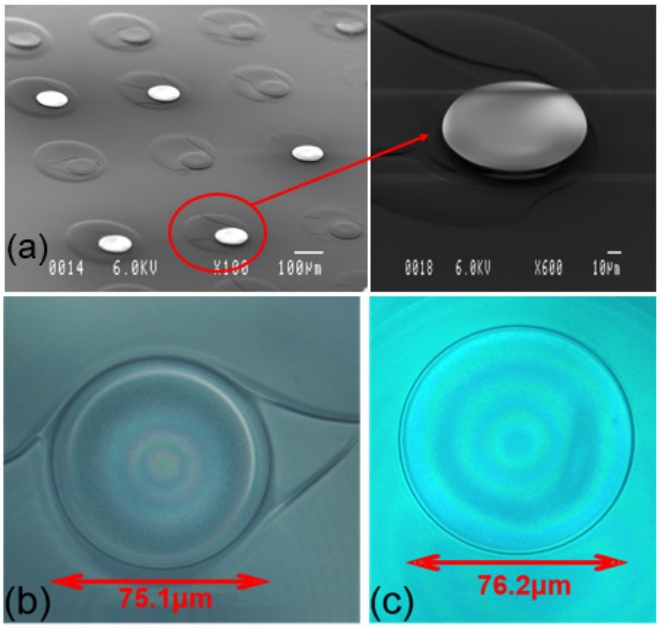

Figure 3.2: (a) The SEM images of microdisk; (b) The microscopic image of LDS798 doped TZ-001 microdisk; (c) The microscopic image of a Rhodamine 590 doped TZ-001 microdisk.

the beam spot within diameter of 350 μm, the spot size can be adjusted by changing the distance of lens. Finally, the lasing signal was leaked from edge of a microdisk, and collected by spectrometer via a microscope system. Here, for measuring LDS798 doped TZ-001 microdisk, a spectrometer HR4000 with resolution of $>$ 1 nm from cean Optics was used. On the other hand, for measuring Rhodamine 590 doped TZ-001 microdisk, a spectrometer MS7504 with resolution of $>$ 0.04 nm from Solar TII was used.

3.2.2 Results and discussion

The lasing spectra of LDS798 doped TZ-001 microdisk can be shown in figure 3.4 (a). Some lasing peaks gradually appeared with the increasing of excitation intensity. The peaks of lasing spectrum show the multimodes of WGM in microdisk.

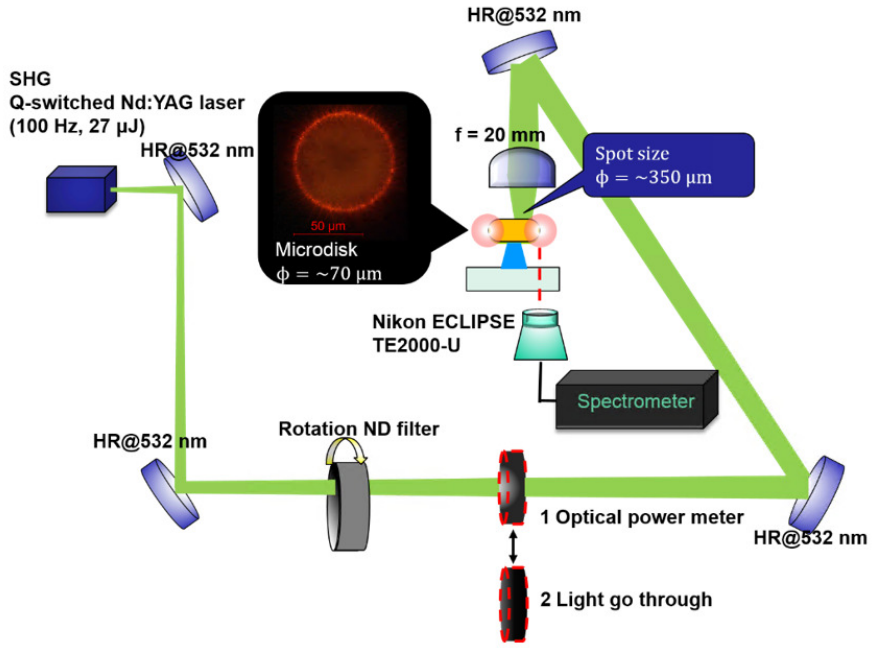

Figure 3.3: Optical microscope based measurement setup for lasing signal of active microdisks.

For analyzing the input-output characteristics, the easily identifiable 5 modes of A1∼A5 were selected (figure 3.4 (b)). Based on the input-output characteristic, the relatively low threshold was regarded as 2.8∼3.7 μJ/mm^2 which was shown in figure 3.4 (b).

As shown in figure 3.4 (a), the experimental result of wavelength split about 1.66 nm can be obtained. As mentioned in chapter 2, WGM split can be expressed as

$$\triangle\lambda = \frac{\lambda^2}{2\pi n_{eff} r_{eff}} \tag{3.1}$$

where λ denotes resonance wavelength, n_{eff} denotes RI of WGM, r_{eff} denotes the effective radius of WGM. Herein, the optical gain regions of LDS798 and Rhodamine 590 are around 800 nm and 600 nm, respectively. Because n_{eff} can

be calculated by RI of TZ-001 (n=1.78), a r_{eff} of 34.5 μm can be estimated. A effective radius r_{eff} of 34.5 μm can be obtained which is very close to the actual size of microdisk in radius of 37.5 μm(3.2(b)). Therefore, the WGM field is very close to the edge inside of disk.

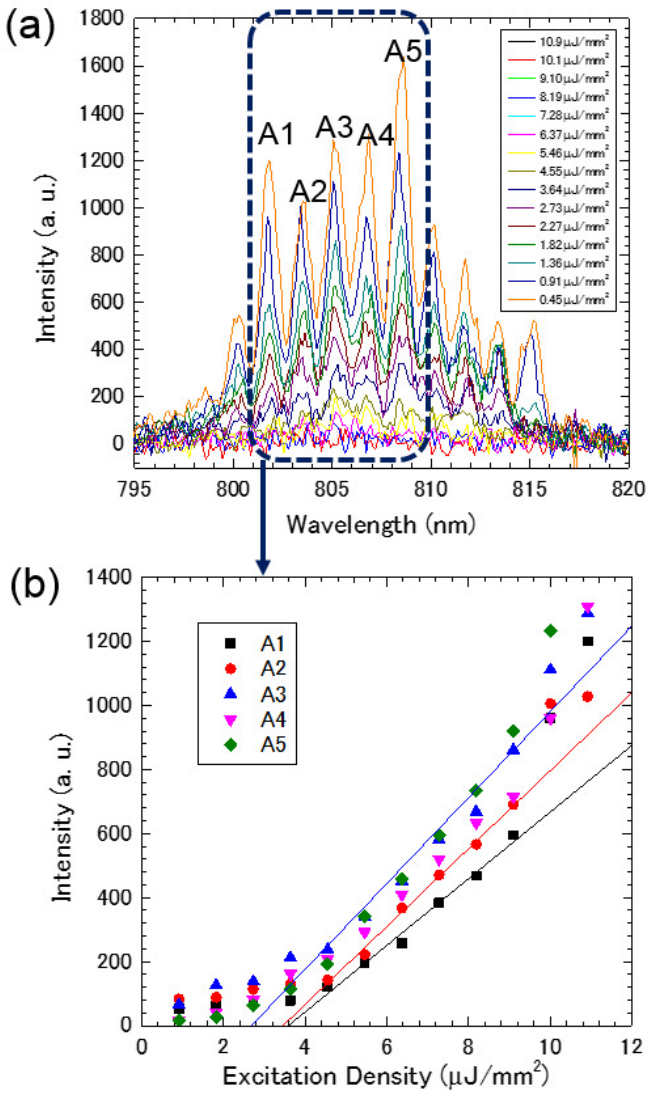

Figure 3.4: (a)The lasing spectrum and (b) input-output characteristic of LDS798-doped microdisk.

Generally, the Rhodamine590 doped microdisks are more difficult for etching process since it was thinner than a LDS798 doped microdisk. Furthermore, since a higher stimulated emission cross-section in Rhodamine 590 the WGM lasing in visible region should has a relatively lower threshold. Figure 3.5 (a)(b) shows spectrum of a non-etched microdisk under different pumping intensity. As shown in figure 3.5 (c), the intensity of each lasing peak selected from 3.5 (a)(b) was listed up as a function of pumping intensity. Figure 3.6 shows similar plots from a etched microdisk which is another sample. The experimental WGM split of the etched disk was 0.89 nm which was shown in figure 3.6 (a). From this data, a effective radius r of 36.2 μm was calculated. It was close to the actual radius of the microdisk. A important and interesting phenomena was observed that the peak wavelength always has blue shift with increasing of the pumping intensity. This phenomena led to a inhomogeneous output intensity of each WG modes which resulted a bending curves of input-output characteristic in figure 3.6 (c). Since the bending curves are difficult to accurate characterize lasing threshold, a rough lasing threshold of 2.0$\sim$2.5 μJ/mm^2 is estimated. By comprising figure 3.5 (a) with 3.6 (a), the etched disk has a higher output since etching increased the leaking light from microdisk bottom. Furthermore, the lasing thresholds from figure 3.6 (c) were larger then figure 3.5 (c), this is because of the increasing of scattering loss on the bottom surface. The spectral shifts of 0.89 and 0.83 nm can be obtained in figure 3.5 (a) and 3.6 (b).

The peak shifts as a function of the excitation intensity on the non-etched Rhodamine 590 doped microdisk is shown in figure 3.7 (a). The shifts were linear and had similar slope of 0.045 nm per μJ/mm^2, and approximately similar result were obtained for etched microdisk. Besides, LDS798 doped microdisk did not show any wavelength shifts which was shown in figure 3.7 (b). The shift of Rhodamine doped microdisk was 0.15% which was 2$\sim$3 times larger than that can be

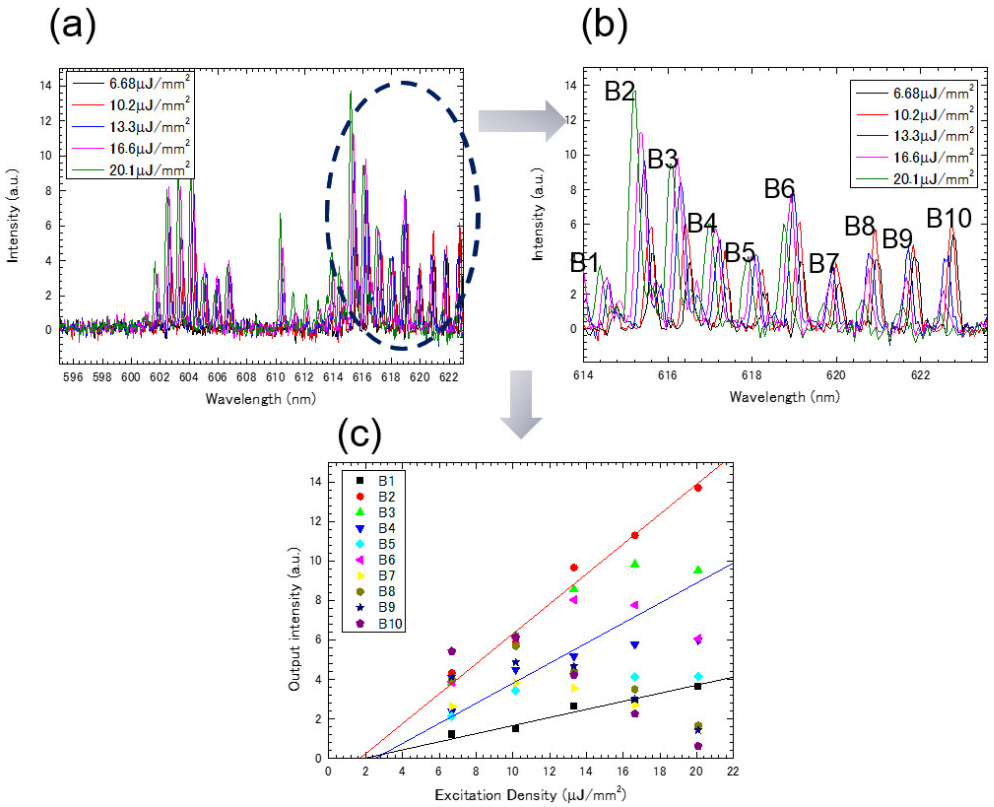

Figure 3.5: (a)Lasing spectra of non-etched Rhodamine590 doped microdisk (b) 10 mode (B1-B10) chosen from all modes peaks (c) input-output characteristics of B1-B10.

predicted by the refractive index dispersion with the optical gain, so we assumed that there is another reason caused by the thinner edge on the Rhodamine 590 doped microdisk. In order to verify the effect of angle on WGM, more explanation will be given in the next subsection.

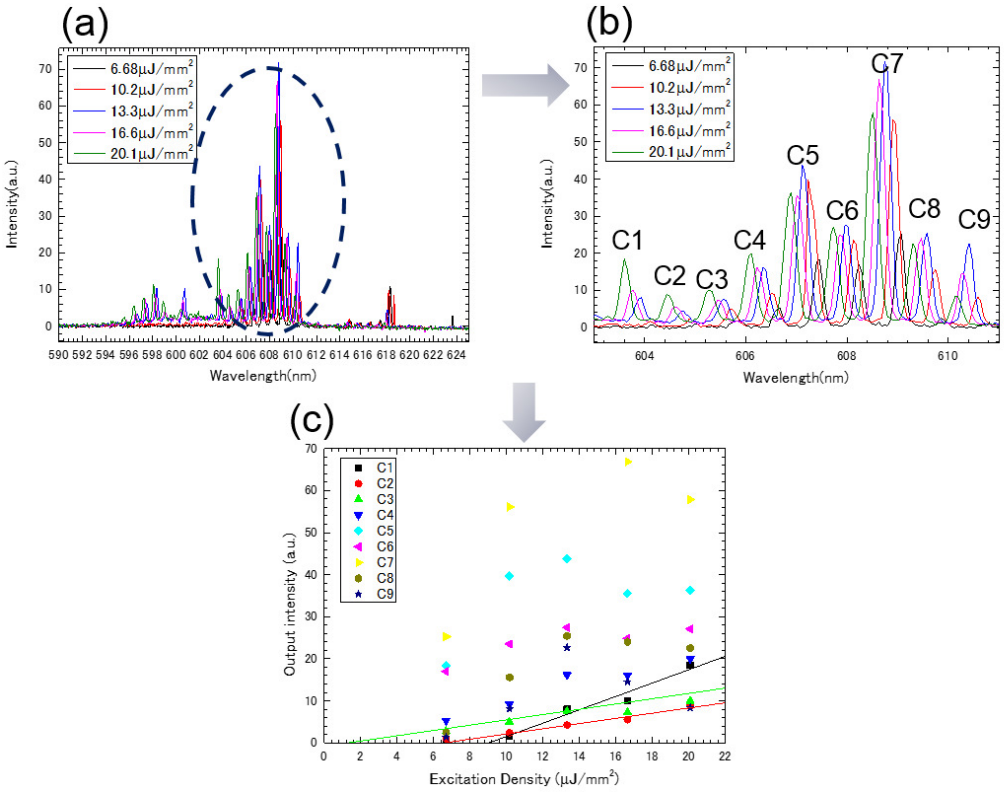

Figure 3.6: (a)Lasing spectra of etched Rhodamine590 doped microdisk (b) 10 mode (C1-C10) chosen from all modes peaks (c) input-output characteristics of C1-C10.

3.3. Correlations between WGWM spatial position and edge angle

3.3.1 Experiments

In order to further investigate the correlations between edge angle and WGM, different edge inclination angles disks are needed. Two different concentrations of 10 wt.% (DiskA) and 5 wt.% (DiskB) TZ-001 were used for fabricating two kinds of microdisks with different edge shapes. The printing processes of a polymeric microdisk are shown in figure 3.8 (a), in order to maintain the edge angle of disk,

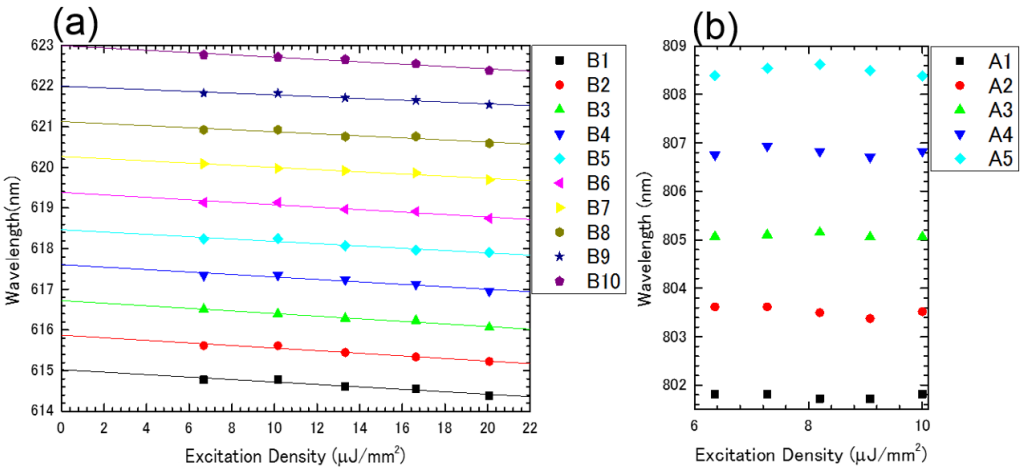

Figure 3.7: Spectrum stability with pumping intensity variation of (a) Rhodamine590 doped microdisk (b) LDS798 doped microdisk.

the etching step was omitted. In order to guarantee a same concentration for gain material, DiskA and DiskB were doped in Rhodamine 590 with concentrations of 5 mM and 10 mM. Figure 3.8 (b)(c) shows SEM picture of ink-jet printed microdisk. Based on the edge profiles which were took by atomic force microscope (AFM), the thicknesses of microdisks were about 1 μm. As shown in figure 3.9, the edge angles of the DiskA and DiskB were 8.4° and 13.1°, respectively. Because low concentration is more likely to cause coffee ring effect, solute concentration is more concentrated in the edge, so low concentration has a higher edge angle. However, this is not absolute. When the ink jet parameters are changed, different ejection velocities will lead to different shapes even in the same concentration. As mentioned in introduction section, it is no need a waveguide for coupling in active microcavities, hence active microcavities could be simply pumped and collected lasing signal based on a free-space measurement setup. The whole setup is basically the same as figure 3.3, but it will be explained again in the table 3.2.

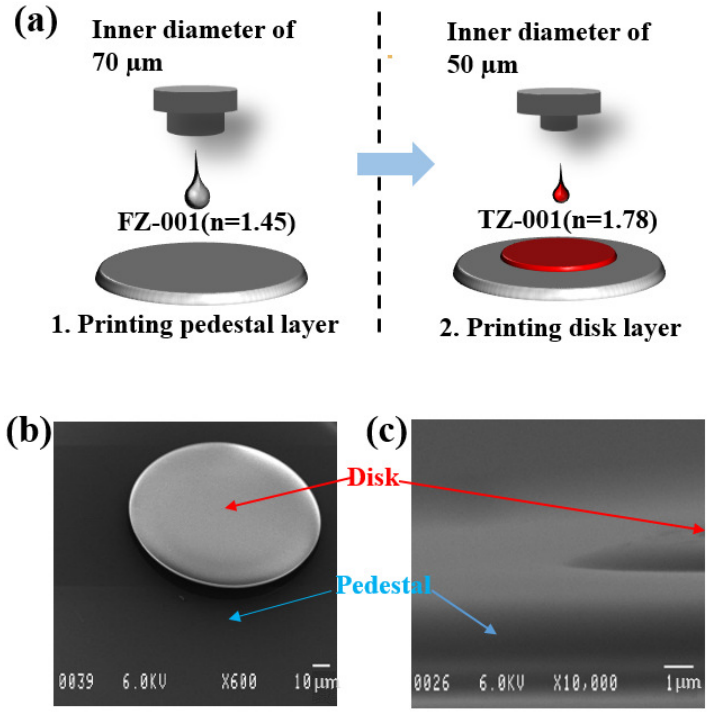

Figure 3.8: (a) The fabrication process of a wedge ink-jet printed microdisk laser based. The (b) top view and (c) side view SEM images of a microdisk.

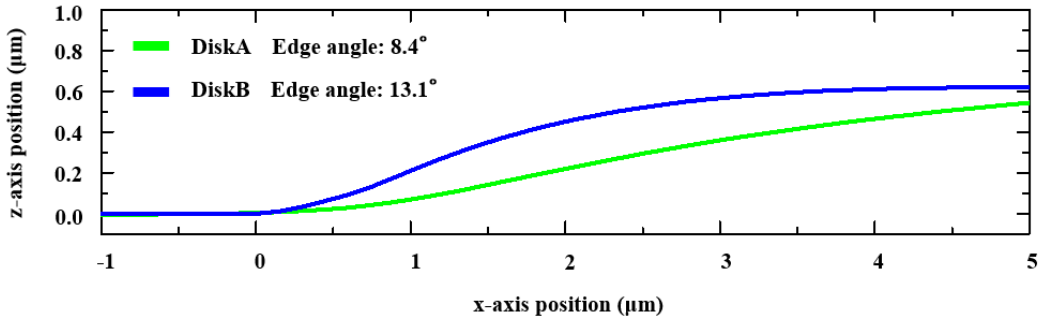

Figure 3.9: The edge profiles of ink-jet printed wedge microdisks (DiskA and DiskB).

3.3.2 Results and discussion

As it is shown in figure 3.11, the lasing spectrum of the DiskA and DiskB could be obtained at the pump energy density of 27.03 μJ/mm^2 with the microscope

Table 3.2: Pumping condition of microdisk lasers.

Conditions	Parameters
Pumping wavelength	532 nm
Pumping pulse duration	0.5 ns
Pumping pulse repetition	50 Hz
Pumping spot size(diameter)	350 μm
Integration time	10 seconds

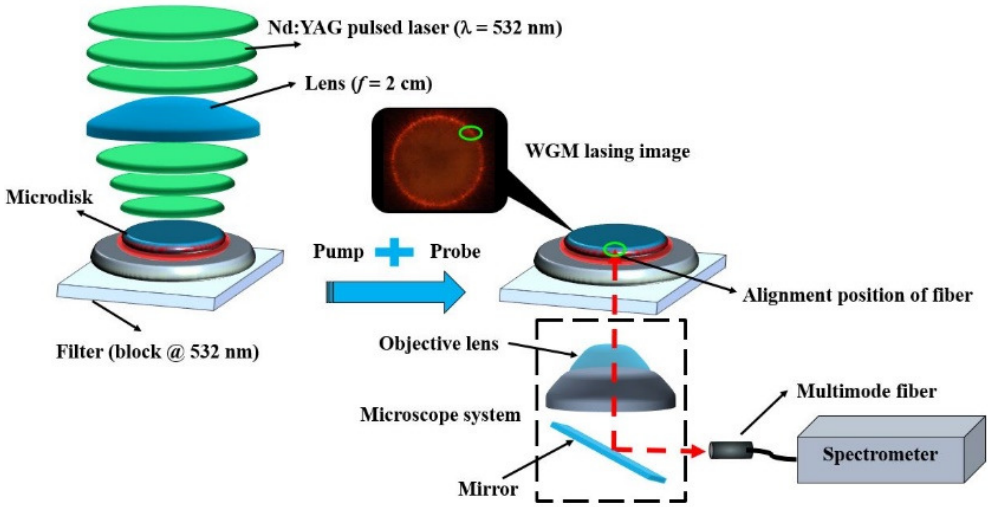

Figure 3.10: Experimental setup of pumping and detecting for a ink-jet printed wedge microdisk laser.

based free-space measurement setup. In this work, the wedge microdisk lasers with average lasing threshold of 5.5 μJ/mm^2 were used as experimental object. Since the transverse electric field component is dominant, TE mode tends to scatter towards the outer direction of the microdisk. Contrarily, due to the longitudinal electric field component is dominant, the TM mode tends to scatter towards the inner direction of the microdisk. In our setup, the lasing signals were collected by a multimode fiber which was placed out of plane (slightly away from the outer edge

of the microdisk). Therefore, the TE mode was captured preferentially, especially in the long wavelength region with low PL intensity, which was confirmed in the right region of the laser spectrum. on the other hand, in the short wavelength region of high PL intensity, enhanced signal intensity led to significant coexistence of TE and TM modes. This indicates that more TM modes can be collected in multimode fiber. It can be confirmed with enhanced peak intensity distributed between the FSR, which was shown in the left region of lasing spectrum. Herein, the FSR was observed by the TE modes in the long wavelength region. The lasing spectrum of DiskB (edge angle 13.1°) has a slightly larger FSR than DiskA (edge angle 8.4°). The insets illustration of figure 3.11 indicated the differences of resonance wavelength between TE modes and left adjacent TM modes. The average difference was 0.25 nm in DiskA, and the average difference was 0.35 nm in DiskB. In order to clarify the characteristics behind these differences, it is a feasible solution to study the effects of edge angle on WGM, because the distribution of lasing spectra is related to the edge formation of wedge-shaped microdisk. In the next subsection, the electric field distributions of WGMs in the wedge microdisk cavity were calculated using a numerical simulation method.

As mentioned in chapter 2, by using the Oxborrow's model with PMLs modified by Cheema, the electric field distributions of WGM in a wedge microdisk cavity can be calculated with finite element method (FEM) in COMSOL Multiphysics software [71–74].

The simulation model geometry of a wedge microdisk cavity is shown in figure 3.12. Herein, all of the microdisks show very small curves which can be approximated to linear ramps. The diameter and thickness of microdisk model were set as 120 μm and 1 μm respectively which is according to the actual microdisk sizes. In order to explore the WGM distributions near the edge of the wedge microdisk, the edge angle was set as θ which was varied from 2° to 89°. The distributions

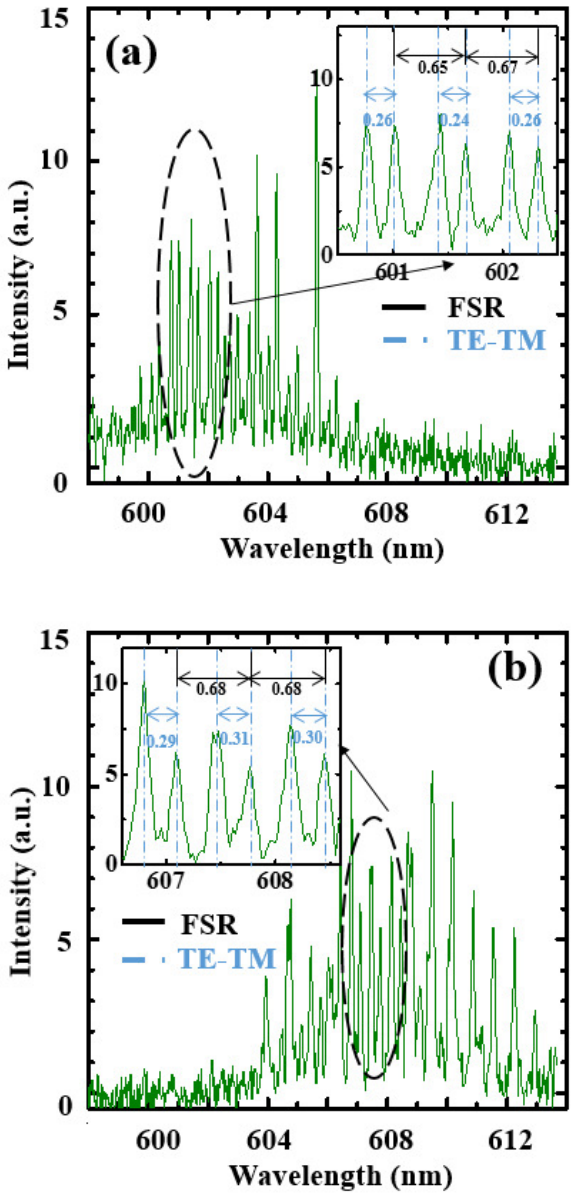

Figure 3.11: The lasing spectrum of the polymeric microdisk lasers with edge angles of (a) 8.4° (DiskA) and (b) 13.1° (DiskB).

of electric field of fundamental TE modes and TM modes at different edge angles were shown in figure 3.13 and 3.14, respectively. Herein, the azimuth angle

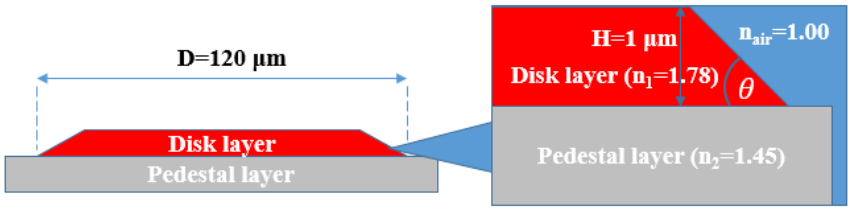

Figure 3.12: The simulation model of a ink-jet printed wedge microdisk.

number M was maintained at 950. According to figure 3.13 and 3.14, it was no difficult to find that the radial positions of TE and TM modes were moving toward to the inner direction of the wedge-shaped microdisk with the decreasing of the edge angle, and this directly affected the resonance wavelength to led shifts. In addition, the TM mode has a smaller radial position than the TE mode, which means that the TM mode has a shorter resonance wavelength.

The WGM position shifts of the TE and TM modes in the different edge angles is shown in figure 3.15 (a).The rainbow part in the figures(3.13,3.14) are the electric field distributions of WGM, and the color represents the intensity of the electric field (red is the strongest, blue is the weakest, as shown by the color contrast on the right side of each figure). In addition, the white arrow represents the direction of electric field vibration, which can help us to observe TE and TM modes. The radial position shifts increase with the increasing of edge inclination angles. This is because the edge inclination angle causes the mode far away from the outer rim of a disk. As it is shown in the figure 3.13 and 3.14, the smaller the edge angle is, the more significant the mode offset is relative to the outer edge of the microdisk. With the increasing of edge angle, TM mode show a larger mode position shift than TE mode, and it is consistent with the variations of resonance wavelength shifts in figure 3.15 (b). The maximum mode spatial position shifts of

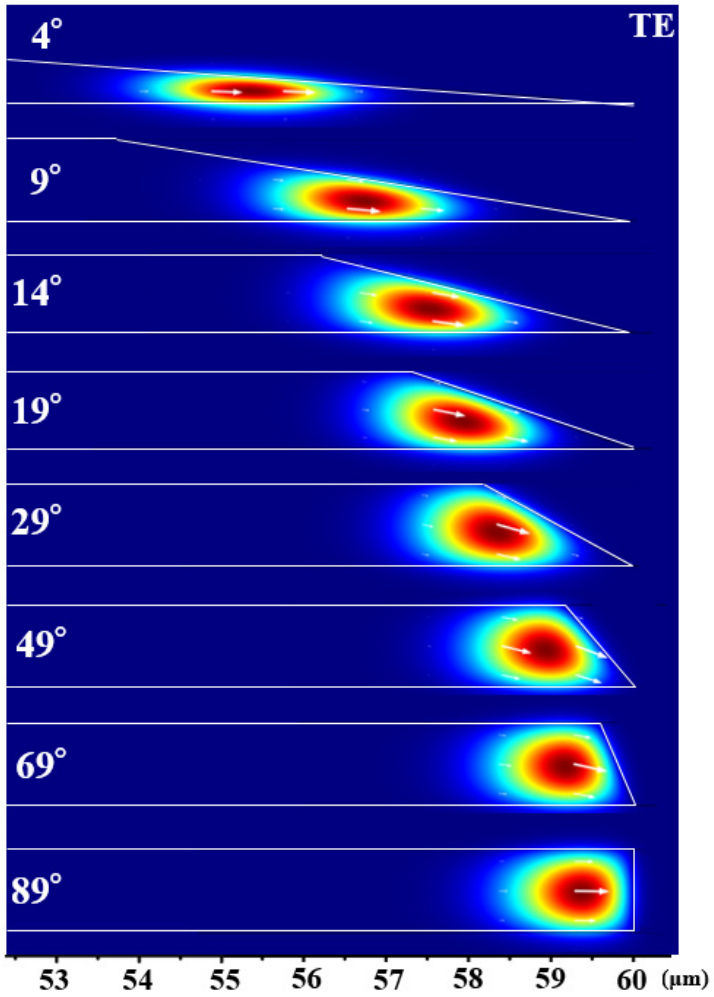

Figure 3.13: The electric filed distributions of fundamental order TE mode in wedge cavities with different edge angles.

TE mode and TM mode were 5.53 μm and 7.07 μm, respectively. The resonance wavelength shifts of TE mode and TM mode were 111.17 nm and 127.87 nm, respectively.

As shown in 3.16 (a), the variations of the FSR differences between the TE and TM modes is consistent with the position differences between TE and TM decrease with the increasing of edge angle. When the edge angle was 2°, the maximum

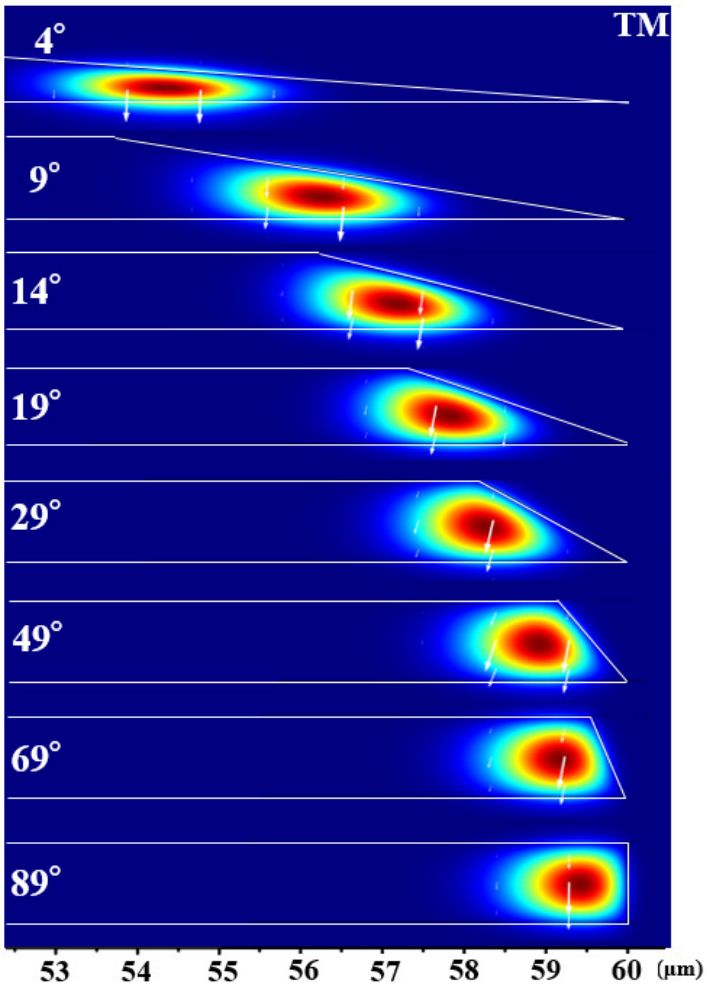

Figure 3.14: The electric filed distributions of fundamental order TM mode in wedge cavities with different edge angles.

position difference and maximum FSR difference between TE and TM modes were 1.49 μm and 0.03 nm, respectively. Another group of mode eigenfrequencies can be obtained when the azimuth angle number M was set as 949. The FSR were calculated by comparing the difference of resonance wavelength between M=949 and M=950 at different edge angles. With the increasing of edge angles, the FSRs increased which was shown in figure 3.16 (a). As the explanation, compared with

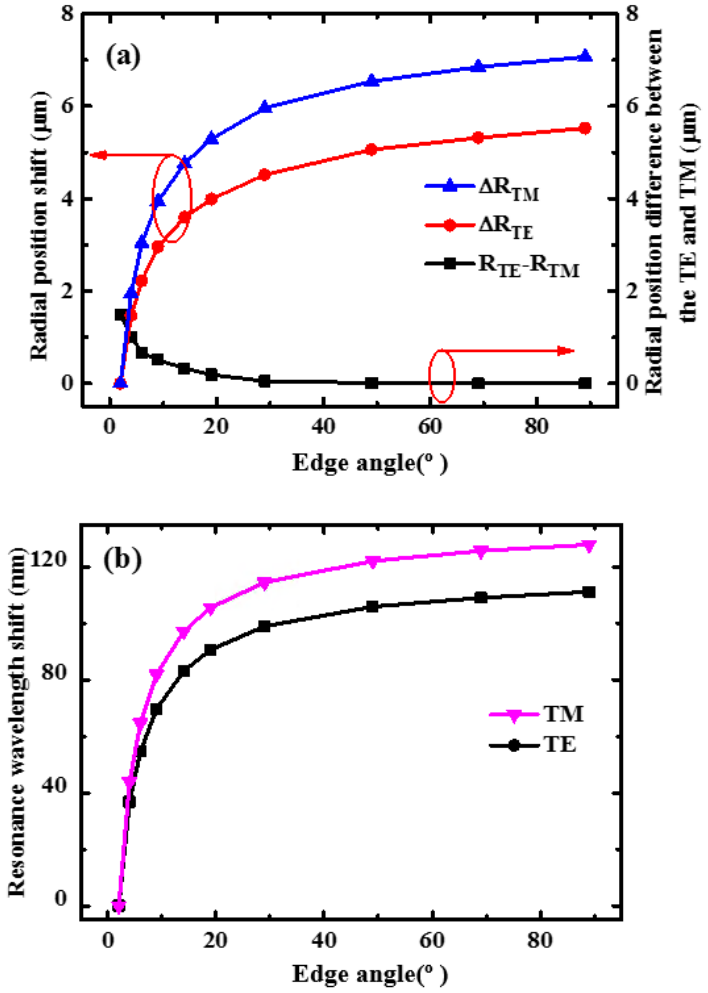

Figure 3.15: The correlations between (a)radial positions/(b)resonance wavelength shift and the edge angles.

the increasing of radial position, the variation of the FSR was dominated by the more remarkably increased resonance wavelength shift. In the experiment, the FSR of DiskB is relatively larger than that of DiskA. By considering the radial position difference of TE mode and TM mode, the resonance wavelength difference of TE mode and TM mode at different edge angles is simulated, which is shown in figure 3.16 (b).

When the edge angle was 2°, a 17.6 nm maximum resonance wavelength difference could be obtained. When the edge angle was set as 8.4° of DiskA edge angle, the average difference of FSR and resonance wavelength can be calculated as 0.617 nm and 5.8 nm, respectively. Therefore, the resonance wavelength difference between TE modes and TM modes can be calculated about 9.4 times of FSR. Therefore, the azimuth angle number difference between TE mode and the left adjacent TM mode was 9, and resonance wavelength difference between TE mode and the left adjacent TM mode was 0.247 nm. When the edge angle was 2°, a 17.6 nm maximum resonance wavelength difference could be obtained. Similarly, when the edge angle was set as 13.1° of DiskB edge angle, the average difference of FSR and resonance wavelength can be calculated as 0.635 nm and 4.1 nm, respectively. Therefore, the resonance wavelength difference between TE modes and TM modes can be calculated about 6.46 times of FSR. Therefore, the azimuth angle number difference between TE mode and the left adjacent TM mode was 6, and resonance wavelength difference between TE mode and the left adjacent TM mode was 0.3 nm. It was observed in experiments that the simulation result of resonance wavelength difference between TE mode and the left adjacent TM mode was very close to the experimental result.

The experiment can only explain the relation between WGWM and edge angle to a certain extent. The experiment of completely proving shape dependence is not done in this thesis, and this is mainly due to two reasons that limit the experiment. One reason is that the position moving of WGWM is only hundreds of nanometers which is too small to observed in a microscope. The other reason is that it is very difficult to realize the shape control with ink-jet method. The edge shape of ink-jet printed microdisk is mainly depends on the contact angle of printed droplet. The contact angle depends on the type of solvent, the concentration of solute and the hydrophobicity of the substrate. When we try to change the contact

angle of droplets, the size usually changes at the same time. So it's hard to make multiple sets of disks with different angles and identical sizes. However, it is possible to accurately control and optimize parameters through a large number of experiments in the future.

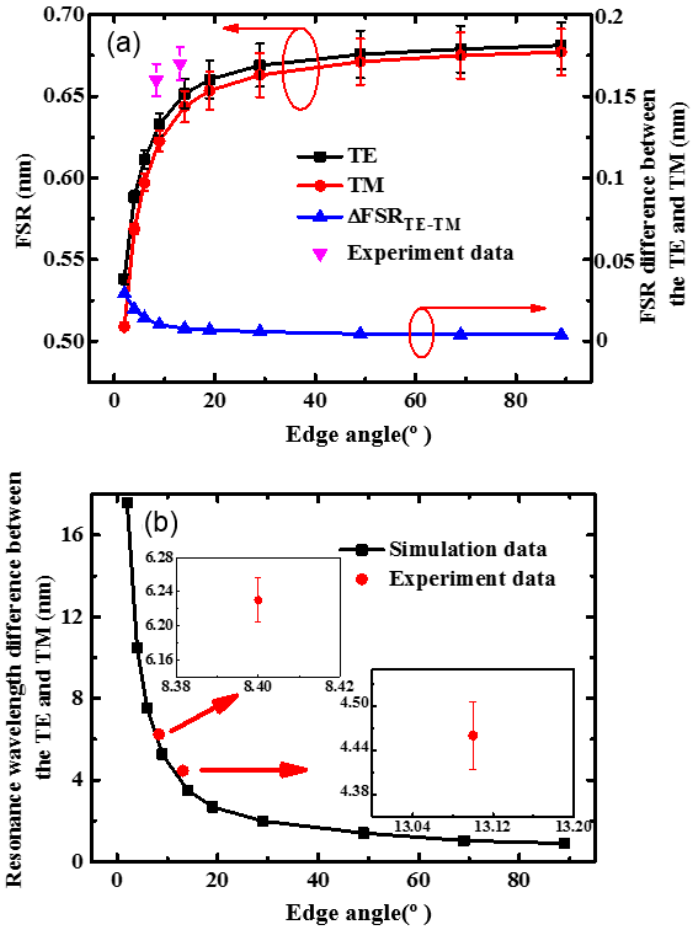

Figure 3.16: (a)The correlations between the edge angles and FSR of fundamental TE and TM modes. (b) The correlations between the edge angles and resonance wavelength differences between fundamental TE and TM modes. Black dots represents simulation data and red dots represents experimental data. The inserts indicate the error bars of experimental data.

The variations of Q-factors and F-factors at different edge angles can be shown

in figure 3.17. The Q-factor and F-factor were slightly decreasing with the increasing of edge inclination angle. This is because when the resonance mode become far from the outer edge of the disk, the radiation loss of the mode decreases. Our result is different with the work reported by Gandolfi *et al* [84], because only absorption loss and radiation loss were taken into account while the coupling loss was not taken into account in our simulation [48]. Herein, we omitted the scattering loss because the surface roughness (RMS) of a ink-jet printed polymeric wedge microdisk was measured to be about several nanometers by AFM. As the intrinsic absorption of material, the extinction coefficient of the disk layer (TZ-001) was set as 9.74×10^{-8} at wavelength of 600 nm. Under the consideration of our device configuration, the optical loss caused by radiation loss can be calculated as about 0.018 cm^{-1}. Due to the increasing of radiation loss, the Q-factors of TE modes were slightly lower than TM modes. As mentioned in chapter 2, the F-factors can be calculated via equation

$$\mathrm{F} = \mathrm{Q} \times \frac{FSR}{f_0}$$

to explore the effect of microdisk edge angles on the performance parameters of wedge microcavities [52], where f_0 are the eigenfrequency of WGM. As it was shown in figure 3.17 (b), when the edge angle was larger than 4°, the F-factor of TM mode is comparative to that of TE mode, which indicates that TM mode has competitive laser intensity compared with TE mode. The changes of F-factor with edge angle is affected by eigenfrequency, Q-factor, and FSR. The physical and geometrical structure of the wedge-shaped microdisk cavity made the effective optical loss of TE mode started at a faster rate near the 10° inclination angle. As shown in figure 3.17 (a), the quicker rate of Q-factors decreasing in TE mode caused the quicker rated of variation in effective optical losses near edge angle of 10°. When the edge angle is around 10°, the Q factor decreases faster than

the FSR, as well faster than eigenfrequencies. Hence, a minimum value can be observed in TE mode at 10° edge angle (figure 3.17 (b)). To investigate the

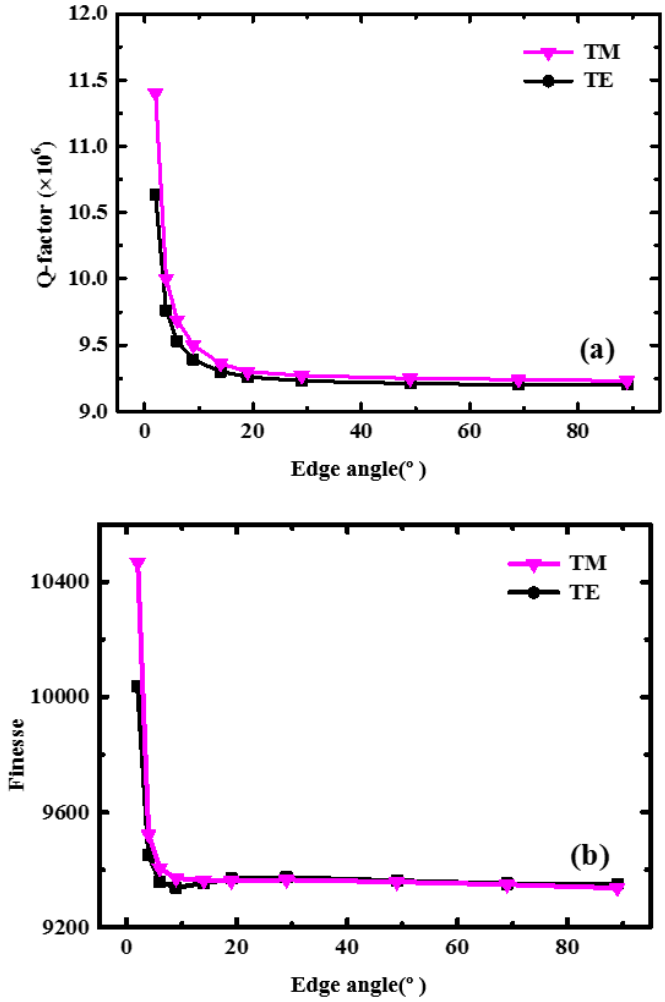

Figure 3.17: The correlations between edge angles and (a) Q-factors/(b) F-factors on fundamental mode.

correlations between the fundamental mode and the high order modes at different edge inclination angles, the second order mode of the WGMs were calculated. The simulation results show in figure 3.18 and 3.19. Figure 3.18 shows the electric eld distributions of the second order TE mode at edge inclination angles of 89, 69,

49, 29, 19, 14, 9 and 4 degrees. Figure 3.19 shows the electric eld distributions of the second order TM mode at edge inclination angles of 89, 69, 49, 29, 19, 14, 9 and 4 degrees. The results are same as results of fundamental modes, the spatial positions of the TE and TM modes are shifting inner rims of the wedge microdisk resonators with the decrease of edge inclination angles.

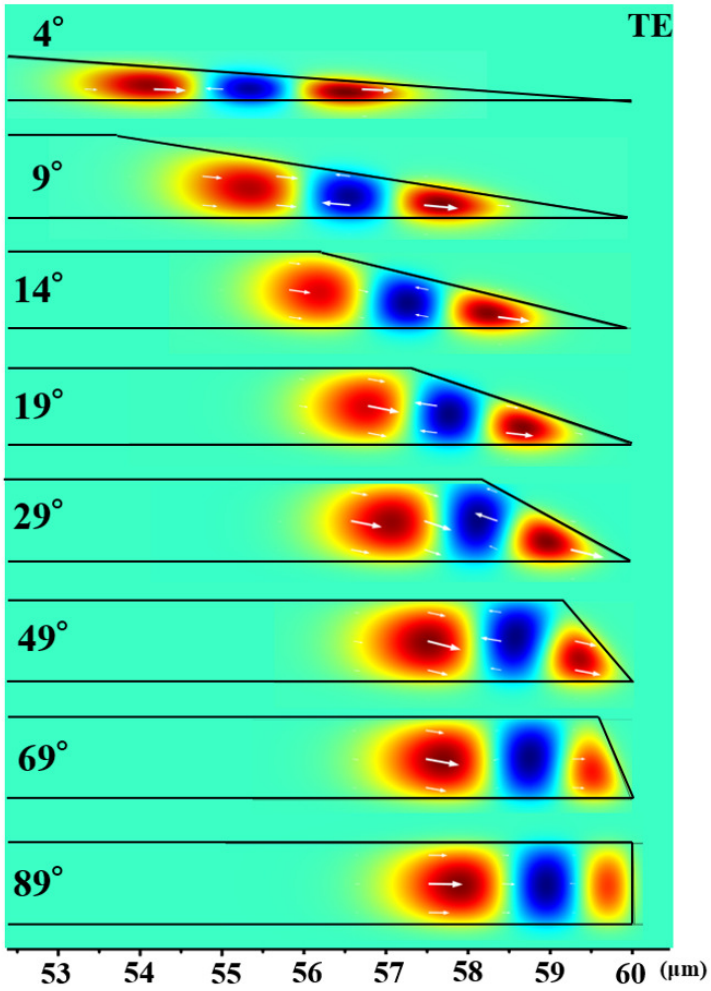

Figure 3.18: The electric filed distributions of the second order TE mode.

To further investigate the competition correlations between the fundamental mode and the high order modes at different edge inclination angles, the quality

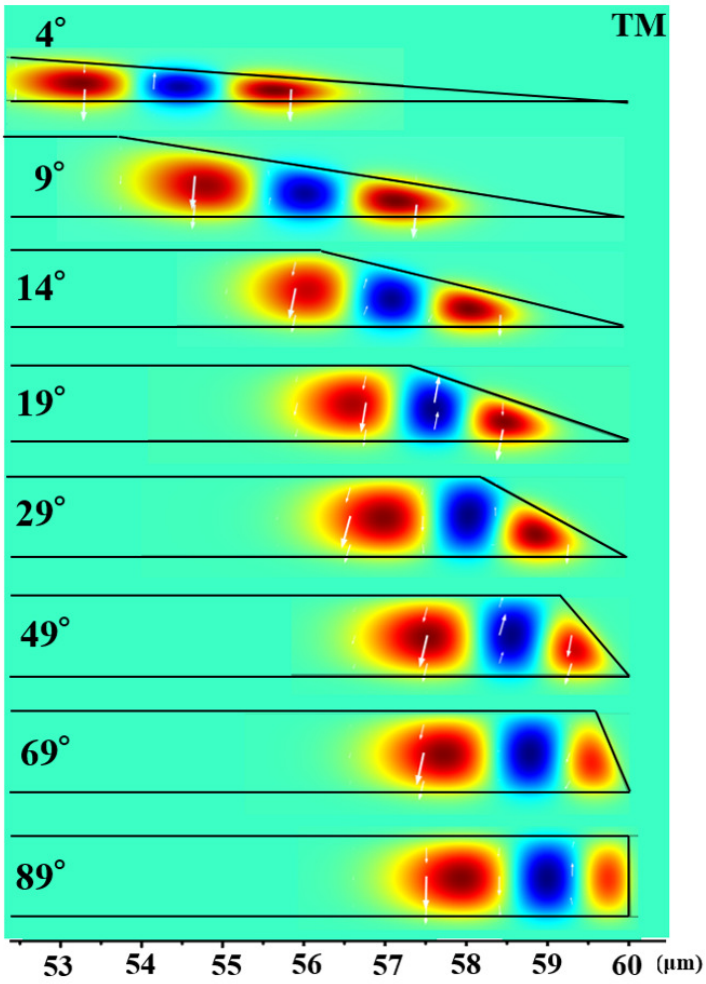

Figure 3.19: The electric filed distributions of the second order TM mode.

factors of the WGMs were quantified. As mentioned in chapter 2, the total Q-factor can be obtained by calculating absorption loss, radiation loss and scattering loss. The equation as following [65]

$$Q^{-1} = {Q_{Abs}}^{-1} + {Q_{Rad}}^{-1} + {Q_{Sca}}^{-1}$$

where Q is the total Q-factor, Q_{Abs} is the Q-factor corresponding to absorption

loss, Q_{Rad} is the Q-factor corresponding to radiation loss, and Q_{Sca} is the Q-factor corresponding to scattering loss. The Q-factor due to the radiation loss can be calculated via

$$Q_{Rad} = \frac{\omega_{real}}{2\omega_{imag}}$$

where ω_{real} and ω_{imag} denote the real and the imaginary part of the eigenfrequency of WGM resonance. Based on the axisymmetric model with PMLs, the Q-factors due to the radiation losses were calculated at different edge inclination angles. The results were shown in figure 3.20. The upper group of the three lines is for TM mode, and the lower group of the three lines is for TE mode. The result shows that the high order modes have a slightly higher Q-factors in comparison with the fundamental mode when the edge inclination angles are less than 19°, which illustrates that the mode competition would be aggravated at small edge inclination angles. On the contrary, the fundamental mode is more prominent than the high order modes in mode competition at large edge inclination angles due to its small mode volume. Therefore, the competition between the fundamental mode and the high order modes can be another reason to the phenomenon of the linewidth broadening of the lasing spectrum in a wedge microdisk laser although this effect is very small.

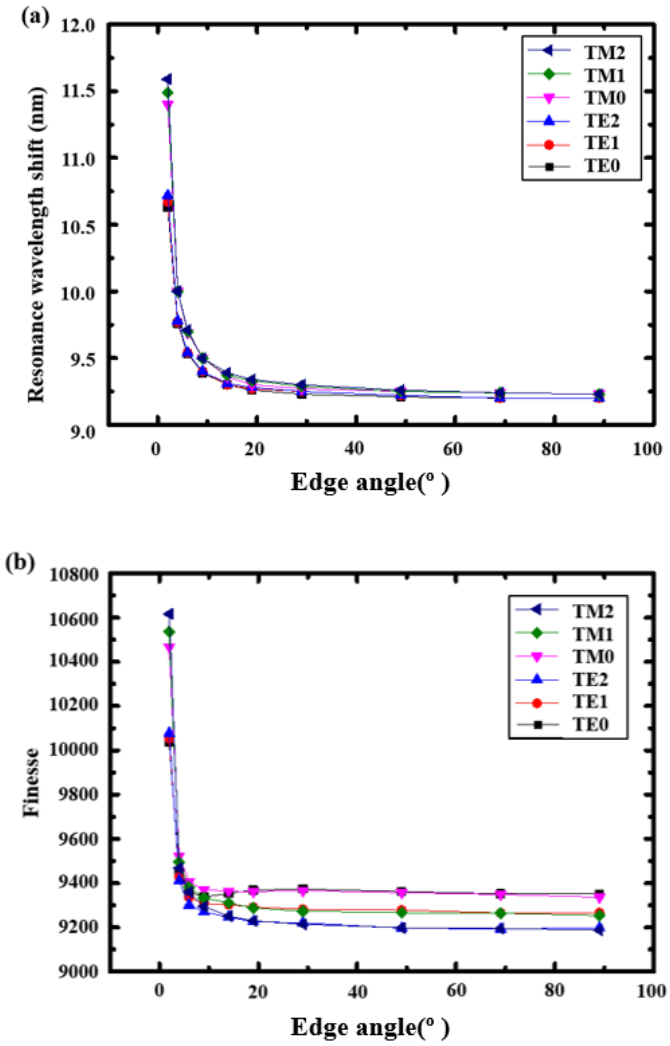

Figure 3.20: The correlations between edge angles and (a) Q-factors/(b) F-factors on different order modes.

3.4. Summary

In this chapter, a WGM lasing with a low threshold was achieved by dye doped microdisks with ink-jet printing method, and the correlations between WGWM spatial position and edge angle were theoretically demonstrated.

The WGM lasing around 800 nm and around 600 nm were demonstrated by dye of LDS798 and Rhodamine590, respectively. Then, mode shift of 1.55 nm (LDS798 dye-doped)/0.83∼0.89 nm (Rhodamine590 dye-doped) were also confirmed. Low lasing threshold of 2.80 μJ/mm^2 (LDS798 dye-doped) and 2.00 μJ/mm^2 were also obtained. Shifts of resonance wavelength were observed only on Rhodamine 590 doped microdisk.

To clarify the causes of wavelength shift, two microdisks lasers with different edge angles of 8.4° and 13.1° were fabricated by ink-jet method. By using a microscope based free-space setup, the lasing spectrum of the two microdisk were obtained. In the information of lasing spectrum, it showed that the microdisk with a larger edge angle always have a larger FSR and a smaller resonance wavelength difference between the fundamental TE mode and TM mode. By simulation with the Oxborrows model for cross-section WGM cavity, the behaviors above were confirmed. The relations between the TE mode and left adjacent TM mode was theoretically demonstrated by combining with the nearly equivalent Q-factor and F-factor variations. In addition, it was found that the spatial position of WGWM moves to inside of radial direction in a wedge microdisk with the decrease of edge angle, and TM modes move more significantly than TE mode.

The results show that if the wedge angle of WGWM cavity is optimized, the sensitivity can be adjusted by controlling the spatial position of WGWM. For example, the small edge angle cavity is suit for biosensing since it has a larger evanescent light area. The sensing applications with both large angle WGM cavity

and small angle WGWM cavity will be discussed in next chapter.

Chapter 4

Sensing applications based on WGM microring lasers and WGWM microdisk lasers

4.1. Introduction and purpose

As mentioned in foregoing chapters, the WGWM microcavities can be applied to sensors especially for surrounding environment sensing since they have a wider evanescent field. The mechanism of WGWM sensing is that the evanescent field be affected with the surrounding environment. It causes the resonance wavelength shift due to the change of molecular adsorption or refractive index. By tracking and analyzing a wavelength shift from a spectrum of one microcavity, some information can be obtained. In chapter 3, we discussed the spatial position shift of WGWM caused by the change of edge angle. The shift of WGWM spatial position will directly affect the evanescent filed and thus affect the sensing performance. Although a small angle WGWM sensor has a wider evanescent field, a too small

angle will lead to a TE and TM mode splitting which is shown in the result of chapter 3. Hence it is more important to consider the mode stability when using the change of the cavity itself for sensing. Based on the results, it is not difficult to infer that small edge angle WGWM cavities are more suitable for surrounding environment sensing since larger evanescent fields are suitable for molecular adsorption detection, and normal WGM cavities are suitable for self environment sensing since they have more stable modes. Since a normal WGM cavities for self environment sensing is much easier to achieve, we initially developed a WGM microring sensor to lay the foundation for WGWM sensing. The reason why we choose the reconfigurable microring laser based on ring groove platform is that, the groove platform can be filled with same material as ink of ink-jet method. This will help us to simply test the feasibility of active laser as a sensor with same conditions.

Generally, biosensor is one of the most typical examples of surrounding environmental sensing. For optical biosensors, which can be divided into fluorescence-based biosensors [86] and label-free biosensors [87]. A fluorescence-based biosensing is usually achieved by entering cells with fluorescent probes, labeling only specific proteins and converting their functions into biosensors. Although fluorescence-based biosensors are very common, they still have many limitations because some of the fluorescent labeled proteins are toxic. Compared with fluorescence-based biosensors, label-free biosensors have the advantages of direct detection/quantitative analysis of biomolecules. They are easy to operate and can be used for single-molecule detection. So far, label-free optical sensors are useful for many advanced applications [58], such as clinical diagnostics [88], environmental monitoring [89, 90], and public health [87]. In label-free sensors, Surface Rlasmon Resonance (SPR), optical waveguide and WGM resonator are the mainstream technologies. Usually the sensitivity of these sensors is evaluated by refractive index unit

(RIU). The SPR sensor can demonstrate a sensitivity of $10^{-5}\sim10^{-7}$ RIU [91], and optical waveguide sensor can demonstrate a sensitivity of $10^{-4}\sim10^{-7}$ RIU [92]. Although WGM sensors were reported with sensitivity of $10^{-6}\sim10^{-7}$ RIU [93–95], the sensitivity of WGM sensors can achieve 10^{-9} RIU with high Q-factor in theory.

The most common research of WGM cavities are usually based on passive microcavities. For detecting a passive microcavity, it requires an optical waveguide [96], a tapered optical fiber [97], or a prism [98] for coupling. The coupling of microcavities needs strict conditions of a very precise coupling distance and phase matched element size. Current technologies can achieve high coupling efficiency and high Q-factor with passive WGM cavities, but the high requirements for these coupling conditions may limits WGM cavities to some daily life applications. Besides, the signal of lasing spectrum is easy to be unstable due to the influence of cavities position moving [99]. Free-space measurement setups can solve the problems above and make it possible to realize such passive-cavity based optical sensor [100, 101]. However, polarization dependent directional scattering and lower signal becomes new problems. On the other hand, optical gain materials doped active microcavities can solve the problems above and realize sensing devices with high sensitivity [80, 102]. It is especially suitable for remote pumping and collecting lasing signals or amplified spontaneous emission (ASE) through free-space optics. Generally, those WGM active cavities based sensors be fabricated by subtractive method such as lithography. However, subtractive methods limit the performance of WGM active cavities due to the drawbacks of high temperature treatment and complex process. In these consideration, we realized an active microcavity based on a dye doped microdisk with a additive fabrication of ink-jet printing method in our previous work [48]. Compared with subtractive method, this ink-jet technology based additive fabrication has merits of arbitrary substrate, room temperature fabrication and simple doping. Therefore, ink-jet

printed active microdisks are very potential for a high sensitive label-free biosensor.

On the other hand, there are many sensing applications based on the variations of RI of a cavity itself. For example, temperature sensing can apply the thermometry technologies to many applications in a variety of important fields. Nowadays, different nanothermometers based on temperature dependent optical properties, such as a photoluminescent nanothermometer composed of quantum dots (QDs) [103], a green fluorescent probe based on nanoparticles [104], and a thermo-responsive polymer-coated optical microfiber [105], are applied to detect environmental temperature at cellular levels in human body temperature range of 35$\sim$42 $^{\circ}C$. A high sensitive on-chip temperature sensor is very useful for multifunctional biological monitoring or treatment, but most of the temperature sensors mentioned above have low sensitivities and are difficult to be integrated on-chip. Hence, it is worth to develop a on-chip high sensitive temperature sensor.

With the merits of rapid response time, easy integration, and immunity to electromagnetic radiation [106–108], passive optical WGM cavities with high Q-factors and small mode volumes have attracted significant attention as common sensing units in the past decade. Generally, various host materials of silica [109],silicon [52] and polymer [110] can be used for fabricating on-chip microcavities.Optical temperature sensing is mainly realized by spectral shifts of WGM cavity due to the thermal optics (TO) and thermal expansion (TE) effects of the cavity materials and the surrounding environment [111–113]. For example, relying on the compatibility of the CMOS fabrication process, silicon-based temperature sensors are favored for their excellent thermal conductivity($\sim$149 W/(mK)) [114–116]. However, due to the low TO coefficient of silicon ($\sim 1.8 \times 10^{-4}$ K^{-1}), the sensitivity of temperature sensor based on pure silicon ring cavity is limited to about 80 pm/$^{\circ}C$ [117–119].

Moreover, silica is another material commonly used to fabricate microring cavity, but it has more lower temperature sensitivity and TO coefficient ($\sim$1 $\times$ 10^{-5} K^{-1}) [120].Recently, a silica microring cavity was coated with a polydimethylsiloxane(PDMS) which demonstrated a high temperature sensitivity of 151 pm/$^{\circ}C$ [121].In most of passive WGM cavity-based temperature sensors, the spectrum detecting are required an optical fiber taper, a waveguide, or a prism for optical coupling, which make passive cavities suffered from high requirement of precision positioning the cumbersome system and susceptible to mechanical vibrations [122].As shown in table 4.1, some of those microring-based temperature sensors were summarized.Compared to passive cavity, an active cavity-based temperature sensor can realized a simpler measurement setup since free-space optical setup can be used to instead of coupling system. In addition, it can reduce the spectral linewidth and improve the sensitivity limitation of an active microring-based temperature sensor by doping gain material [80, 124].

In this chapter, a large edge angle WGM microring for temperature sensing is demonstrated, and a small edge angle WGWM microdisk for biosensing is investigated. The large edge angle WGM microring based on a silica microring groove host as the clad layer and a cured Rhodamine 590 doped polymer as the core layer. In this work, several optical properties, including lasing spectrum, input-output characteristics and photostability of SU-8 and TZ-001 WGM microring lasers, were respectively analyzed to estimate the feasibility of their use as temperature sensing elements. The result demonstrated a high-sensitivity temperature sensor, and it proved that the TZ-001 based active polymeric microcavity laser can be applied for sensor. Based on this result, the development of a surrounding environment sensor based on ink-jet microdisks was carried out. With the ink-jet printed microdisk, the stability in water was proved and the peak shift due to protein adsorption was also confirmed. In addition, the thickness of adsorbed

Table 4.1: Comparison of the characteristics of ring resonator-based temperature sensors.

Type	Sensitivity ($pm/^{\circ}C$)	Q-factor	Comments (Advantages: A; Drawbacks: D)
Silicon ring microcavity [114]	83	2×10^4	A: easy integration; CMOS processes compatibility. D: low sensitivity; waveguide coupling.
SU-8 ring microcavity [115]	92.5	3.3×10^4	A: easy integration; CMOS processes compatibility. D: low sensitivity; waveguide coupling.
Silicon ring microcavity [123]	77	5.2×10^4	A: easy integration; CMOS processes compatibility. D: low sensitivity; waveguide coupling.
PDMS-coated silica ring microcavity [121]	151	1.5×10^6	A: high Q-factor; high sensitivity; D:complex fabrication processes; fiber taper coupling.
Doped SU-8 ring laser [55]	228.6	1.8×10^4	A: high sensitivity; easy integration; free-space probing and readout. D: low detection limit.
Doped TZ-001 ring laser [55]	85.5	1.5×10^4	A: easy integration; free-space probing and readout; small footprint; D: low sensitivity.

protein was calculated with numerical simulation. These investigations show a feasibility for ink-jet printed WGWM specific biosensor. (Two partial contents of this chapter have been at Applied Physics Letters and CLEO Europe 2017,respectively.) [55, 56] (Reproduced from [55], with the permission of AIP Publishing.)

4.2. WGM microring lasers for temperature sensing.

4.2.1 Experiments

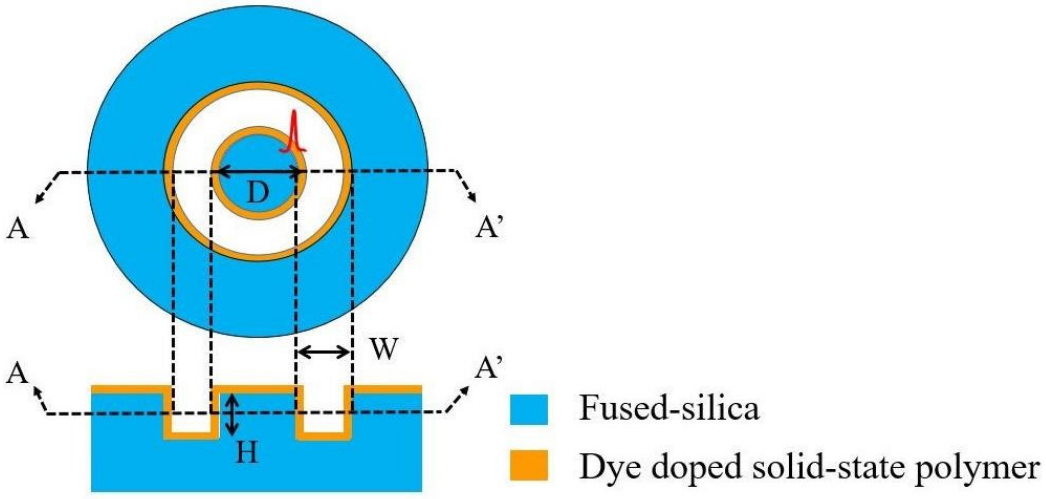

Figure 4.1: Top view and cross-section view of a dye-doped solid state polymer microring laser.

In order to lay the foundation for WGWM sensing, we firstly want to develop a normal WGM sensor for test the feasibility of active microcavity laser. Herein, we chosen the the reconfigurable microring laser based on ring groove platform as the test object since the groove platform can be filled with same material as ink of ink-jet method, and it will help us to simply test the feasibility of active laser

as a sensor with same conditions. Similarly, for easy demonstration, we chosen the temperature as sensing object because self environment sensing is easy to demonstrate with normal WGM cavity. In order to demonstrate a large edge angle WGM temperature sensor, a solid-state polymeric microring laser was used. This polymeric microring laser was based on a fused silica host platform with microring groove shape which can realize a nearly 90 degree edge angle. To achieve WGM lasing, the fused silica host and 6G-doped polymer were used as a cladding layer and a core layer, respectively. The top and cross-section schematic of microring is shown in figure 4.1.

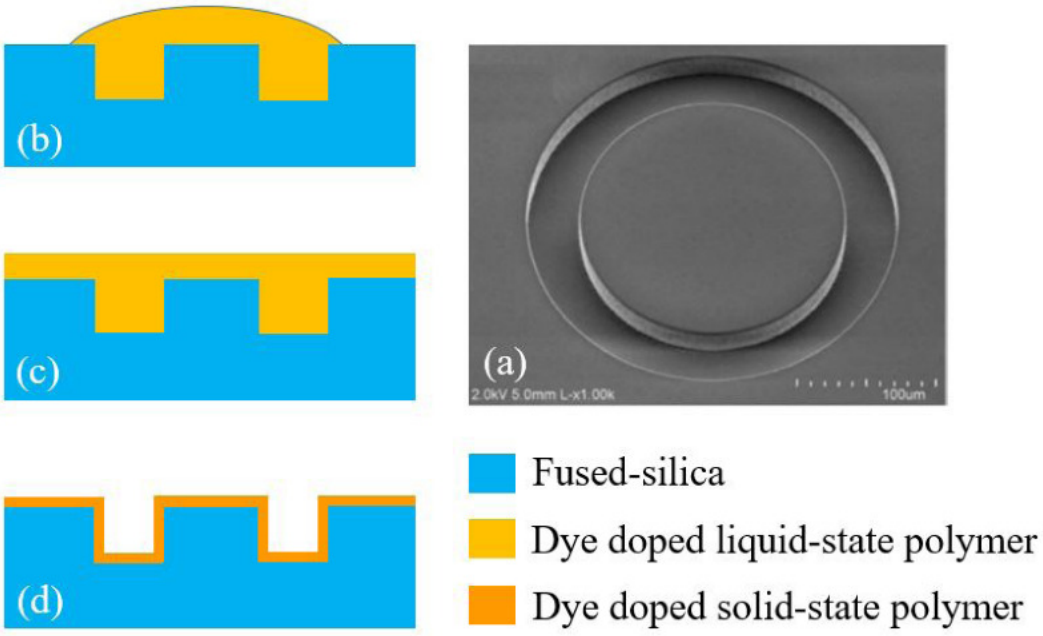

Figure 4.2: (a) SEM image of a fused silica microring cavity host with a groove shape. (b)-(d) Cross-section views of a dye-doped liquid-state polymeric microring in the fabrication process of (b) dripping; (c) spin-coating; (d) drying.

The SEM image of the microring groove platform is shown in figure 4.2 (a) (Before the polymer deposition process). The width and height of the microring

groove were 40 μm and 30 μm, respectively. And the central part diameter shaped silica is 220 μm. The detail fabrication process were shown as figure 2.4 and mainly utilized conventional photolithography and etching technologies. The fabrication method of the polymeric core layer were shown in figure 4.2 (b) to (d). Briefly, the polymer microring resonator was formed using a polymer with a higher RI than the silica groove platform. Polymers as matrix materials of microring can be easily dissolved by organic solvents, so the substituted dye-doped polymers with different emission wavelengths and refractive index can be re-deposited as needed.

In this experimenttwo kinds of polymer were used as matrix material of microring. The preparation of the microrings of these two materials is shown in the table 4.2. For the R6G-doped SU-8 microring laser, Su-8 solution with 1mM R6G was spin-coated on the microring groove platform and baked at 95 $^{\circ}C$ for 15 minutes to dried up. For the R6G-doped TZ-001 microring laser, 10 wt.% TZ-001 solution with 5mM R6G was spin-coated on the microring groove platform and placed at room temperature to dried up. The reason for not choosing baking process was that TZ-001 is brittle and prevents cracks caused by excessive temperature.

Table 4.2: The preparation of the microrings.

Microring	Matrix solution	Dye solution	Volume ratio of Matrix solution to Dye solution	Drying process
SU-8 ring	SU-8 solution	R6G 10mM	9:1	Baked at 95 $^{\circ}C$ for 15 minutes
TZ-001 ring	TZ-001@ cyclohexanone 10 wt.%	R6G 5mM	4:1	Placed at room Temperature overnight

As a commonly used commercial photoresist with a refractive index of 1.6

at 590 nm, SU-8 was preferred for use in a mixture with R6G as the core layer of a polymeric WGM microring laser. Measurement of the R6G-doped polymeric microring laser was performed with a free-space optics measurement setup. Details of this system are provided in figure 4.3.

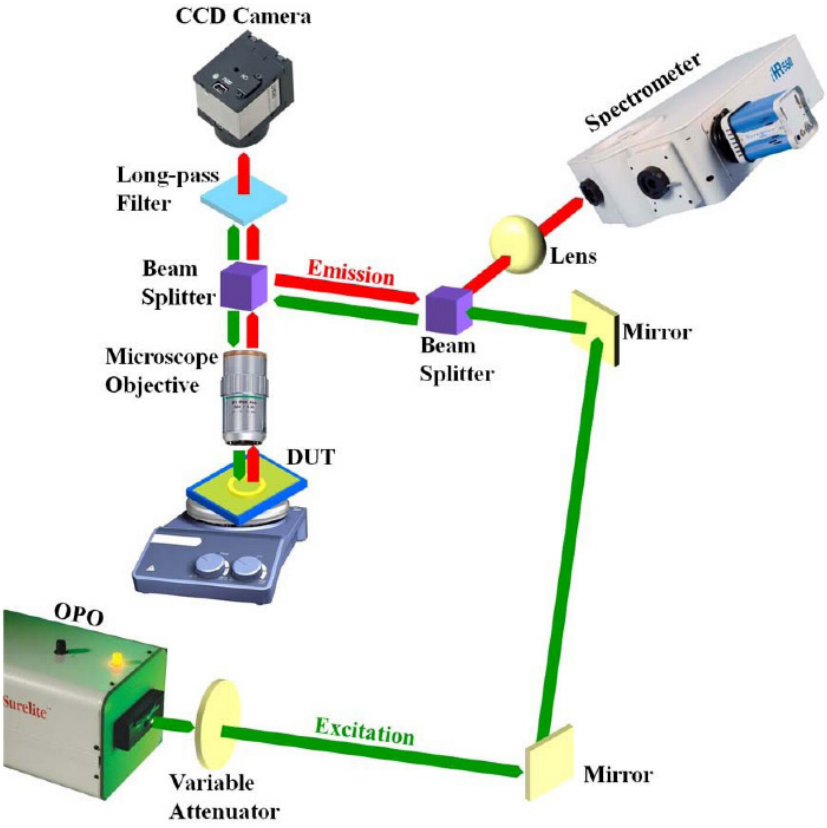

Figure 4.3: Measurement setup of the dye-doped polymeric microring laser-based temperature sensor.

The pumping source was used a pulse laser with an optical parameter oscillator (OPO) at 532 nm wavelength, the pulse duration and repeat rate were 5 ns and 20 Hz, respectively. A variable attenuator was used to adjust the pumping power. Pumping light was focused on a microring to pumping the microring. Once pumping power was over the lasing threshold of the microring, the lasing

signal go through the beam splitter and finally was collected by a spectrometer (Horiba 550,2400 l/mm grating). A hot plate placed under the fused-silica wafer was used to vary samples temperature.

The lasing spectra of a R6G-doped SU-8 polymeric microring laser is shown in figure 4.4 (a). And the FWHM of the lasing peak was 0.034 nm at wavelength of 597.567 nm, and this is limited by the resolution of spectrometer($\sim$0.03 nm). The Q-factor for this R6G-doped polymeric microring laser was calculated as 1.76 $\times 10^4$ by using the equation of the Q-factor mentioned in theory chapter(Q $=\lambda/\Delta\lambda$) [125]. In the spectrum, the a FSR of 0.3 nm was observed, and a radius of the microring about 115.4 μm can be calculated by FSR equation. The calculated value of this radius is close to the inner circle diameter of the host, hence the lasing signals were main from the inner microring cavity.

4.2.2 Results and discussion

The lasing threshold and spectral stability of the polymeric microring laser were characterized to investigate the feasibility of the R6G-doped SU-8 polymeric microring laser as a high sensitive temperature sensor. Figure 4.5 (a) shows the lasing threshold of SU-8 polymeric microring which was measured to be 1.28 μJ/mm^2. The spectral stability was illustrated in figure 4.6 (a) which was investigated under a uninterrupted pumping with a pumping intensity of 75.7 μJ/mm^{2}about 60 times of the lasing threshold).These laser spectrum were collected between adjacent measurements at 30 seconds intervals in 10 measurements. They show that SU-8 polymeric microring lasers have a very good spectral stability. Furthermore, as it was shown in figure 4.6 (b) a spectral shift of just less than 0.011 nm at lasing peak wavelength of 589.12 nm even under an very high pumping intensity.

As mentioned in introduction section, the temperature sensing is achieved by

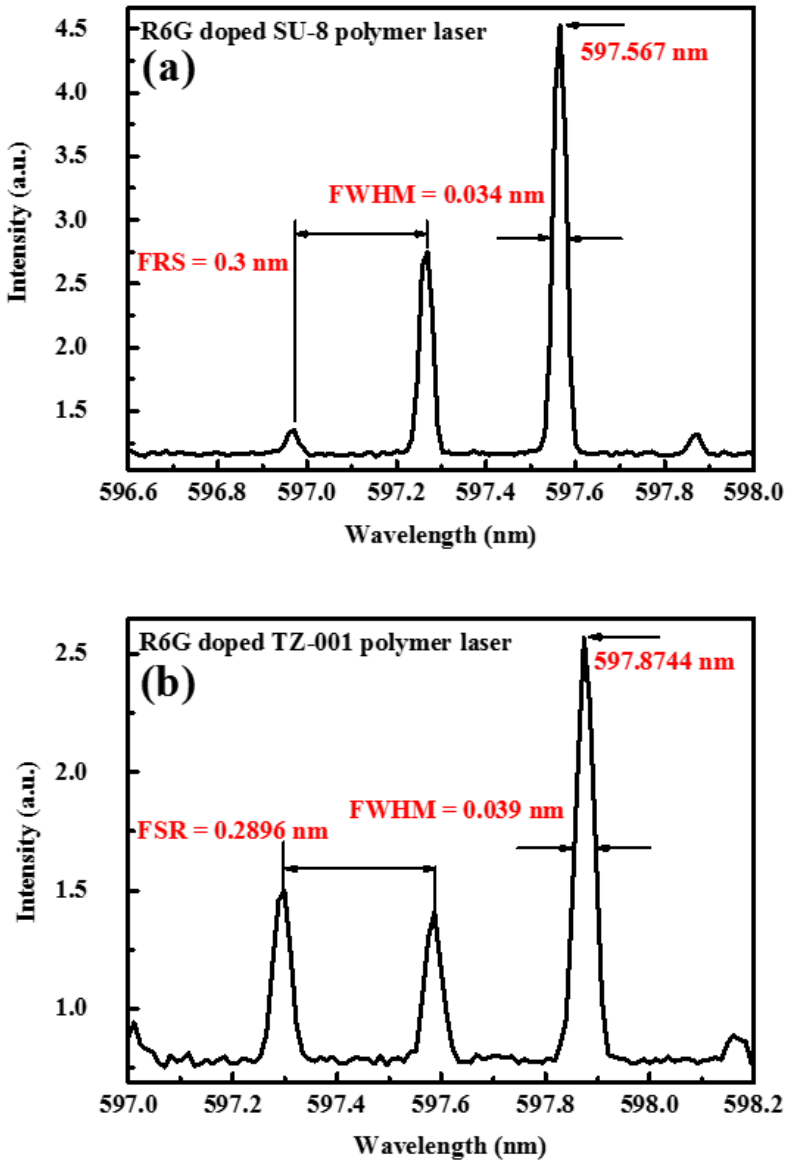

Figure 4.4: The lasing spectrum of (a) R6G-doped SU-8 polymeric microring laser and (b) R6G-doped TZ-001 polymeric microring laser.

spectral shift due to the TO and TE coefficient of cavity material based temper-

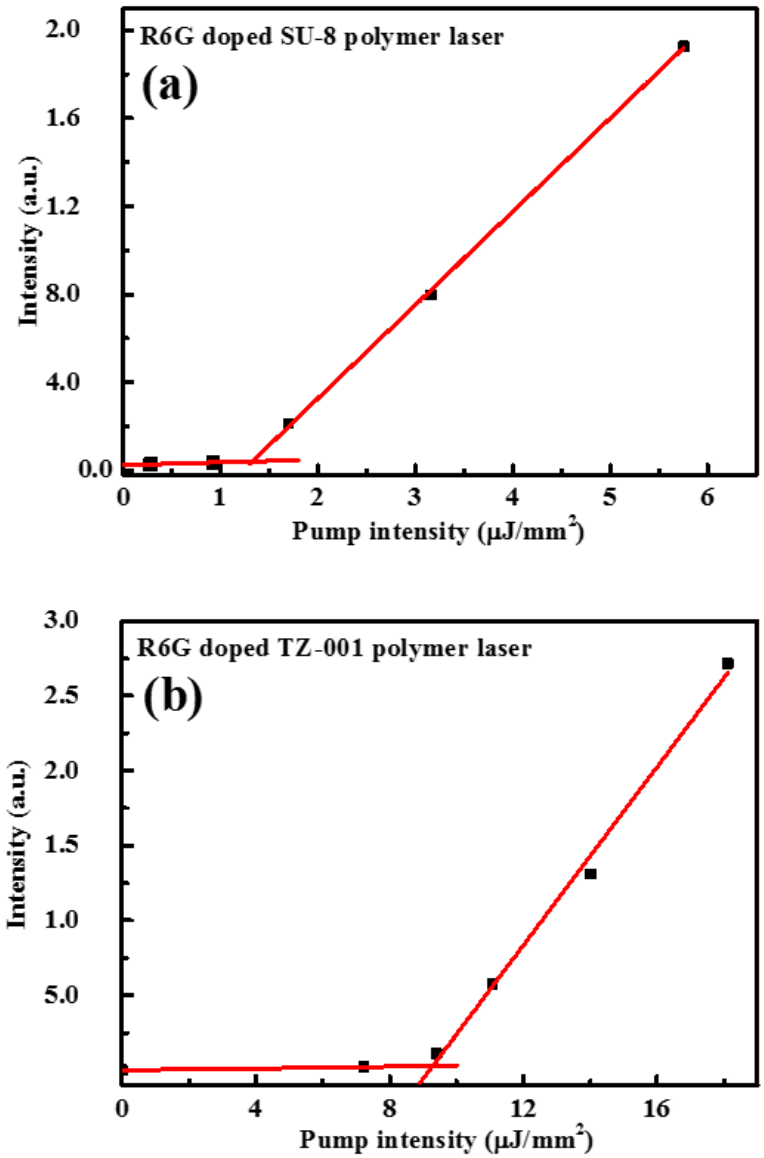

Figure 4.5: The lasing input-output characteristics of (a) R6G-doped SU-8 polymeric microring laser and (b) R6G-doped TZ-001 polymeric microring laser.

ature changing. The wavelength shift can be expressed by TO and TE as:

$$d\lambda = \lambda \left(\frac{1}{n_{eff}} M_{TO} + M_{TE} \right) dT \tag{4.1}$$

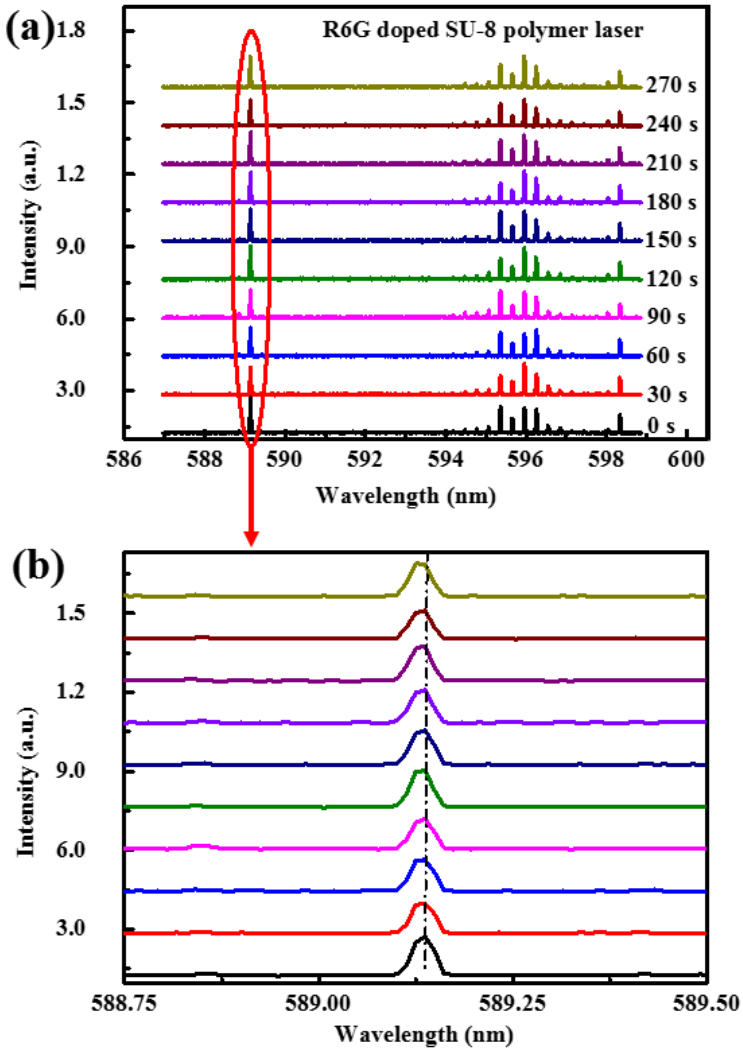

Figure 4.6: Lasing spectra of R6G-doped SU-8 polymer microring laser at different time intervals.

$$M_{TO} = \frac{dn_{eff}}{dT}$$

$$M_{TE} = \frac{1}{D}\frac{dD}{dT}$$

where D and n_{eff} denote the diameter and the effective RI of the polymeric microring cavity, respectively. T denotes the temperature. M_{TO} and M_{TE} denote TO and the TE coefficient of the cavity material, respectively. In the sensing

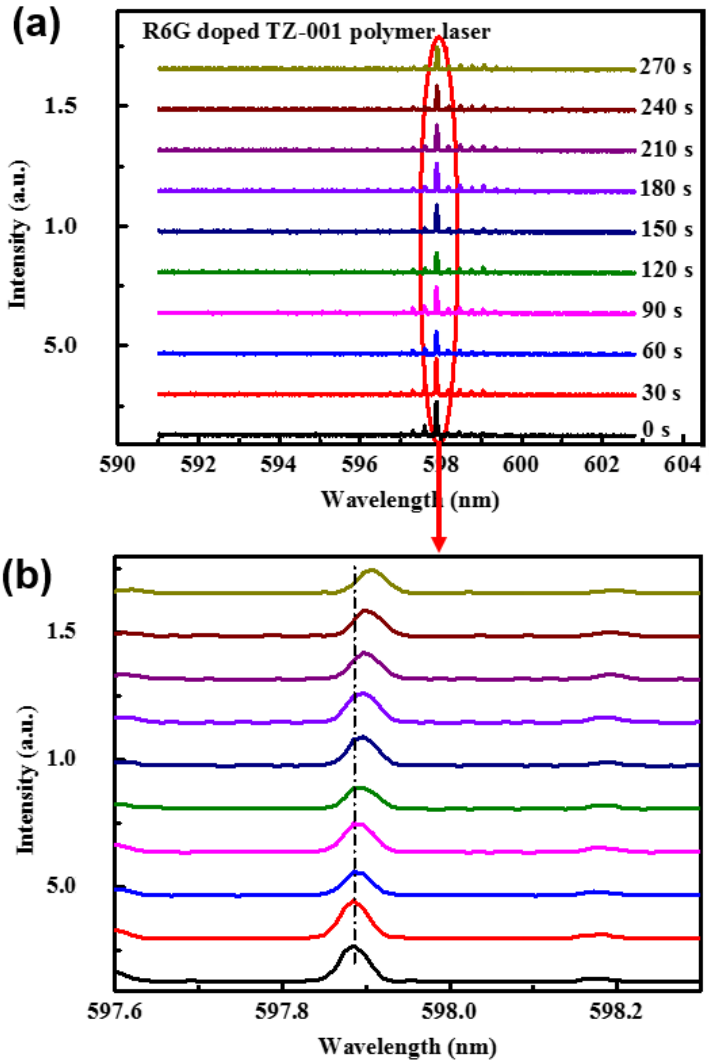

Figure 4.7: Lasing spectra of R6G-doped TZ-001 polymer microring laser at different time intervals.

experiment, we set the temperature range from 31 $^{\circ}C$ to 43 $^{\circ}C$ with hot plate, and this range can cover the physiological temperature range (35 $^{\circ}C$ to 42 $^{\circ}C$). The lasing peak shifted to left side about 0.92 nm when the temperature be set from 39 $^{\circ}C$ to 43 $^{\circ}C$. Since the TE coefficient of solid SU-8 ($\sim 10^{-6}$ K^{-1}) [126] is

far less than the TO coefficient, this blue shift was mainly contributed by negative TO coefficient.

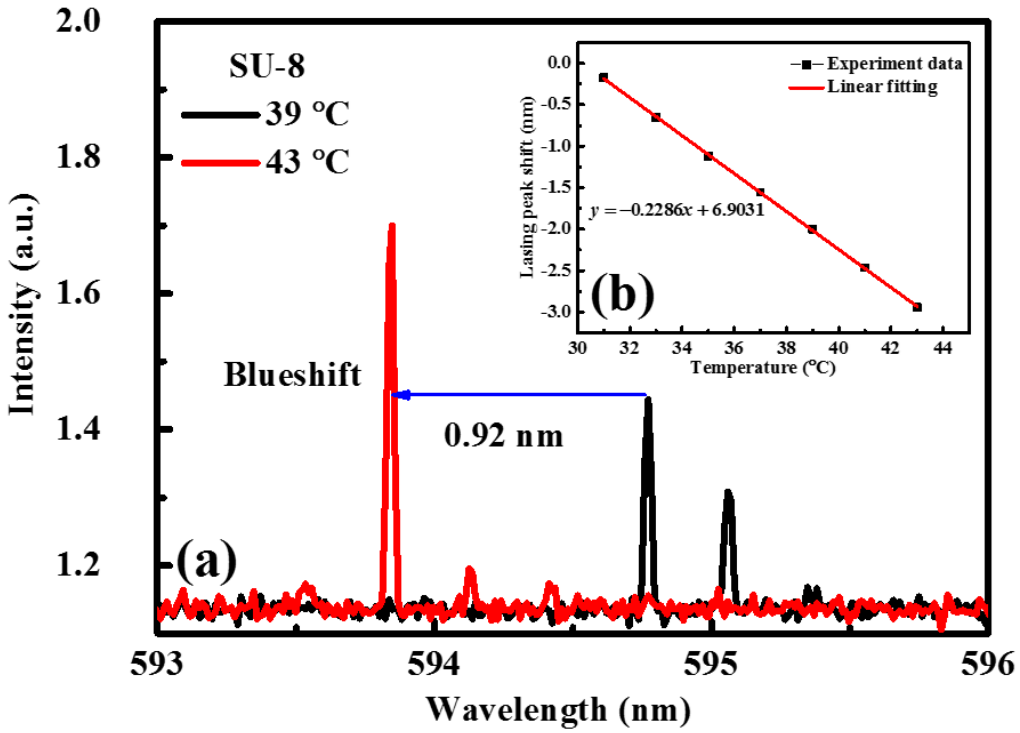

Figure 4.8: (a) The lasing spectrum of the R6G-doped SU-8 polymeric microring laser at 39 $°C$ and 43 $°C$. (b) The lasing peak shifts with variation of temperature.

As shown in figure 4.8 (b), a sensitivity of 0.2286 nm/$°C$ can be obtained by linearly fitting with the experimental results of the microring temperature sensor. By comparing with the microring based temperature sensor [114–116, 121] which mentioned in table 4.1, our work shows a obviously higher sensitivity without using any waveguide for coupling. We significantly improved the temperature sensitivity, because the WGM distribution was largely confined in the SU-8 polymeric microring core layer with the height of approximately 30 μm. In addition, our active microring temperature sensor shows a three times higher sensitivity and

twice narrow linewidth compared with the passive silicon microring temperature sensor contributed by Kim *et al.*, [114]. In theory, the resolution of our temperature sensor could be enhanced 6 times of the silicon based microcavity (i.e., $\sim$1.67 $\times 10^{-3}\ ^{\circ}C$). Although it shows a high temperature sensing resolution, the sensing limitation of our device was calculated to be only 0.13 $^{\circ}C$ due to the resolution limit of the spectrometer. All of the results above show that the SU-8 polymeric microring based temperature sensor has a very good performance.

On the other hand, as a unique merit, the chemical robustness of the fused silica microring host platform provides the feasibility of different matrix materials in same cavity. In order to achieve the WGM waveguiding, it is need to use a high RI material as the matrix material. For this reason, we used a polymer TZ-001 with the high RI of 1.78 as the matrix material to be the reference object. In addition, this work could be very helpful for exploring the properties of the novel hyperbranched polymer TZ-001, for example, the TO and TE coefficient of TZ-001.

With the same fabrication process in table 4.2, a TZ-001 polymeric microring was obtained. The lasing spectrum of the R6G doped TZ-001 polymeric microring laser is shown in figure 4.4 (b). Compared to the spectrum of SU-8, the TZ-001 microring shows a smaller FSR which is corresponding to high RI of TZ-001. According to this FSR, the radius of the TZ-001 polymeric microring was calculated to be 110.5 μm which is smaller than SU-8 ring, this is because the TZ-001 layer (0.5 μm) was thinner than SU-8 layer. The thinner TZ-001 layer was obtained by a higher spin speed in spin coating process which is operated to avoid the cracks.

Besides, the lasing threshold is shown in figure 4.5 (b) which is 9.28 μJ/mm^2, and it shows that the TZ-001 polymeric microring laser has a lower Q-factor compared to the SU-8 microring laser. This was mainly contributed by the larger

scattering loss which is resulting from the brittle TZ-001 matrix material. As shown in figure 4.7, the spectral stability of TZ-001 microring laser was detected at a pumping intensity of 140 μJ/mm^2 under different time intervals. It can be observed that the lasing peak shifted to right side about 0.02 nm in the time range of 0 $\sim$ 270 seconds. This was caused by deceasing of effective RI due to dye degradation under a large pumping intensity. Obviously, the SU-8 polymeric microring laser had better performance than TZ-001 polymeric microring laser.

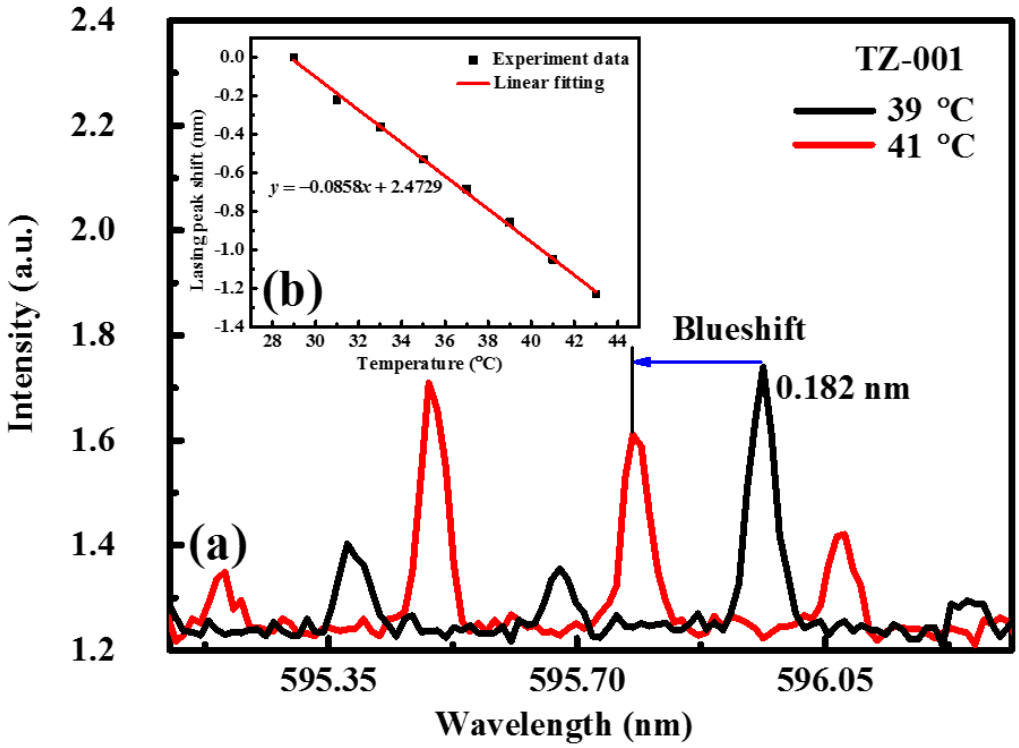

Figure 4.9: (a) The lasing spectrum of the R6G-doped TZ-001 polymeric microring laser at 39 $^{\circ}C$ and 41 $^{\circ}C$. (b) The lasing peak shifts with variation of temperature.

As shown in figure 4.9 (a), the lasing peak shifted to shorter wavelength about 0.182 nm with increasing the of temperature from 39 $^{\circ}C$ to 41 $^{\circ}C$. By linear fitting, the sensitivity of TZ-001 temperature sensor was calculated to about 0.0858

nm/$^{\circ}C$ which is shown in figure 4.9 (b). This sensitivity was about one-third of SU-8 microring, and the sensing resolution of TZ-001 microring was estimated to about 0.35 $^{\circ}C$. Herein, the low sensitivity due to the low TO coefficient of TZ-001 which is related to the physical property.

4.3. WGWM microdisk lasers for protein sensing

4.3.1 Experiments

The result of previous section demonstrated a high-sensitivity temperature sensor, and it proved that the TZ-001 based active polymeric microcavity laser can be applied for sensor. Based on this result, we can stat the development of a surrounding environment sensor based on ink-jet microdisks. Herein, we chosen protein as sensing object. In this experiment, the ink-jet printed microdisk was fabricated by 10 wt.% hyperbranched polymer FZ-001 (n = 1.45) which was used as the clad layer, 10 wt.% hyperbranched polymer TZ-001 (n = 1.78) doping with 5 mM Rhodamine590 which was used as waveguiding disk. The fabrication process is as same as figure 3.8, the etching process was not operated because a more robust structure is needed for sensor. In order to realize biosensing using an ink-jet printed microdisk, it is necessary to confirm the stability evaluation in the working environment of reaction between biomolecules or biomolecules. As we know, the reaction environment of the antigen-antibody reaction is water constituting 50 $\sim$ 60% of the human body. In the water environment, swelling, degradation of dyes and re-dissolution of dyes all may affect the stability of lasing spectrum, thus affecting the sensing performance. In order to confirm the stability, it is necessary to evaluate the spectrum of a underwater microdisk.

Here, figure 4.10 shows the setup to evaluate the spectrum of an underwater

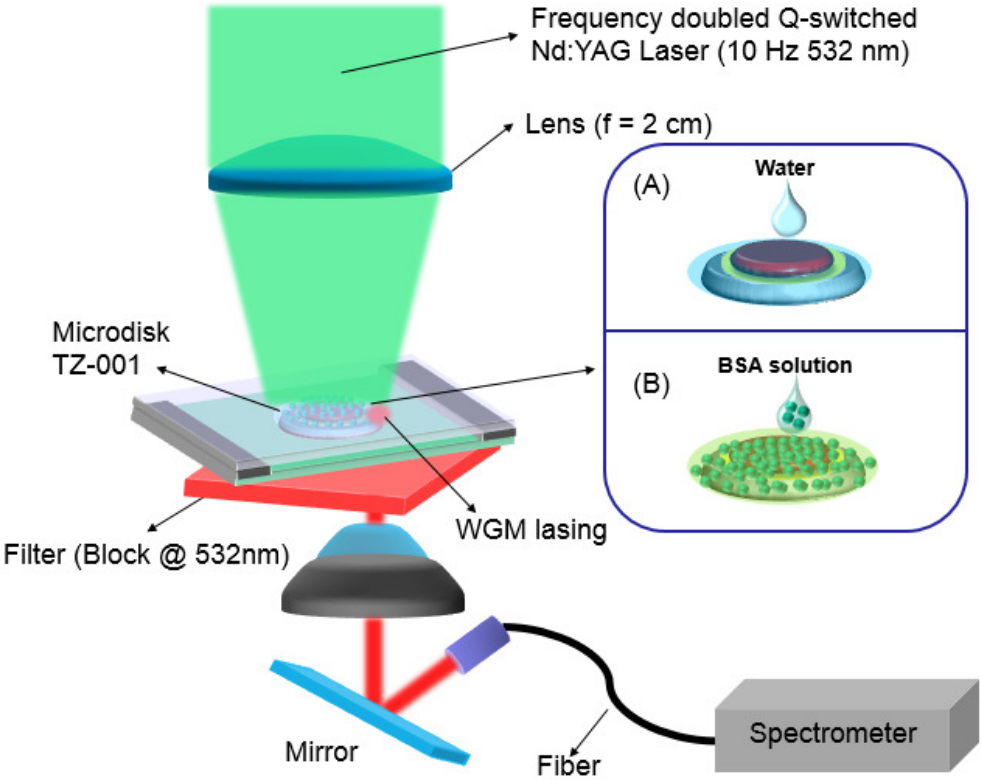

Figure 4.10: Setup of microdisks for protein adsorption sensing.

microdisk. A Q-switched YAG laser was used as a pumping light. The pulse pumping repetition rate was 10 Hz. As shown in the figure, the disk layer of microdisk is above the clad layer while the clad layer is on a PET substrate. In order to create the external environment of the liquid, a cover glass is covered above the substrate with enough space. When we start to evaluate the lasing spectrum in water, water is injected from the gap which is shown in the inset (A) of figure 4.10. By pumping the microdisk with Nd:YAG laser, the spectrometer observed WGM lasing spectra the water environment with integration of 300 shots in every 3min. The exposure time is 30 seconds, and the waiting time is 2 minutes 30 seconds. As the lasing spectrum is shown in figure 4.11, there is a spectral shift

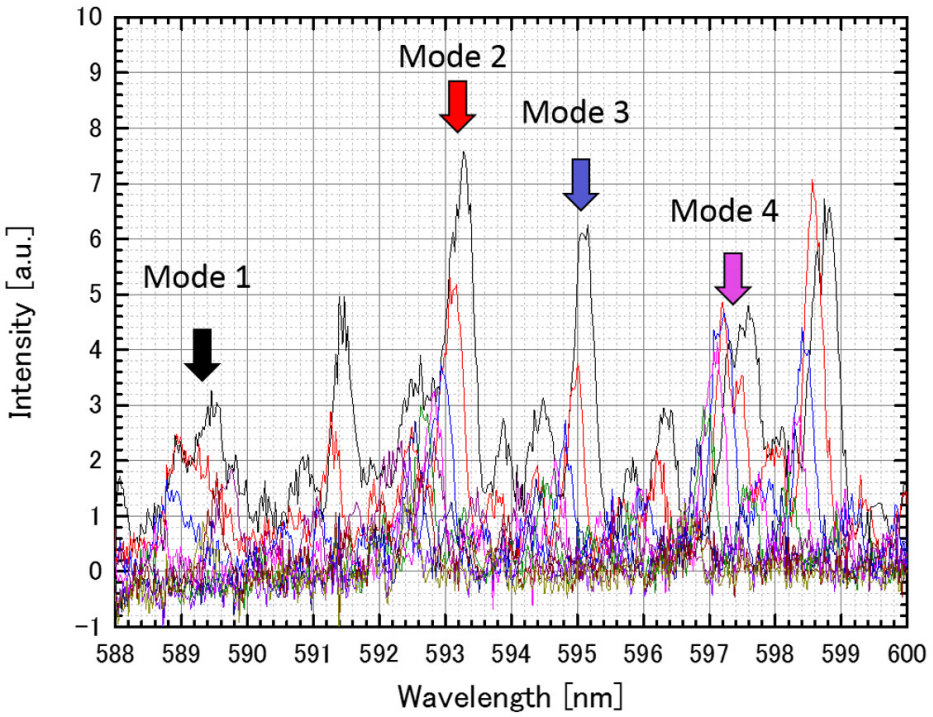

Figure 4.11: Lasing spectrum of a microdisk in water.

each pumping. To further analyze this migration, mode 1, mode 2, mode 3, and mode 4 are selected among all lasing modes. As shown in figure 4.11, there is a significant shift in every laser excitation. This shift is caused by dye degradation, the dye degradation come from the photobleaching by strong laser excitation. The degradation of dye leads to the decrease of effective RI in the microcavity, resulting in lasing spectral blue shift. Degradation rate α was around -0.033 was estimated from the figure 4.12. Actually, photobleaching is unavoidable if dyes are chosen as active WGM cavity gain material, hence the blue shift is also unavoidable. It is worth mentioning that we will discuss the solution for problem of photobleaching using quantum dots as gain materials in chapter 5. In fact, dye based WGM cavity can be still consider as good biosensor because it can be find that the shifts

are linear and not chaotic. When we use the dye based microdisk as sensor, we need to offset and take the shift line as baseline. Therefore, there is no problem in ink-jet printed disk sensing in water.

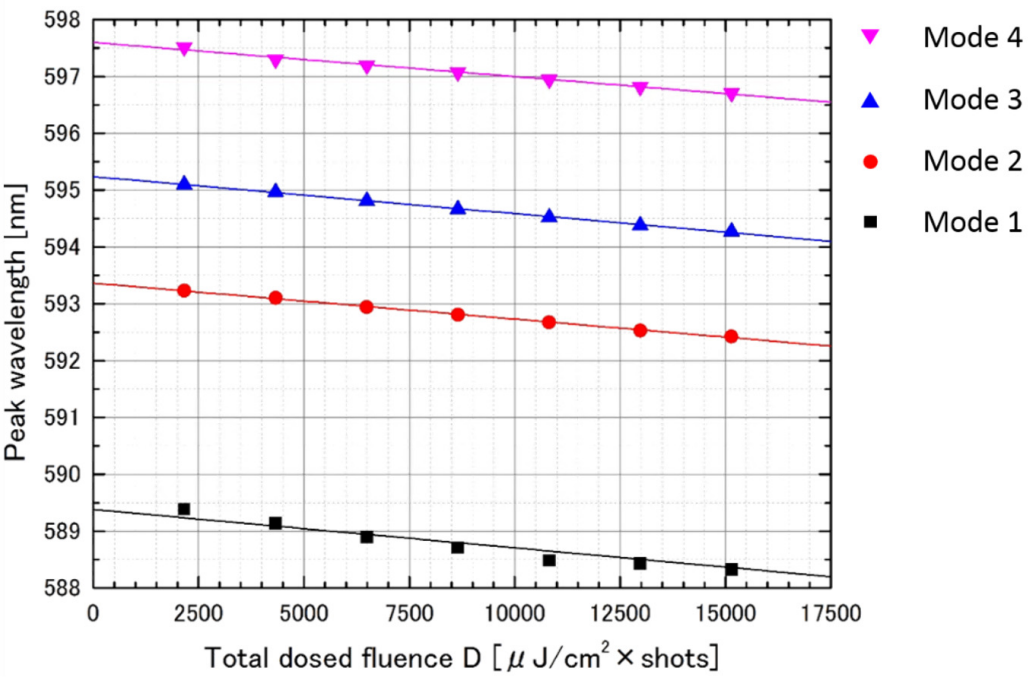

Figure 4.12: Lasing spectral shifts in water.

After investigating the stability of disk in water, it is necessary to investigate whether protein can adsorb on the surface of TZ-001. In order to facilitate observation, we chose a fluorescent BSA as adsorbent protein. At the same time, in order not to interfere with fluorescent protein, the blank disk without dye doping was used. The observation setup is shown in figure 4.13, the incident light enters an objective lens and is irradiated on the microdisk, and the fluorescence is collected by a camera after it comes out of the ocular. For recording fluorescent photographs, the exposure time and the image gain were set as 4 seconds and 6.4 times, respectively. In order to make fluorescent protein adsorbed on disk, mi-

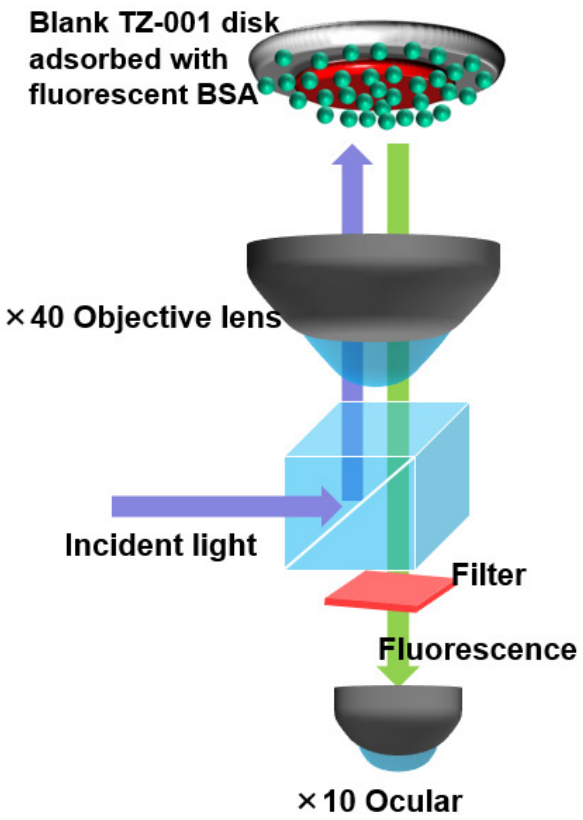

Figure 4.13: Observation setup.

crodisk was soaked in the fluorescent BSA with concentration of 1000 ppm. After soaking for five minutes, then dried the microdisk. The BSA adsorption state in 5 min is shown in figure 4.14. The figure shows that the disk in the TZ-001 area is obviously brighter the FZ-001 area after soaking for five minutes. The results show that BSA can be adsorbed on the surface of microdisk, and TZ-001 has a higher affinity than FZ-001 for BSA molecular.

To further investigate the BSA adsorption on microdisk, setup of figure 4.10 was used again. As it is shown in the inset of figure 4.10, the microdisk was first immersed in water, then inject the BSA solution, and rinse the disk with

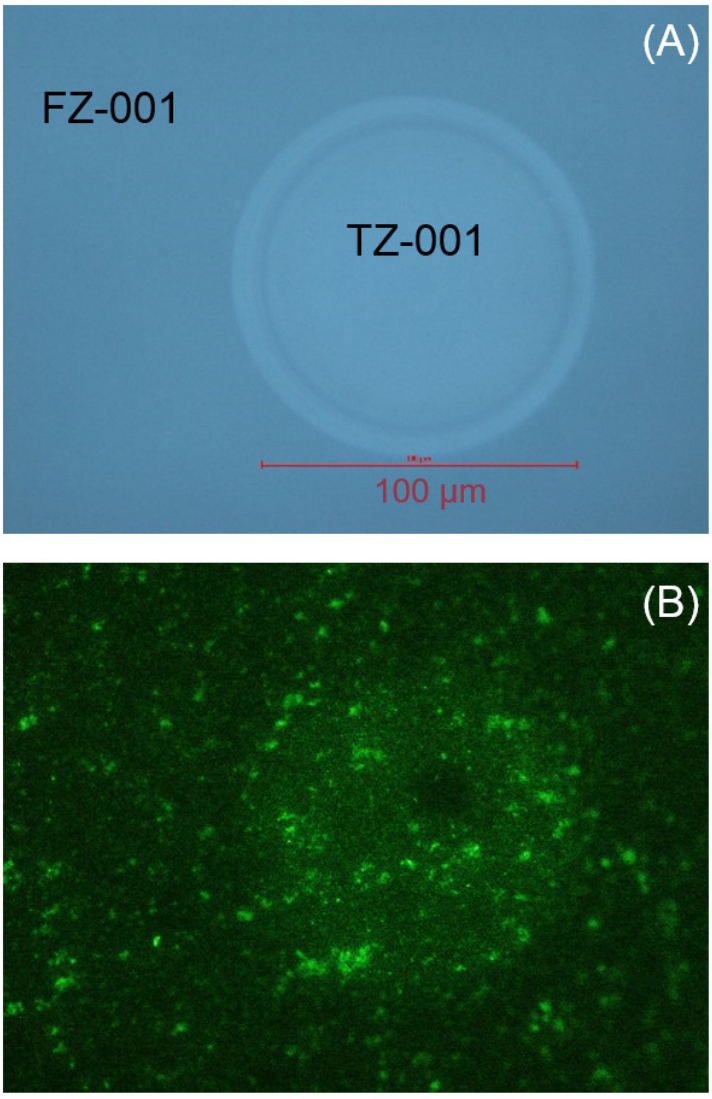

Figure 4.14: (A) A blank TZ-001 microdisk on FZ-001; (B) BSA adsorb state in 5 min after fluorescent BSA solution dropped in.

water lastly. We measured twice in water firstly, measured twice in BSA solution subsequently, and measured more three times in water again. The lasing spectrum of each measurement was showed as figure 4.15. Because of many modes and serious degradation of the dye, it is difficult to distinguish shift from the figure

Table 4.3: Experimental parameters of protein adsorption

Measure intervals	Exposure time	Light spot diameter	Pumping energy	Pumping repetition
3 min	30 sec.	300 μm	5.10 μJ	10 Hz

directly, so further data processing will be discussed in the next subsection.

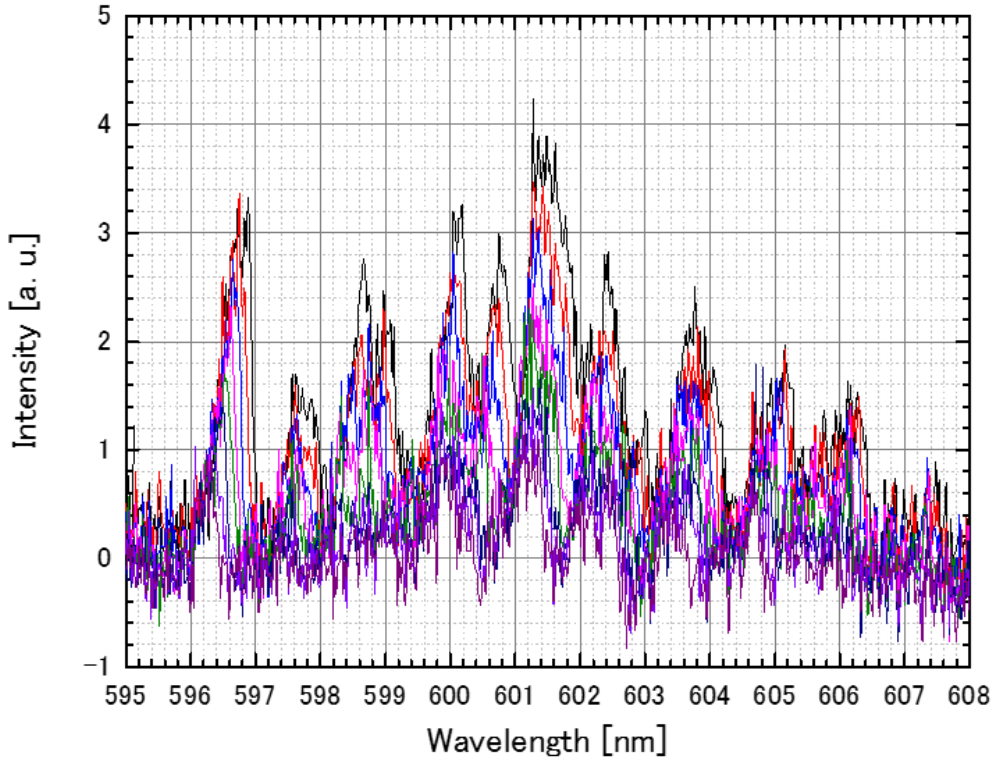

Figure 4.15: Lasing spectrum of BSA adsorption experiment.

4.3.2 Results and discussion

From the lasing spectrum of figure 4.15, we can get a wavelength shift as shown in figure 4.16. In the figure 4.16, the first 2 points (0∼5000 D)are in water

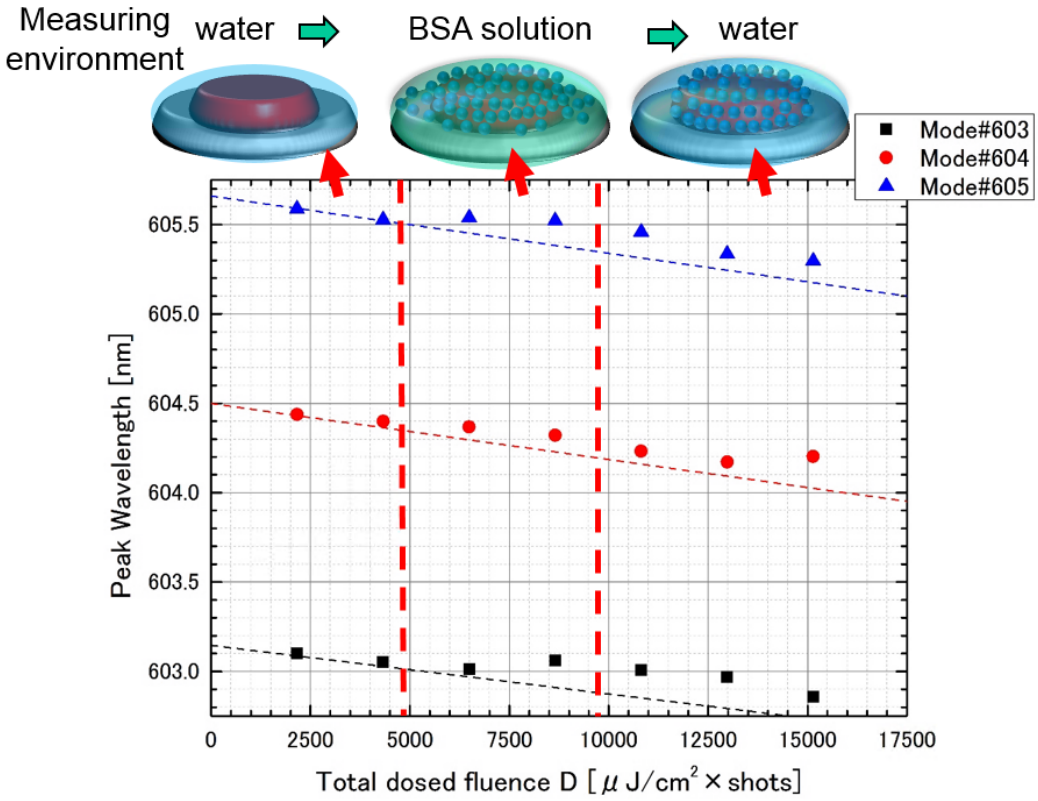

Figure 4.16: Investigation of spectrum shift on WGM caused by adsorption of BSA.Three areas between red dotted lines in the figure represent the wavelength changes of each state which is shown on the top of the figure.

environment, the following 2 points (5000∼1000 D) are in BSA environment, final 3 points (10000∼D) are in water environment. As we show, the wavelength shift will go back to the initial state with rinsing if the BSA molecular just lay on the disk not adsorption. In the experiment, we can observe that there is a redshift generation with the injecting of BSA solution. In addition, at the last three points, the redshift was still maintained when disk was rinsed with water. It fully proved that the BSA can be adsorbed on the TZ-001 microdisk. In order to better evaluate the amount of shift and analyze the adsorption of BSA, we established

the following equations for data fitting.

$$\lambda = \begin{cases} \alpha t + \lambda_m + \Delta\lambda \left(1 - e^{\frac{-(t-t_{ex})}{\tau}}\right) & (t \geq t_{ex}) \\ \alpha t + \lambda_m & (0 < t < t_{ex}) \end{cases} \tag{4.2}$$

Where t, t_{ex}, λ, λ_m, $\Delta\lambda$ and τ are reaction time, exchange water to BSA solution time, the peak wavelength, the offset of the peak wavelength of each WGM, total amplitude of the wavelength shift, and the time constant of the peak shift, respectively. A fitting example as figure 4.17. After studying the peak shift signals at different BSA concentration of 5∼20 mg/ml, respectively. All the peak shift amplitude $\Delta\lambda$ are assumed as ∼0.5 nm. All these experiments have

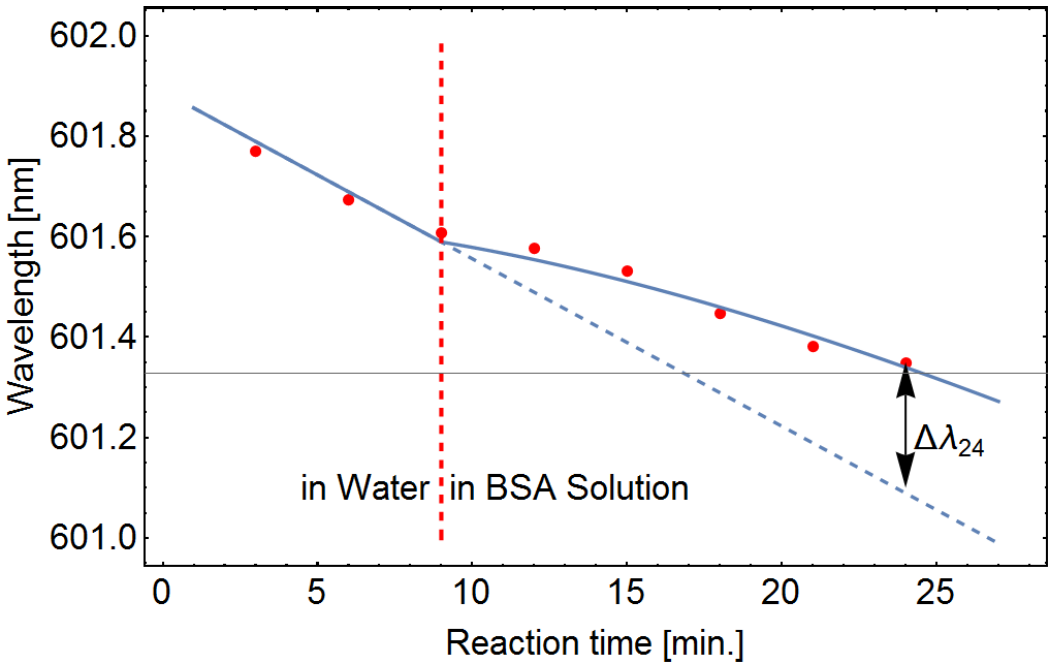

Figure 4.17: Example of fitting. $\Delta\lambda_{24}$ is the shift that reached saturation after 24 minutes.

fully verified the feasibility of protein sensing with ink-jet printed microdisks. However, in order to achieve a specific biosensor, it is necessary to prove that

the evanescent field of the resonator can sense the occurrence of specific binding. As the simulation shows in chapter 2, the evanescent field is usually nanometer scale, which means the thickness of adsorbed protein needs to reach nanometer the order, so that specific sensing can be realized. To investigate the thickness of protein adsorbed on our microdisk, a TZ-001 microdisk was soaked in a BSA solution with concentration of 100ppm. Phosphate buered saline (PBS) was used as buffer solution for BSA in this experiment. The sensing setup was as same as figure 4.10, and the experimental parameters was as same as table 4.3. Based on the above experimental results and fitting method, the result is shown in figure 4.18. The result shows that a shift of 0.11 nm can be obtained after 15 minutes saturation.

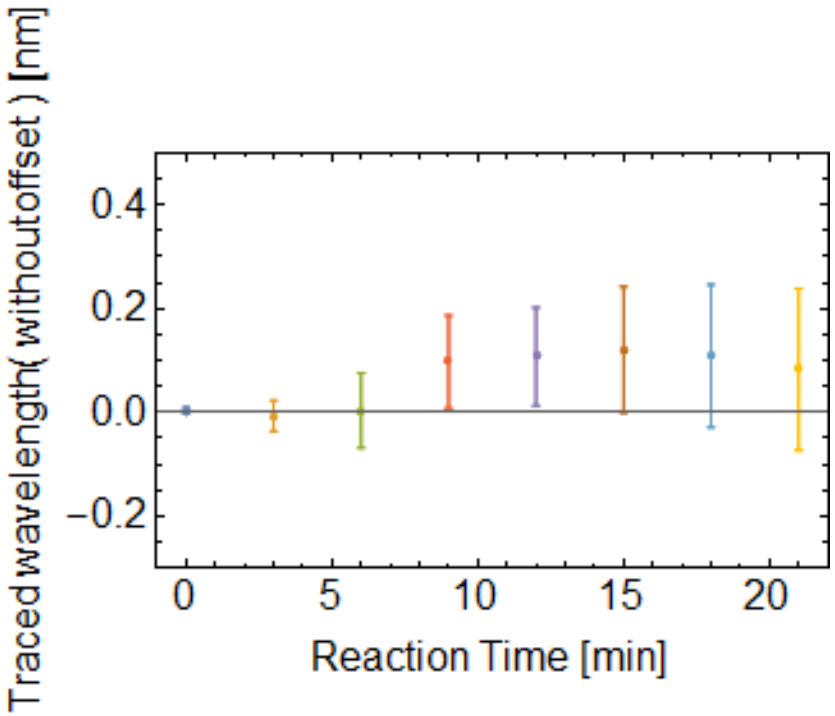

Figure 4.18: Time dependent shifts of microdisk in 100ppm BSA solution.

Using the FSR equation introduced in Chapter 2, the effective refractive index

of cavity can be expressed as

$$n_{eff} = \frac{\lambda^2}{2\pi R \Delta\lambda} \tag{4.3}$$

where $\Delta\lambda$ and λ are FSR and lasing wavelength, respectively. From the lasing spectrum of experimental sample in figure 4-9, $\Delta\lambda$ and λ are 0.8621 nm and 603.5813 nm, respectively. Hence $n_{eff} = 1.1715$. Substituting the value in the following equation,

$$2\pi R * n_{eff} = m\lambda \tag{4.4}$$

In this way, m can be obtained. On the other hand, the standing wave conditions of the microdisks in PBS and BSA:PBS solutions can be expressed as,

$$2\pi R * n_{eff1} = m\lambda_1 \qquad PBS \quad solution$$
$$2\pi R * n_{eff2} = m\lambda_2 \quad PBS : BSA \quad solution$$

Hence

$$\Delta n_{eff} = \frac{m\Delta\lambda_{shift}}{2\pi R}$$

Where $\Delta\lambda_{shift}$ is 0.11nm which obtained from the experiment. Therefore, we can know that the change of effective refractive index Δn_{eff} is about 0.0003. With the result of effective RI, the mode analysis was simulated by FEM based on the RF module of COMSOL. The thickness and the wedge angle of microdisk were set as 1 μm and 14° respectively for modelling the cross-section of microdisk. The simulation of mode distribution is shown in figure 4.19, effective refractive index can be calculated in this model.

As shown in figure 4.19, the effective index change of 0.0003 could be obtained when the BSA thickness on disk surface was set at 10∼15 nm. Here, the result shows that a ink-jet printed active microdisk successfully detected a BSA solution with concentration of 100 ppm, and the thickness of adsorbed BSA can be calculated.

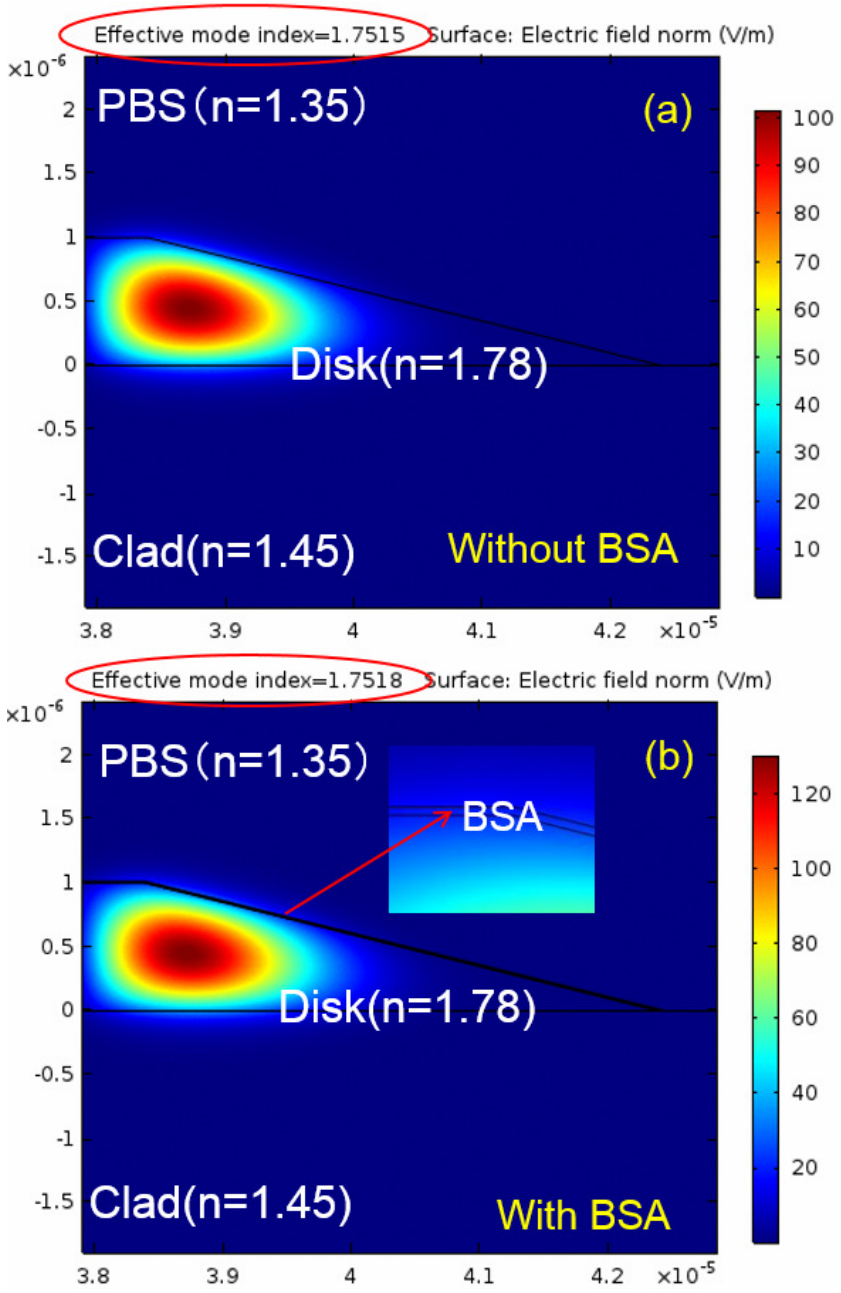

Figure 4.19: Fundamental mode distribution on microdisks edge (a) without BSA absorption, (b) with BSA absorption).

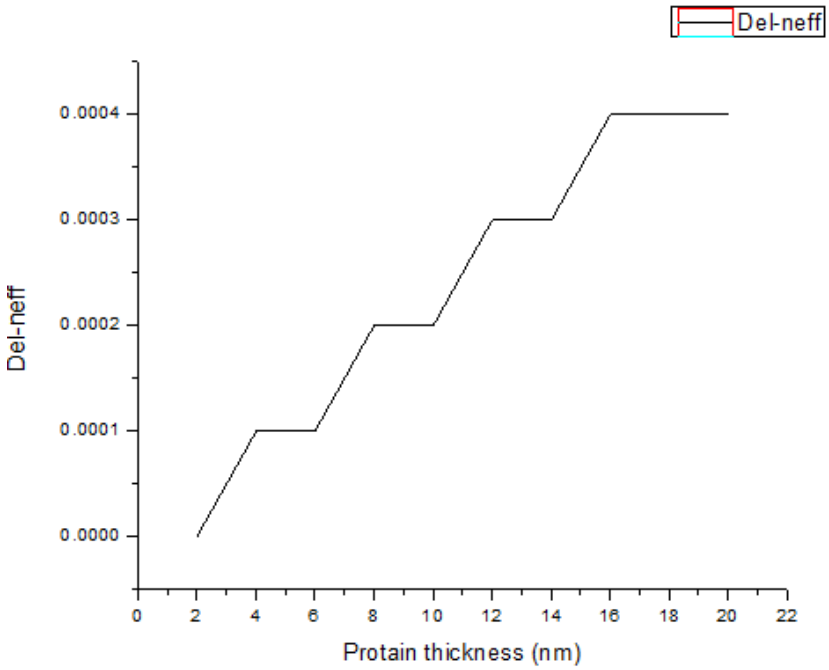

Figure 4.20: Simulation result of correlations between protein thickness and effective refractive index change.

Simulation result of correlations between protein thickness and effective refractive index change is shown in figure 4.20. It was known that the thickness of BSA adsorbed on microdisk was 10∼15 nm when sensing a 100 ppm BSA solution. This thickness is in the range of evanescent field which means ink-jet printed microdisk can be applied for a specific sensor.

4.4. Summary

In this chapter, a large edge angle WGM cavity for temperature sensing was demonstrated by a reconfigurable solid-state polymeric microring laser, and a small edge angle WGWM cavity for protein sensing was investigated with an ink-jet printed microdisk laser.

A temperature sensor with a high sensitivity of 228.6 pm/$^{\circ}C$ based on a R6G-doped SU-8 WGM microring laser was developed. As a test object, a TZ-001 WGM microring laser based temperature sensor was characterized with sensitivity of 85.8 pm/$^{\circ}C$. The temperature resolutions of SU-8 ring and TZ-001 ring were 0.13 $^{\circ}C$ and 0.35 $^{\circ}C$, respectively. The result provides feasibly of sensing devices based on active polymeric microcavity laser.

Based on the result of microring sensor, it was proved that the TZ-001 based active microcavity laser can be easily applied for sensor. As a WGWM microcavity, the ink-jet printed active microdisk successfully detected a BSA solution with concentration of 100 ppm. Based on the spectral shift of 0.11 nm, 10$\sim$15 nm thickness of absorbed BSA can be calculated. The investigation of water stability and the results above show that ink-jet printed microdisk has a high feasibility of high sensitive WGWM specific biosensors.

Although WGWM sensor have been realized, the photobleaching of dye still limits the performance of these two active WGWM cavities since short durability does not allow them to make real-time sensing. In the next chapter, we will discuss the use of quantum dots instead of dyes to improve the durability of cavity.

Chapter 5

Effects of gain intensity on spectroscopic behavior of WGWM in quantum dots doped microcavities

5.1. Introduction and purpose

In our previous work, it was found that there is always a blue shift in lasing spectrum of microdisks with the increasing of excitation power. Through experiments, we preliminarily analyzed that the blue shift mainly came from three reasons which are abnormal dispersion, dye degradation, and the change of WGWM spatial position. Among these reasons, the effect of gain on the spatial position of WGWM is less studied and most interesting. It will be possible to realize the controlling of the spatial position of WGWM if the effect of gain on the WGWM spatial position is proved. Since controlling the WGWM spatial position can help

to reveal more evanescent field, hence WGM spatial location can be controlled, more applications will be realized, especially the sensing applications. However, in order to fully prove that the blue shift is related to the effect of gain on the spatial position of WGM, the problems of abnormal dispersion and dye degradation must be solved first. The problem of abnormal dispersion can be solved by theoretical calculation, so the only problem is to solve the problem of dye degradation.

In Chapter 3 and Chapter 4, we discussed the effect of cavity edge angle on WGWM and the sensing applications with different cavities' edge angles, respectively. The both results give us confidence to further study the wet-process fabricated WGM microcavities. However, not only in the research of the effect of cavity edge angle on WGM, but also in the research of sensing applications with different cavities' edge angles, the degradation of dyes always limits the performance of active cavities. This limitation comes from two aspects. One is that the degradation of dyes causes lasing intensity to decrease or even not to emit laser light, thus directly shortening the durability of cavities. The other one is that the degradation of dyes causes shifting of lasing spectrum due to the decreasing of effective refractive index. While the durability of cavities effects the lifetime of sensing, and changing of effective RI effects the stability of sensing. On the other hand, we have found in previous experiments that excitation intensity has an effect on WGWM, so the degradation of dyes also limits our exploration of this problem. Therefore, if we want to make use of the advantages of active cavity and not be affected by the degradation of dyes, we must consider replacing dyes with other gain materials.

Generally, the degradation of dyes results from photobleaching. The photobleaching caused by fluorescent molecular permanently is unable to fluoresce due to the photon-induced chemical damage and covalent modification [128].When a fluorescent molecular transition from singlet state to triplet state, the irreversible

modifications of covalent bonds will happen. The exciton has a longer lifetime in the triplet state than in the singlet state relatively. Therefore, according to the optical properties of substances, some fluorophores emit a few photons and bleach quickly, while other fluorophores may go through many cycles and emit large quantities of photons.

Since quantum dots (QDs) have longer durability than typical organic dyes for photobleaching, it is a feasible strategy to choose quantum dots as gain material. Recently, the research on QDs microcavity lasers has become more and more attractive since Dang *et al* demonstrated red, green and blue lasing with single-exciton gain in the QDs films [129]. In the research of QDs laser behavior, the WGM microcavity structure combined with the gain medium of quantum dots is preferred because of the merits of tunable emission wavelengths, high quantum yield, simple fabrication, and solubility [130–133]. It can be summarized in four routes for fabricating the WGM QDs microcavity lasers.

The first route is a traditional method which is realized by an external cavity with a low-concentration QDs film as exterior coating. The lasing mechanism of this method is that the quantum dots coating is amplified into a WGM microcavity with high Q-factor by evanescent field. As the typical example of this method, Snee *et al* [130] and Min *et al* [131] demonstrated WGM lasing with Ds-coated microsphere and microtoroidal cavities, respectively. However, in order to achieve low threshold lasing, the morphology of WGM microcavity with high Q-factor is necessary, which undoubtedly increases the fabricating complexity of QDs laser.

The second route is based on the structure without external cavity, which is a novel method using high concentration quantum dot film as microcavity and internal gain. The main mechanism is the formation of self-assembled microcavities in quantum dot films under the action of external stress or strain. For example, Feber *et al* used ring trench as the base of microring laser, filled pure quantum dots

in the pretreated silicon template, coated with UV curable epoxy as clad layer, and peeled ring quantum dots from the silicon template as the core layer [132]. Sun *et al* demonstrated the self-assembled microcavity laser with the QDs based on the coffee-ring effect [134]. In addition, a on-chip QDs microplate laser was realized with water-dripping method which was presented by Chen *et al* [135]. This simple fabrication process provides the variability and diversity for QDs based WGM microcavity lasers. Therefore, more preparation methods and microcavity structures are expected to promote the exploration and research of on-chip QDs microcavity lasers.

The third route is based on external quasi-cavity configuration, which is an assembled method driven by the patterned quasi-cavity as the cladding layer consisting of the QDs microcavity laser. As the main mechanism of this route, the conformal adhesion of quantum dots formed the core layer along the patterned cavity substrate. For example, Kiraz *et al* presented a WGM optofluidic laser which consist of silica micro capillary as the clad layer and self-assembled QDs film as the core layer [136]. However, the on-chip integrated QDs microcavity laser is uniquely concerned, especially in terms of the optoelectronic devices.

The fourth route is to mix the gain material and matrix material to realize hybrid cavity by wet process. For example, Sun *et al* used high concentration quantum dot/polymethyl methacrylate (QD/PMMA) nanocomposites based on polymer stability and evaporation droplets of colloidal quantum dots to realized WGM QDs microbubble laser [133]. Compared with the third route, this route requires matrix materials such as polymers to form cavities, rather than self-assembly of QDs to form cavities. Although the condensation of QDs can be a challenge to this route, the stable cavity attracts many researchers to study with it for long-term sensing.

In this chapter, the third route was realized with an on-chip QDs microring

laser by virtue of the annular groove etched in the fused-silica substrate, the fourth route was demonstrated by an ink-jet printed QDs doped polymeric microdisk. In our experiments, both QDs microrings and QDs microdisks were achieved long-durability laser. In a QDs microdisk, the lasing spectrum still shifted with the increasing of excitation intensity although there is no effects of dye degradation. Finally, we have successfully demonstrated by numerical simulation that when the WGWM is unbalanced in the sidewall loss, WGWM spatial position moves to the inside of the cavity with the increase of the gain. (Two partial contents of this chapter have been published at SPIE [57] and Optics Letters [59], respectively.)

5.2. Anomalous dispersion of refractive index in microdisk lasers

5.2.1 Experiments

As mentioned in section 5.1, we have found that the WGWM lasing spectrum always has a blue shift with the increasing of excitation power. To verify whether this blue shift originated from abnormal dispersion or other causes, the following experiments were performed. Two different microdisks (DiskA and DiskB) were fabricated with ink-jet method (show in figure 3.1) by 10 wt.% and 5 wt.% TZ-001, respectively. It is note that the edge angle of these two disks are different with disks in chapter 3 although the concentration of inks are same. This is because the parameters of ink-jet fabrication are different between this two times. In this experiment, the angle of diskA is larger than that of diskB. Next, the pumping setup was as same as figure 3.3. The pumping wavelength, integration time and repeat rate were 532 nm, 10 s and 50 Hz, respectively. The ND filter was used to adjust excitation power. In order to monitor the lasing wavelength

shift, we set the following 3 steps experiment. Step 1 was set as decreasing step of excitation power (40.9 μJ/mm^2 $\sim$ 10.2 μJ/mm^2), Step 2 was set as increasing step of excitation power (10.2 μJ/mm^2 $\sim$ 40.9 μJ/mm^2), and finally Step 3 was set as decreasing step of excitation power (40.9 μJ/mm^2 $\sim$ 10.2 μJ/mm^2). The lasing spectrum was recorded every 10.2 μJ/mm^2.

As shown in figure 5.1, both DiskA(a) and DiskB(b) show a same shift tendency with excitation power changes of the 3 step. With decrease of excitation power, the lasing peaks shift to red side of spectrum in step1. Meanwhile, with increase of excitation power, the lasing peaks shift to blue side of spectrum in step2. Finally, with decrease of excitation power, the lasing peaks shift to blue side of spectrum in step3. These 3 steps shifts proved that the shifts are not only caused by dye degradation because dye degradation only causes red shift. In addition, DiskB always had a larger shift than DiskA by analyzing figure 5.1 (a) and figure 5.1 (b).

The peak shift rate $\Delta\lambda_{sum}$ of DiskA in step1, step2, step3 were calculated as -1.71$\times10^{-3}$ nm/(μJ$\cdot$mm^{-2}), -5.37$\times10^{-3}$ nm/(μJ$\cdot$mm^{-2}), -2.10$\times10^{-3}$ nm/(μJ$\cdot$mm^{-2}). The peak shift rate of DiskB in step1, step2, step3 were calculated as -1.81$\times10^{-3}$ nm/(μJ$\cdot$mm^{-2}), -6.35$\times10^{-3}$ nm/(μJ$\cdot$mm^{-2}), -2.20$\times10^{-3}$ nm/(μJ$\cdot$mm^{-2}). We assumed that there are two main reasons cause peak shift $\Delta\lambda_{sum}$, one is $\Delta\lambda_{sum}$ the spectral shift $\Delta\lambda_{Rd}$ caused by dye degradation and the other is the peak shift $\Delta\lambda_p(I)$ caused by variation of excitation power. The correlations are expressed as,

$$\Delta\lambda_{sum} = \Delta\lambda_{Rd} + \Delta\lambda_p F_p \tag{5.1}$$

Where F_p is the excitation power and $\Delta\lambda_p$ is coefficient of spectrum shift. As shown in figure 5.2, the spectral shift rate of DiskA and DiskB were slightly different, and they were estimated as -3.77$\times10^{-3}$ nm/(μJ$\cdot$mm^{-2}) and -4.21$\times10^{-3}$ nm/(μJ$\cdot$mm^{-2}), respectively. The total shift of DiskA and DiskB were -1.54$\times10^{-1}$

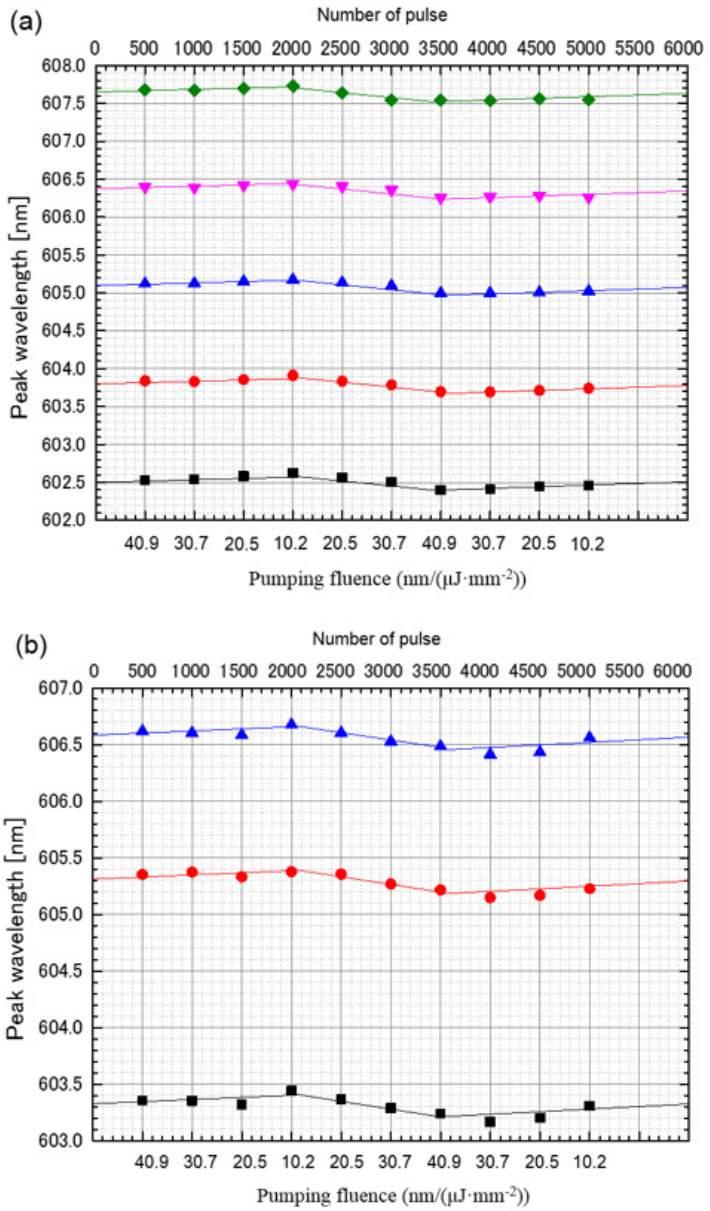

Figure 5.1: (a) Lasing peak shifts of 10 wt.% Tz-001 5mM Rhodamine590 doped microdisks; (b) Lasing peak shifts of 5 wt.% Tz-001 2.5mM Rhodamine590 doped microdisks

nm and -1.72×10^{-1} nm, respectively.

5.2.2 Results and discussion

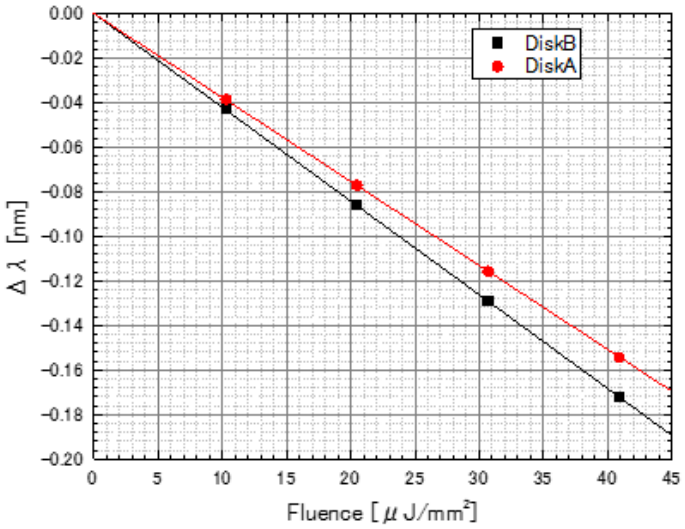

Figure 5.2: The spectrum shifts characteristics of DiskA and DiskB by excitation power changing.

Figure 5.2 shows the pure spectral shift (deduct the effect of dye degradation) of DiskA and DiskB with the variation of excitation power.

As mentioned earlier, the RI variation of anomalous dispersion caused by the dye dopant could be a reason for affecting the lasing wavelength λ. To confirm the effects by anomalous dispersion, we calculated the theoretical dispersion of RI at 600 nm with simple Kramers-Kronig relation. The correlation between the absorption/emission cross-sections $\sigma_{a,e}(\omega)$ and RI dispersion $\Delta n_{a,e}(\omega)$ is expressed as,

$$\sigma_{a,e}(\omega) = \sum \eta_i (s_i/2)/((\grave{u} - \omega_i)^2 + s_i^2/4) \tag{5.2}$$

$$\Delta n_{a,e}(\omega) = \frac{-N}{2k} \sum \eta_i (\omega - \omega_i)/((\omega - \omega_i)^2 + s_i^2/4) \tag{5.3}$$

where N denotes spatial density of excited molecules, k denotes the propagation

coefficient, and ω denotes the angular frequency of light. For Lorentz fitting, we take fitting parameters of η_i, s_i and ω_i into account. Herein, σ_a can be measured by experiment, σ_e were numerically fitted by using η_i, s_i and ω_i. Based on these data, the total $\Delta n(\lambda)$ was approximated by using $\Delta n_a(N - N^*)/N + \Delta n_e N^*/N$. Herein, with the corresponding to 1 % of the N, a spatial density of excited molecules N^* was assumed 310^{17} cm^{-3} since the Rhodamine 590 was doped in a very high concentration. As the calculation result From the figure 5.3, the maximum of refractive index shift was approximated about 0.012 %. Hence, the equation of WGM peak shift $\Delta\lambda$ is given by

$$\Delta\lambda = \frac{2\pi nd}{m} \tag{5.4}$$

where n, d, and m denote the RI, the diameter of WGWM cavity and mode number, respectively. With the above equation, the peak shift caused by anomalous dispersion can be calculated as -0.82×10^{-1} nm. On the other hand, the number of -1.54×10^{-1} nm, -1.72×10^{-1} nm about diskA and diskB is not matched under same condition of excited molecules density N^*. The result shows that the blue shift caused by abnormal dispersion is very small. Hence, there are other reasons causes the large blue shift. Here, we assume that larger optical gain can affect the WGWM field to slightly move insider radially with the increase of excitation power. To prove this assumption, a cavity without dye degradation and a WGWM simulation are required.

5.3. QDs microring lasers in an annular groove

5.3.1 Experiments

QDs microring lasers are designed and characterized on a fused-silica ring groove platform with stable chemical and physical properties. This method pro-

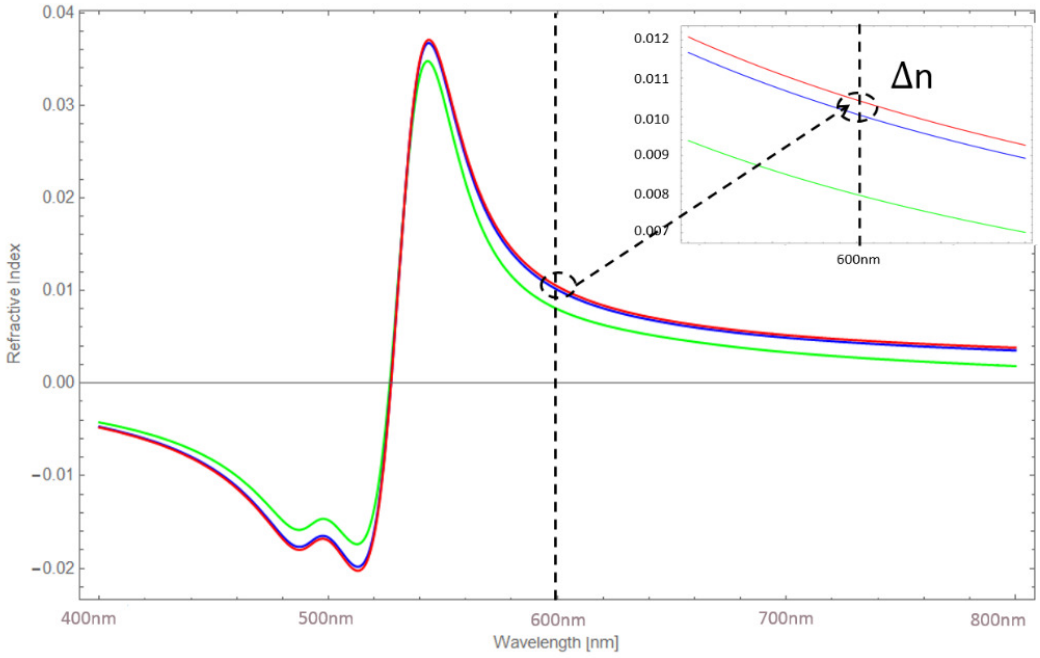

Figure 5.3: The variation of refractive index changing by anomalous dispersion.

vides the possibility of realizing different emission reconfigurable gain material in chip size order microcavities. This flexible method show potential in sensing applications by using the on-chip QDs microcavity laser with the laser behavior in different environments.

In the experiment, two kinds of QDs lasers were fabricated by coating with a cured pure colloidal CdSe/ZnS core-shell QDs and polystyrene-doped QDs film as a core layer. Herein, PS was chosen as the dopant because it has a relatively higher RI than ordinary polymers and it has a common solvent with the selected quantum dots that can be perfectly mixed. To fabricate the pure QDs microcavity laser, QDs toluene solution with the concentration of 30 mg/mL was spin coated on the microring groove platform under a low rotation speed (600 rpm), and dried under 130 $^{\circ}C$ for 15 min. The refractive index of dried QDs film was about 2.45 [137]. To

fabricated the QDs PS microcavity laser, 3 wt.% PS solution was mixed with pure quantum dots solution at volume ratio of 1 to 9, and the solution was spin coated on the microring platform. The SEM image of the microring groove platform without coating was shown in figure 5.4(a). The detailed fabrication was discussed in chapter 2. In this work, the fabrication processes can be shown in figure 5.4(b)-(d). The top and cross-section views are shown in figure 4.1. Here, the width and height of this annular groove were 40 μm and 30 μm, respectively. The diameter of the inner disk was 160 μm.

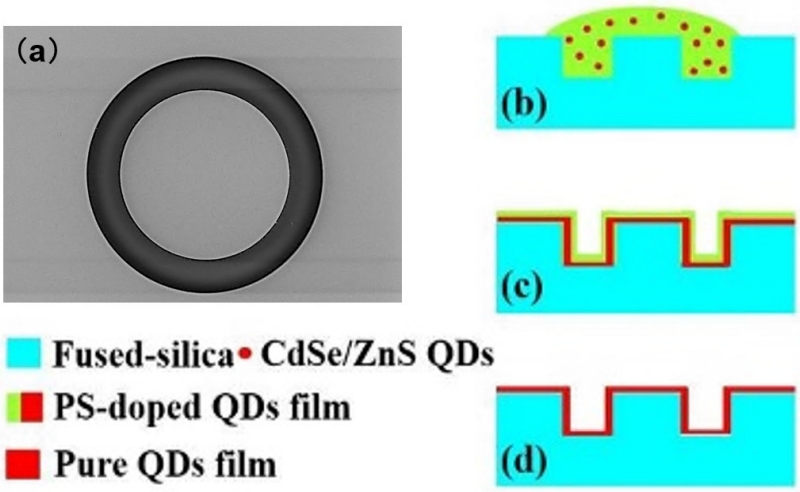

Figure 5.4: (a) SEM image of a microring groove platform without coating. (b)-(d) Cross-section views of a PS-doped QDs in the process of (b) dripping, (c) spin-coating; (d) pure QDs cured on the microring groove platform.

As mentioned in foregoing chapters, we used a microscope based setup system for pumping and collecting lasing signal from a QDs microcavity laser which was shown in figure 5.5. A Nd:YAG pulsed laser with wavelength of 532 nm (PNG-002025-040, Nanolase Corp.) was used as pumping source. The pulse duration was set as 0.5 ns, and repetition rate was set as 10 Hz. A planoconvex lens

(focal length: 20 mm) was used to focused the pumping light spot within 300-μm-diameter on the QDs microcavity laser. With the object lens of microscope (Eclipse TE2000-U, Nikon), the laser signal of QDs microcavity was collected by a multimode fiber with the diameter of 200 μm (Thorlabs, FP600ERT). Prior to the measurement, the multimode fiber was properly positioned to reduce the PL background on the lasing signal. Finally, the lasing signal was collected by a spectrometer with the grating of 1200 l/mm, and the integration time was set as 1 s. In order to observe the spectral changes in different external environments, the QDs laser are placed in a transparent vessel.

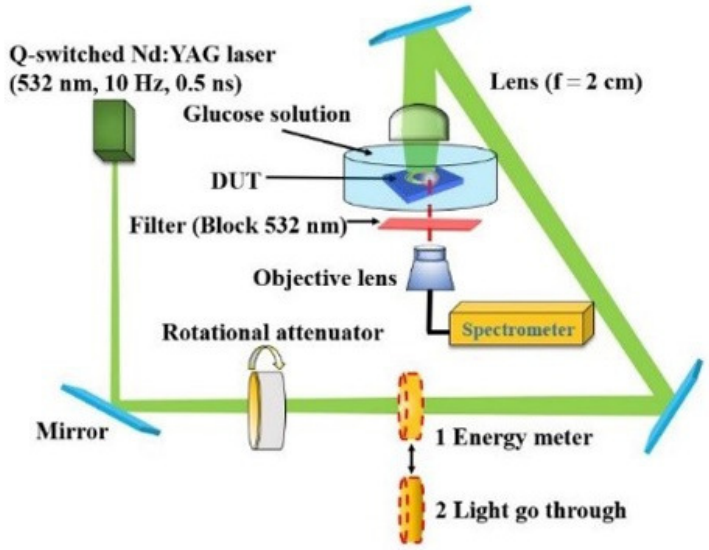

Figure 5.5: The microscope based measurement setup for pumping and detecting on-chip QDs microcavity laser.

5.3.2 Results and discussion

By using the microscope based measurement setup system, the lasing spectrum of QDs microcavity laser can be obtained. S lasing spectrum of a pure QDs

microcavity laser under the pumping intensity of 16 μJ/mm^2 was shown in figure 5.6 (a). A lasing threshold of 8 μJ/mm^2 could be estimated by integrating the intensities of lasing spectrum from 636 nm to 640 nm under different pumping power which was shown in figure 5.7 (a). Obviously, mode overlaps caused the lasing peak broadening can be observed in the lasing spectrum (figure 5.6 (a)). The scattering from rough sidewalls and the undesired scattering from cracks of QDs film caused the appearances of some random lasing modes which lead to difficulty of lasing peak observation [138].

On the other hand, figure 5.6 (b) shows the lasing spectra of QDs PS laser under the pumping power of 34 μJ/mm^2. A FWHM of 0.12 nm can be obtained from the lasing spectrum at peak wavelength of 626.15 nm. By using the Q-factor equation which was mentioned in chapter 2($Q = \lambda/\Delta\lambda$ [125]), a Q-factor of 5218 can be calculated. Compared to the previous works, the Q-factor of our QDs PS microring laser is twice higher than the work presented by by Sun *et al* citeMicrobubble,Unraveling, 4 times higher than the work of QDs micropalte presented by by Chen *et al* [135]. In addition, a lasing threshold of 13.45 μJ/mm^2 could be obtained from intensities of lasing peak around 626.15 nm under the different pumping power which was shown in figure 5.7 (b). Compared with the threshold of pure QDs laser, the threshold of QDs PS lasers was decreased due to the decrease of quantum dot concentration caused by adding PS. Compared to the pure QDs laser, QDs PS laser showed a more easily identifiable lasing spectrum. It means that the smoother surface of the cavity and fewer cracks resulted in less random lasers due to excessive scattering by adding the polymer of PS. Actually, this improvement is valuable of sensing applications since a easy identifiable lasing peak can be conducive to tracking of spectral shifts.

In order to investigate the photostability of the QDs microcavity laser, both pure QDs laser and QDs PS laser were characterized under long-term pumping.

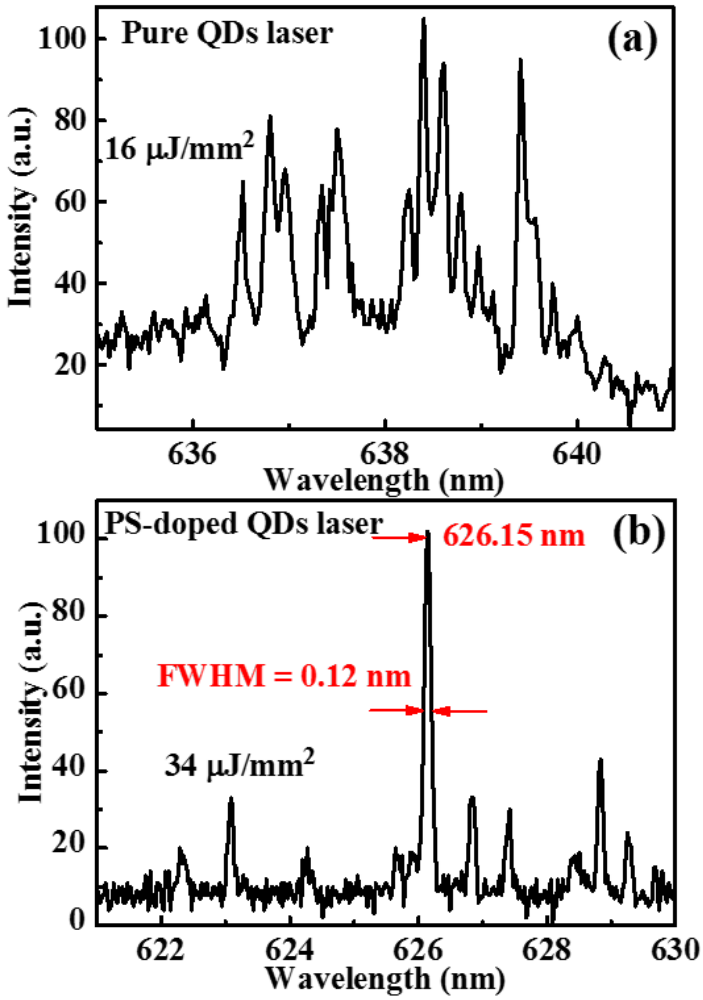

Figure 5.6: (a) The lasing spectrum of pure QDs microcavity laser; (b) The lasing spectrum of QDs PS microcavity laser

The durability of QDs PS microcavity laser and Rhodamine 590 doped TZ-001 microcavity at the uninterrupted pulse pumping in air. We use TZ-001 instead of PS, because the Rhodamine 590 doped PS cavity can not lasing. It is noteworthy that, as our previous work has demonstrated the reconfigurability of the external microring platform, the dye doped microcavity laser was fabricated from

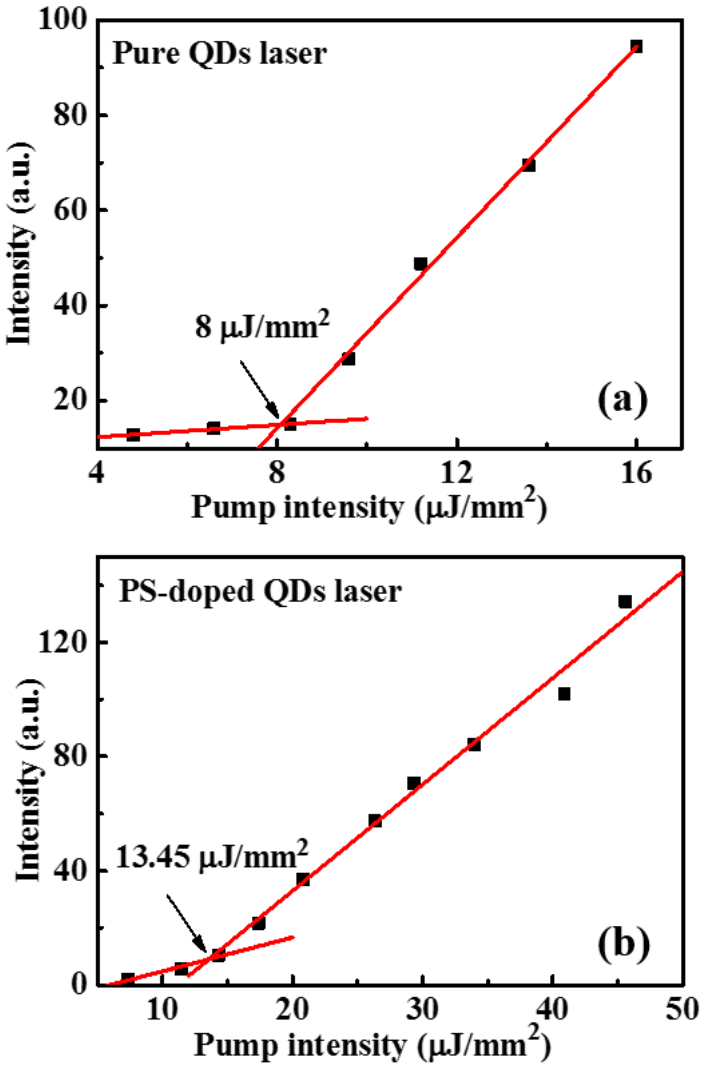

Figure 5.7: The input-output characteristics of (a) the pure QDs and (b) PS-doped QDs microcavity lasers.

the microring groove [55]. Here, we evaluated the optical stability of the cavity laser by two indicators, one is the intensity of the emitted light, and the other is the wavelength of the laser peak. As shown in 5.8 (a), under the pumping power of μJ/mm^2, the laser emission of PS-doped QDs laser remained stable for more

than 15 minutes which showed a very good photostability. On the contrary, the dye doped laser decayed quickly to no excitation in 2 minutes under the pumping power of 7.78 μJ/mm^2 due to dye degradation. The reason is that the durability of dye doped lasers is very short due to the breakage of chemical bonds caused by dye degradation under the action of light, while high quantum efficiency make the quantum dot lasers have a long durability.

In order to observe the stability of the spectrum, the laser peaks of PS doped QDs laser at 0 minutes and 15 minutes are shown in figure 5.8 (b). The position of the laser peaks did not shift obviously, which indicates that the spectrum of PS doped QDs laser is very stable in air. On the other hand, as mentioned in the previous chapter, the laser peaks of dye doped laser always blue shifts because of the dye degradation. Many sensing applications are in water environment, so it is necessary to investigate the photostability of QDs lasers in water. As shown in figure 5.9 (a), the intensity of light emitted is not as stable as in the air, but shows certain fluctuations when the QDs microcavity laser was in aqueous environment. In order to make the measurement accurate, the measurement take once every five minutes, and take the average value of the measurements three times each time under the pumping power of 28.3 μJ/mm^2. In fact, after observing many spectra, we can know that the fluctuation of intensity is mainly due to the disappearance and appearance of some laser modes. This disappearance and appearance of laser modes indicated the dynamic evolution of QDs cavity lasing behavior in aqueous environment, mainly due to cracks in quantum dot films. The ruptured quantum dots film gradually absorbed water molecules, thus adjusting the effective RI. Furthermore, a significant blueshift can be observed by comparing the laser peaks of PS doped QDs laser at 0 minutes and 40 minutes which are shown in figure 5.9 (b). It showed unstable spectrum in aqueous environment.

To further explore the spectral stability of the QDs laser in water, the evo-

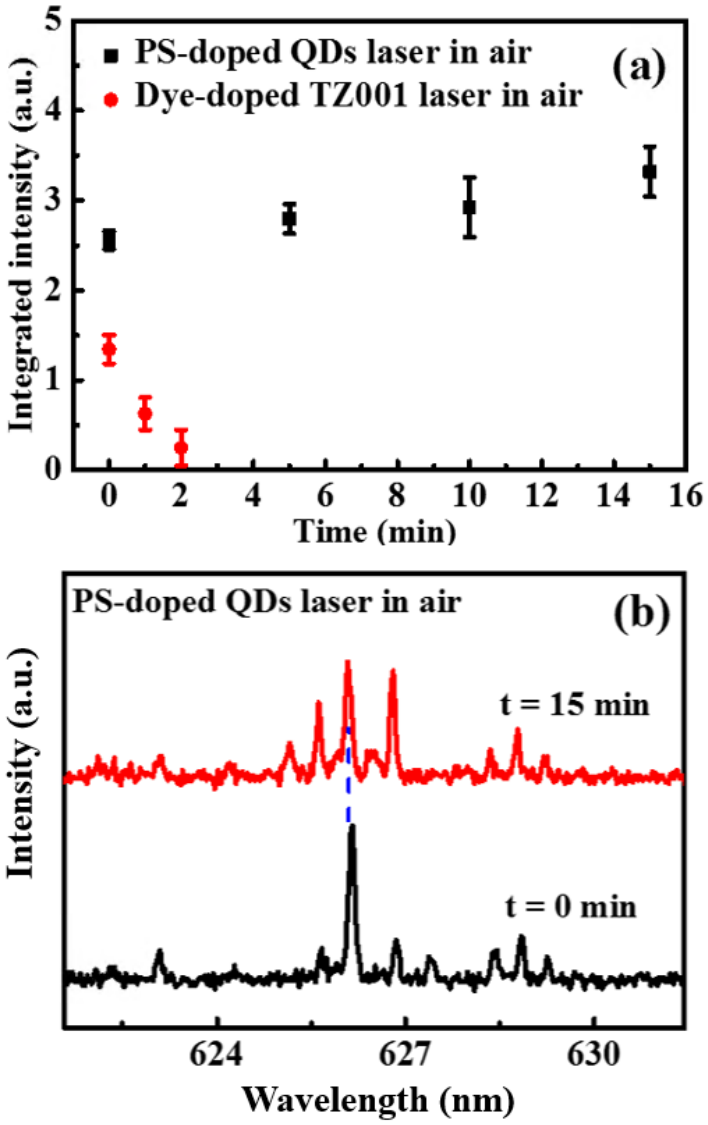

Figure 5.8: (a) The durability of emission intensities overtime of the PS-doped QDs and dye-doped TZ001 lasers in air; (b) The lasing spectrum of the PS-doped QDs laser in air (t = 0 min, t = 15 min)

lution of the lasing wavelengths were monitored in real-time under the aqueous environment under pumping power of 28.3 μJ/mm^2. Figure 5.10 shows the real-time monitoring of lasing spectrum for the PS doped QDs laser fabricated by

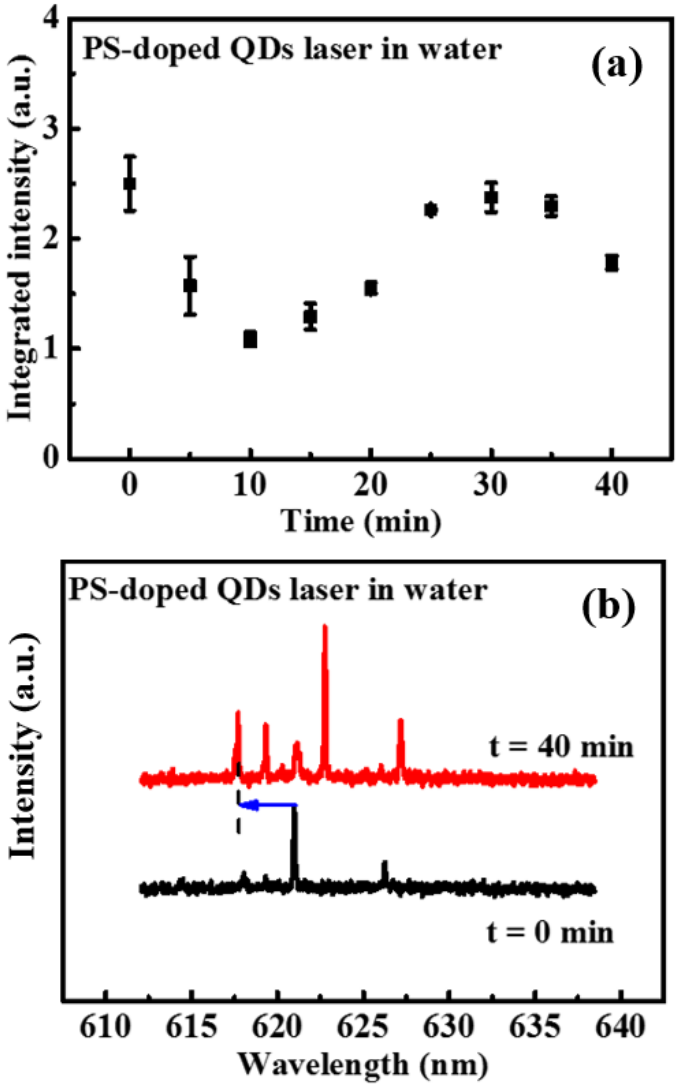

Figure 5.9: (a) The durability of emission intensities overtime of the PS-doped QDs in water; (b) The lasing spectrum of the PS-doped QDs laser in water (t = 0 min, t = 40 min).

the single spin coating process. The monitoring lasted 45 minutes and collected data every one minute. The lasing wavelengths were blue-shifted as time went on. According to the experimental data, it could be concluded that during the whole experiment, the blue shift occurred in our experiment due to water permeating

into the porous quantum dot film. Therefore, the laser wavelength drifts over time to the shorter wavelength range.

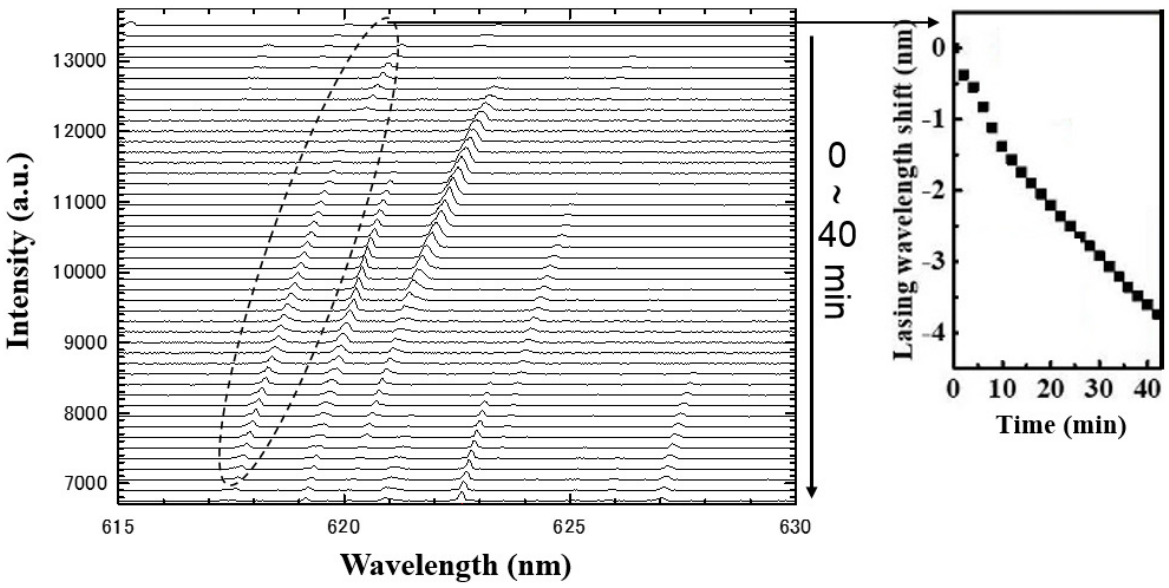

Figure 5.10: The real-time lasing spectrum of the PS-doped QDs microcavity lasers fabricated by the single spin-coating deposition. The insets show the lasing wavelengths shifts.

In order to improve the spectral stability of QDs laser in water, we tried to use another polymer layer to seal the cracks in the QDs microcavity. Herein, to assemble the second polymer layer on the QDs microcavity laser a two-step coating was operated. At the beginning of the experiment, we tried to use pure PS as the sealing layer, but the resolving of QDs cavity from toluene led to no laser emission. Thus, we tried to added a few quantum dots in the sealing layer solution, and varied the doping ratio of quantum dots and PS through experiments until we got the same laser as previous experiments. After the optimization, we chosen the 1 wt.% of PS solution with 15 mg/mL QDs as the sealing layer solution.

Then, the QDs mircocavity laser with sealing layer were characterized the lasing spectrum in real-time under the pumping power of 50.81 μJ/mm^2 which is shown in figure 5.11. Notice that the lasing wavelength was nearly constant within the first 35 minutes of the experiment. It is the reason that the second deposition of nanocomposite film was able to seal most of the cracks in the first film of cavity and prevent liquid penetration, which increased the thickness of the core layer and protected the lasing modes from external aqueous environment. In the whole two-hour experiment, the totally wavelength shift was only about 1 nanometer. This was over 400% of improvement in spectral stability compared to the previous QDs cavity laser without sealing layer (Figure 5.10). Due to the mode competition of other modes, there were a little bit shifts happened around 45 min. The durability of this on-chip QD laser has been demonstrated to be consistently longer than 45 minutes. Therefore, the long durability and spectral stable on-chip QDs microcavity laser was demonstrated by molecularly engineering the QDs gain layer in the microring groove platform.

5.4. Ink-jet printed QDs microdisk lasers

5.4.1 Experiments

There are two challenges to fabricate QDs doped microdisks with ink-jet technology, one is that high viscosity matrix ink may block the nozzle, and the other one is that condensation of QDs reduces fluorescence efficiency. As mentioned in the above chapters, thickness of micrometer order is required for waveguiding visible light. However, a high concentration is required to achieve thick film with linear polymers. The high concentration lead to a high viscosity which is the cause to block micro nozzle. In previous experiments, we used low viscosity

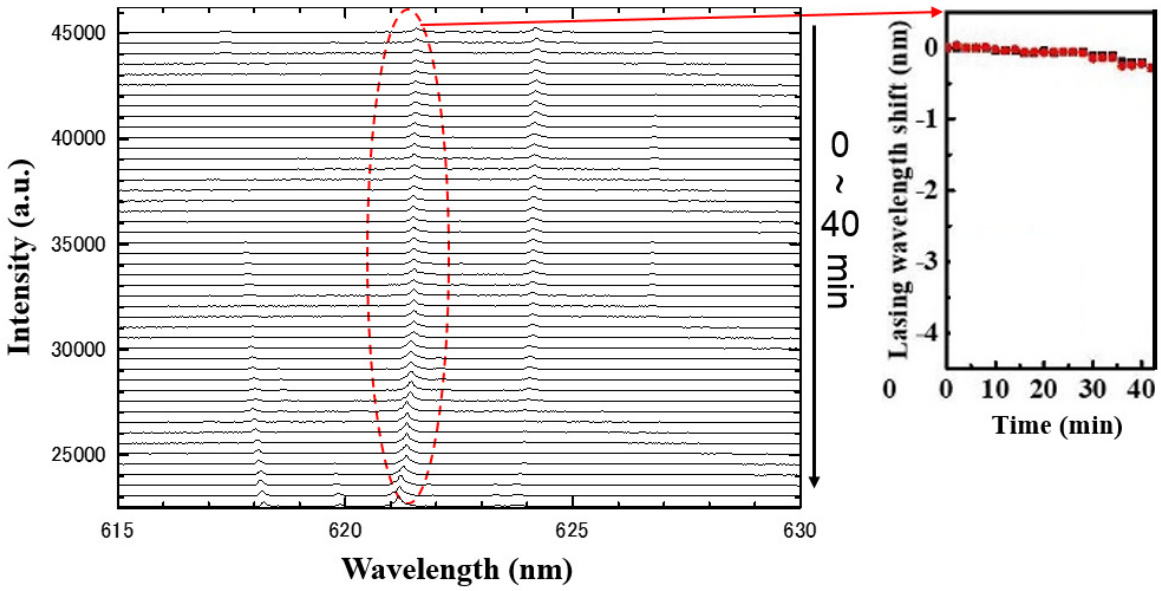

Figure 5.11: The real-time lasing spectrum of the PS-doped QDs microcavity lasers fabricated by the two-step deposition process. The insets show the lasing wavelengths shifts.

hyperbranched polymers as matrix to realize dye doped microdisks with ink-jet technology. In this experiment, it may be necessary to use ordinary linear polymers, because the solvent of QDs is limited. The good news is that QDs can self-assemble microcavities have been reported. This means a high concentration QDs with low concentration matrix has feasibility of realizing microcavity. However, quantum dots still have the possibility of condensation in different materials. In order to investigate the condensation of QDs in different matrix material, we carried out the following experiment. Colloidal CdSe/ZnS core-shell QDs doped polystyrene in various concentration was dropped on slide glass with pipet. After drying, the QDs doped PS film formed on the glass. Figure 5.12 (a) and (b) shows the films of 15 mg/mL QDs doped 10 wt.% PS and 15 mg/mL QDs doped

10 wt.% PS, respectively. Obviously, the condensation of QDs increased with the increasing of PS concentration.

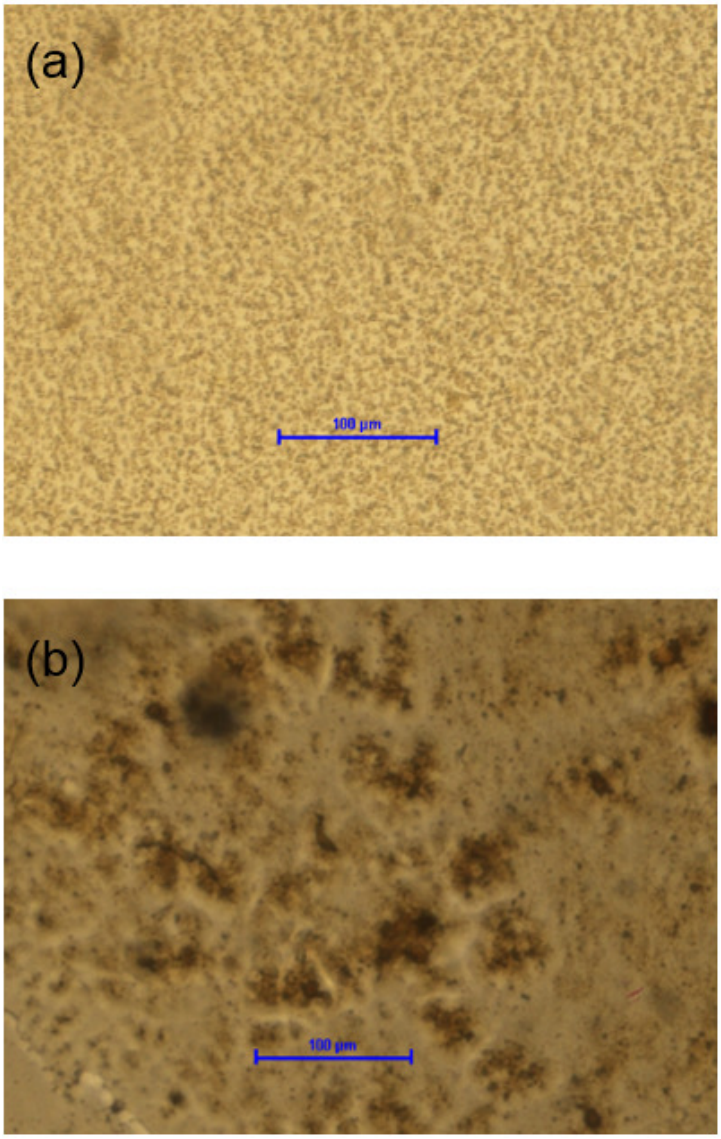

Figure 5.12: (a) 15 mg/mL CdSe/ZnS doped 10 wt.% PS; (a) 15 mg/mL CdSe/ZnS doped 20 wt.% PS.

To further investigate the QDs condensation, colloidal CdSe/ZnS core-shell

QDs doped FZ-001 was also tested. In this test, we did not vary the concentration of PS, we varied the concentration of QDs. Figure 5.13 (a) and (b) shows the films of 15 mg/mL QDs doped 10 wt.% FZ-001 and 1.5 mg/mL QDs doped 10 wt.% FZ-001, respectively. Similar to the above result, the condensation of QDs increased with the decreasing of QDs concentration.

In addition, by comparing the two groups of figures, it is not difficult to find that QDs condensation is more seriously in FZ-001. This is because FZ-001 contains fluorine, which will repel QDs and make it easier to condense between QDs. After the simple test above, the results show that in the QDs doped matrix solution, increasing the concentration of matrix will aggravate the condensation of QDs, and increasing the concentration of QDs will alleviate the condensation of QDs. Therefore, based on the above results, we chose of high concentration QDs doped PS solution to fabricate microdisks.

As mentioned earlier, PS which is a linear polymer will be easy to block micro nozzle with high concentration. However, in order to optimize the concentration of PS, it is necessary to try to fabricate microdisk with high concentration of PS. Thus, we used spray printing method to test different concentrations of PS to make microdisk. The schematic of fabrication is shown in figure 5.14, a dispenser needle (Musashi Eng. NA-27G-B) is mounted on a 5 mL syringe, the solution is rapidly ejected on a FEP substrate after absorbing a small amount of a QDs doped PS solution. As shown in illustration of figure 5.14, a large number of droplets with different shapes and sizes formed films on the substrate. In these films of different sizes, choosing the film with suitable shape and size can be regarded as a microdisk.

The microdisks fabricated with 15 mg/mL QDs doped 10 wt.%, 5 wt.%, 1 wt.%, 0.5 wt.%, and 0 wt.% PS are shown in figure 5.15 (a) ,(c) ,(e) ,(g), and (i), respectively. In the figures, it is obvious that the coffee ring effect is more

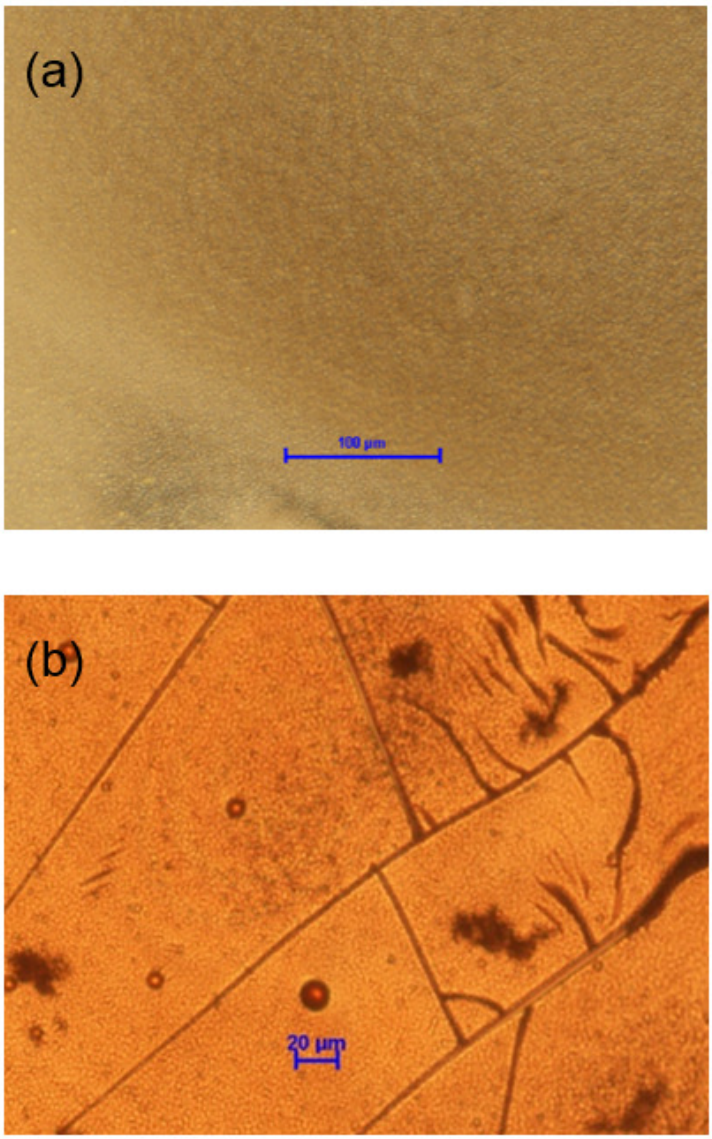

Figure 5.13: (a) 15 mg/mL CdSe/ZnS dope 10 wt.% FZ-001; (b) 1.5 mg/mL CdSe/ZnS dope 10 wt.% FZ-001.

remarkable with the decrease of PS concentration, and the film gradually changes from disk shape to ring shape. To pumping these microdisks for generating laser, the setup in figure 3.3 was used. A passively Q-switched and frequency-doubled

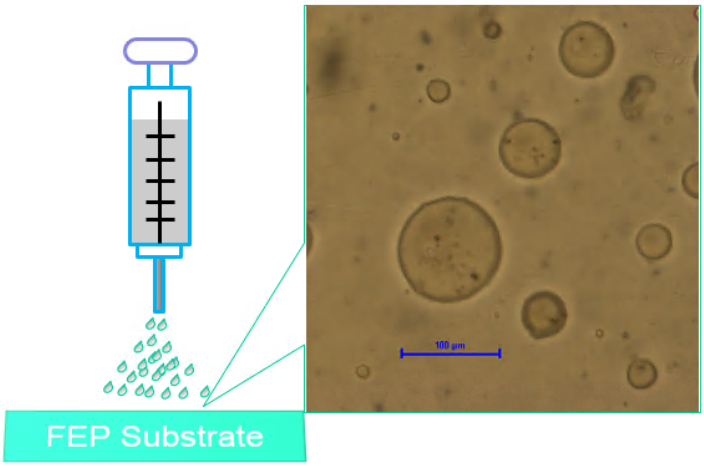

Figure 5.14: Spray printing for fabrication of QDs doped PS microdisks.

Nd:YAG laser were used as a pumping source at 532 nm. The integration shots was 50 shots which the exposure time and pulse Frequency were 1 s and 10 Hz, respectively. Pumping images of microdisks with different concentration of PS are shown in figure 5.15 (b) (d) (f) (h) (j). When the concentration of PS was10 wt.% and 5 wt.%, the fluorescence was very weak and no laser was detected. On the other hand, the laser signal was detected in microdisks with PS concentration of 1 wt.%, 0.5 wt.%, and 0 wt.% PS.

5.4.2 Results and discussion

The lasing spectrum of microdisks with PS concentration of 1 wt.%, 0.5 wt %, and 0 wt.% are shown in figure 5.16. The results are similar to the case of the QDs microrings, the lasing spectrum of the pure QDs disk is very difficult to identify while the WGM lasing peak of QDs doped PS disk is easy to identify. As explained earlier, these messy modes in pure QDs microdisk are partly originated from the scattering of rough sidewalls of the pure QDs microcavity, and the cracked

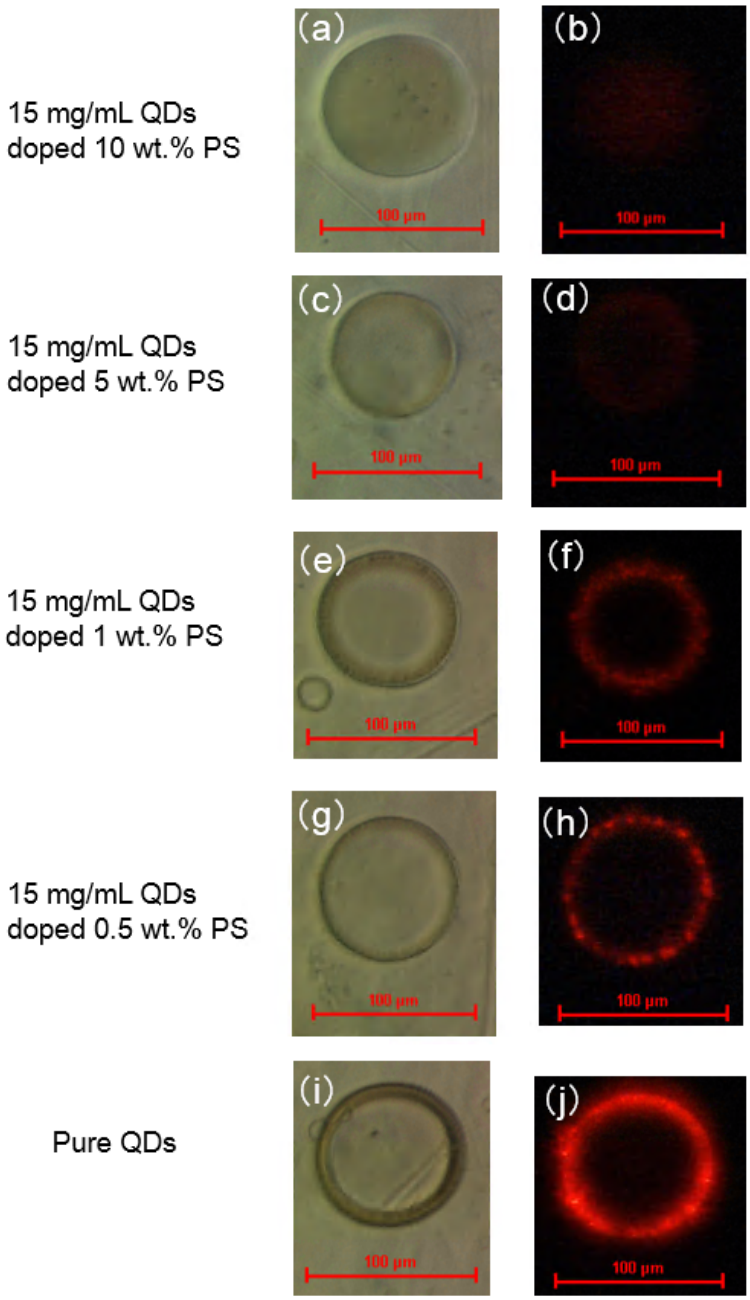

Figure 5.15: (a) (c) (e) (g) (i) Microdisks with different concentration of PS; (b) (d) (f) (h) (j) Pumping images of microdisks with different concentration of PS.

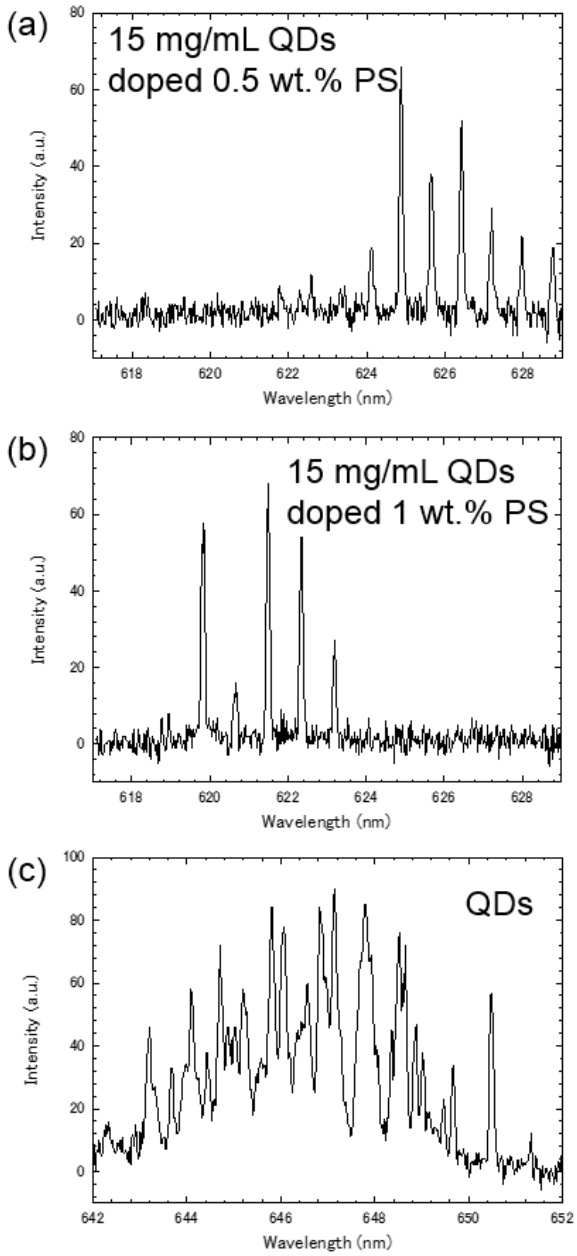

Figure 5.16: Lasing spectrum of (a) 15 mg/mL QDs doped 1 wt.% PS microdisk; (b) 15 mg/mL QDs doped 0.5 wt.% PS microdisk; (c) pure QDs microdisk.

QDs film due to the high concentration also introduced undesired scatterings. In addition, the lasing resonance spectra appear at longer wavelength bands with the decrease of PS concentration. This is because the refractive index of quantum dots is much larger than that of PS. The refractive index of the cavity increases when PS concentration decreases, hence lasing spectrum moves to longer wavelength.

The input-output characteristics of each microdisks can be obtained by changing the pump power as shown in figure 5.17. The lasing threshold of 15 mg/mL QDs doped 1 wt.% PS microdisk, 15 mg/mL QDs doped 0.5 wt.% PS microdisk, and pure QDs microdisk were 14.1 μJ/mm^2, 3.5 μJ/mm^2, and 0.86 μJ/mm^2, respectively. The result show that the threshold of the microdisk decreases with the decrease of PS concentration.

This is because the concentration ratio of QDs increases when the concentration of PS decreases, it is easier to achieve laser due to the higher gain concentration. In addition, the refractive index of the cavity increases when PS concentration decreases, higher RI cavity is easier to block the light inside of cavity. All of the results with excitation state in microdisks are shown in table 5.1.

Table 5.1: The excitation state in microdisks with different PS concentration.

Concentration of materials	Lasing threshold	Lasing wavelength range	Spectral identification
15 mg/mL QDs doped 1 wt.% PS	14.1 μJ/mm^2	618∼624 nm	Clear
15 mg/mL QDs doped 0.5 wt.% PS	3.5 μJ/mm^2	624∼630 nm	Clear
Pure QDs	0.86 μJ/mm^2	642∼651 nm	Messy

Since then, the relations between PS concentration and microdisk lasing state has been clarified. Fortunately, WGM lasing can be realized at 1wt.% PS concen-

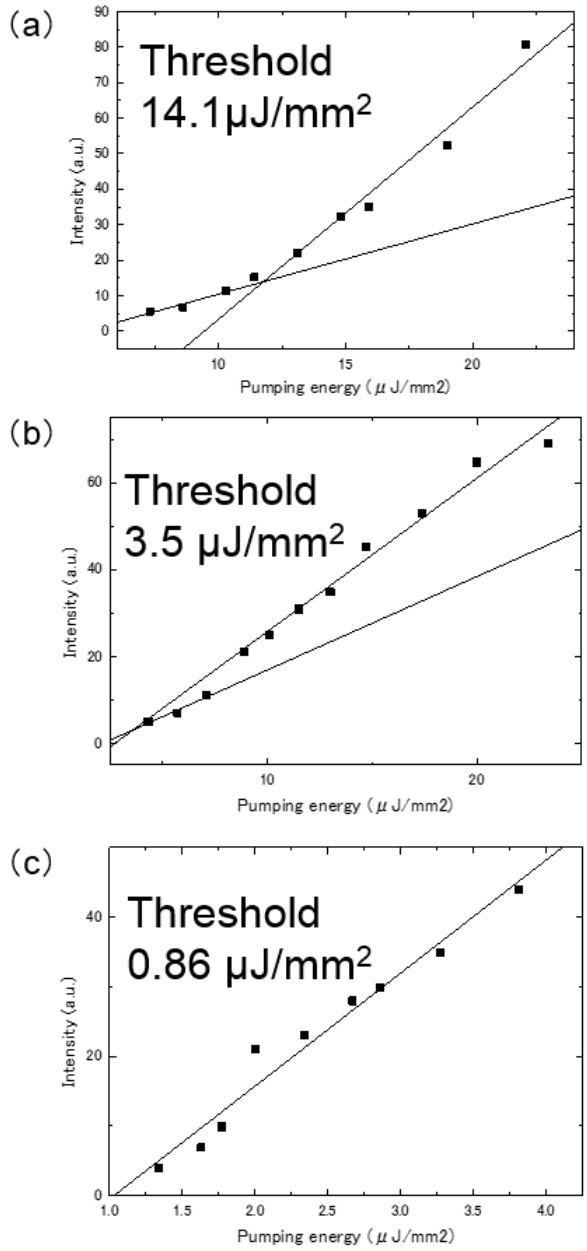

Figure 5.17: Input-output characteristic of (a) 15 mg/mL QDs doped 1 wt.% PS microdisk; (b) 15 mg/mL QDs doped 0.5 wt.% PS microdisk; (c) pure QDs microdisk.

tration. This low concentration of polymer can be printed with ink-jet technology. As shown in figure 5.18, a microdisk was printed on a FEP substrate by using a micro nozzle (Cluster Technology CO., LTD., PIJD-1) with inner diameter of 60 m. The ink of microdisk was 15 mg/mL QDs doped 1 wt.% PS solution(solvent: toluene). The printing condition parameters of voltage, cycle, delay, width, temperature and humidity were set as 6.9 V, 90 Hz, 0.357 ms, 20 μs, 24$^{\circ}C$ and 43 %, respectively. After drying, a fine microdisk can be obtained as shown in figure 5.19(a). Under the appropriate pumping power, WGM lasing can be obtained as shown in 5.19(b), and the lasing spectrum is shown in 5.19(c). Obviously, the clear WGM lasing peak can be found in the spectrum. Therefore, we demonstrated a QDs doped PS microdisk with ink-jet printing method. It is note that this demonstration shows ink-jet printed WGM microdisks can be achieved with ordinary polymers.

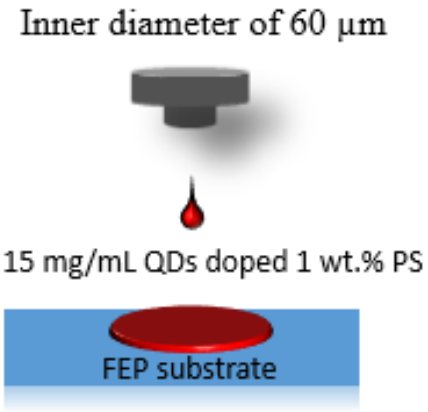

Figure 5.18: Fabrication of ink-jet printed QDs doped microdisks.

After completing the above experiments, on the one hand, we verified that the anomalous dispersion is not enough to explain the spectral shifts, on the other hand, we have successfully fabricated QDs doped microcavity without dye

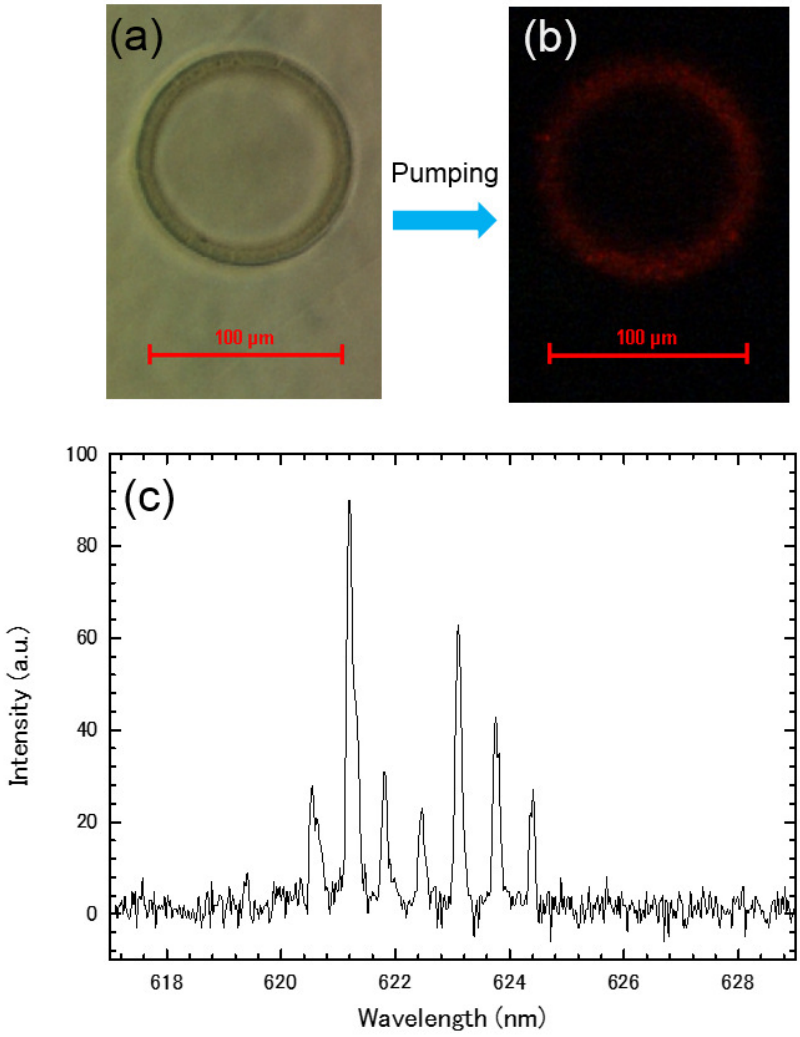

Figure 5.19: (a) Ink-jet printed QDs doped microdisk; (b) Lasing image of ink-jet printed QDs doped microdisk; (c) Lasing spectrum of ink-jet printed QDs doped microdisk.

degradation. To further investigate the cause of spectral shifts from excitation power, a QDs doped microdisk is fabricated with ink-jet printing method as shown in figure 5.18.

A lasing spectrum of a QDs doped microdisk can be obtained when we change the excitation power. As it shown in figure 5.20, there is still a significant shift

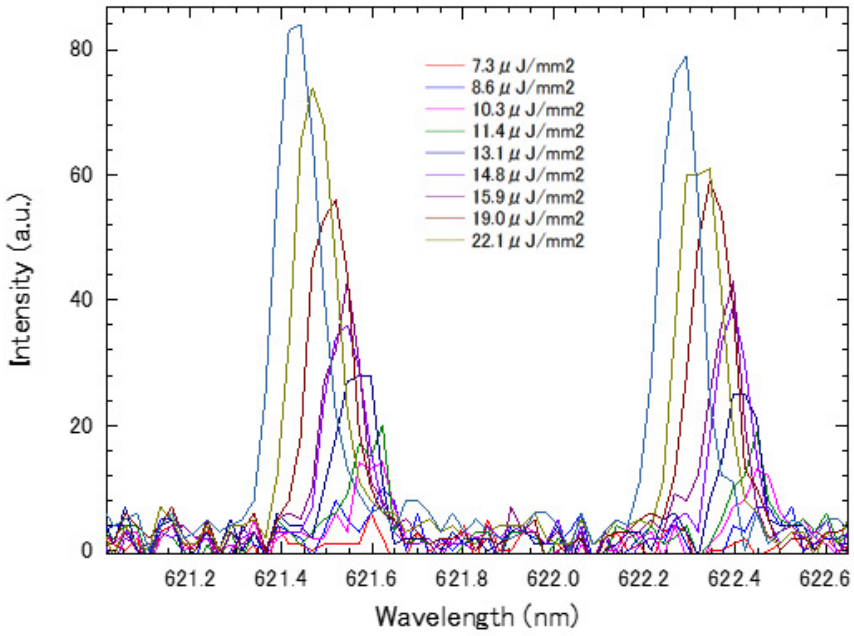

Figure 5.20: Lasing spectral shift in QDs doped microdisk with different excitation power.

occurred when we decreased the excitation power. Combined with the previous experimental results, it is not difficult to infer that this shift has other cause in addition to the anomalous dispersion and dye degradation. Based on the results above, we assumed that the shift was caused by a larger optical gain move the WGM field to slightly insider radially when the intensity was increased. To prove this the assumption, Oxborrow's model with PMLs modified by Cheema was adopted to accurately calculate the eigenfrequencies of modes using the FEM in COMSOL software. In this simulation, effects of gain was added to investigate. Actually, when the excitation intensity increases, the number of excitons increases, which means the gain increases. Only the qualitative research was implemented in this simulation because it is very difficult to accurately calculate the gain. , the specific parameters are not important. For convenience, the model of figure

2.11 was used without modification because it is a qualitative research. Although this calculation model can't import the number of excitons, we changed the gain by changing the refractive index of the cavity. As we know, the total refractive index in a cavity can be expressed as:

$$n_{tol} = n - N^* i + N_{loss} i \tag{5.5}$$

where n is the RI of cavity material, N^* is related to gain, and N_{loss} is related to loss. The simulation result in a 14° angle disk is shown in figure 5.21, the spatial position of WGWM is moving to inside of cavity with the increasing of gain. Compared to the result above, the simulation result in a 89° angle disk is shown in figure 5.22, there is almost no moving of WGWM spatial position even the gain increased. The simulation results proved that the spectral shift origins from WGWM spatial modification under the exactly same excitation condition, and the modification was caused by interaction between the sharpened-edge with increased the optical gain.

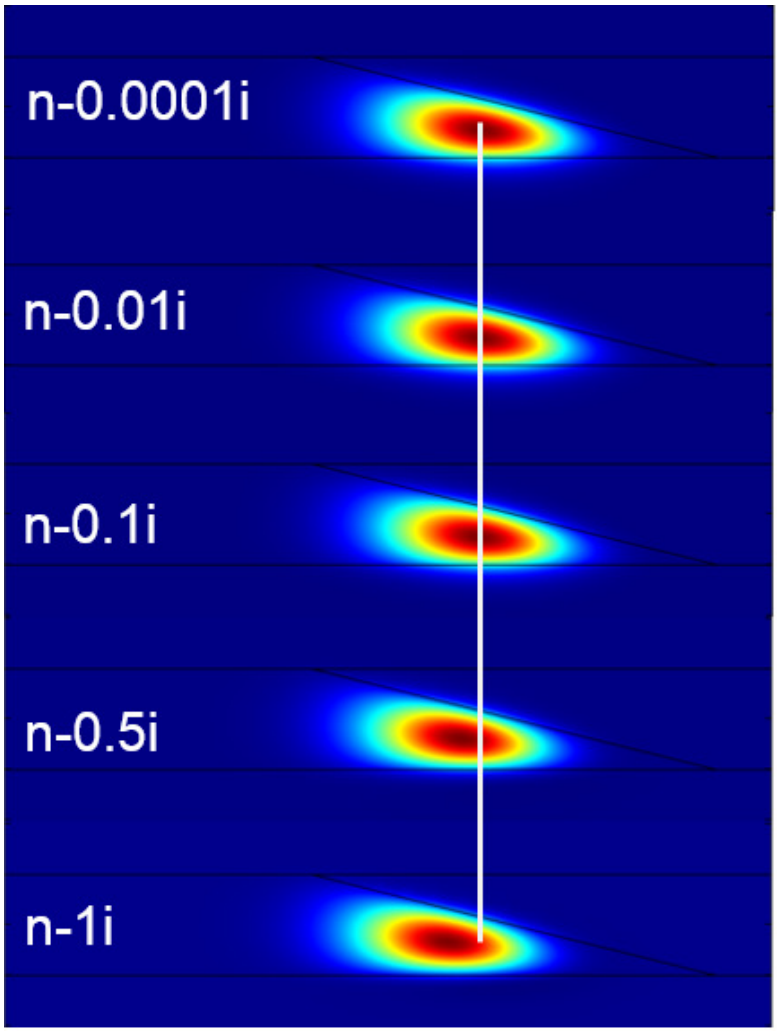

Figure 5.21: Eigenfrequencies of WGWM in a microdisk (14° edge angle)under different excitation power.

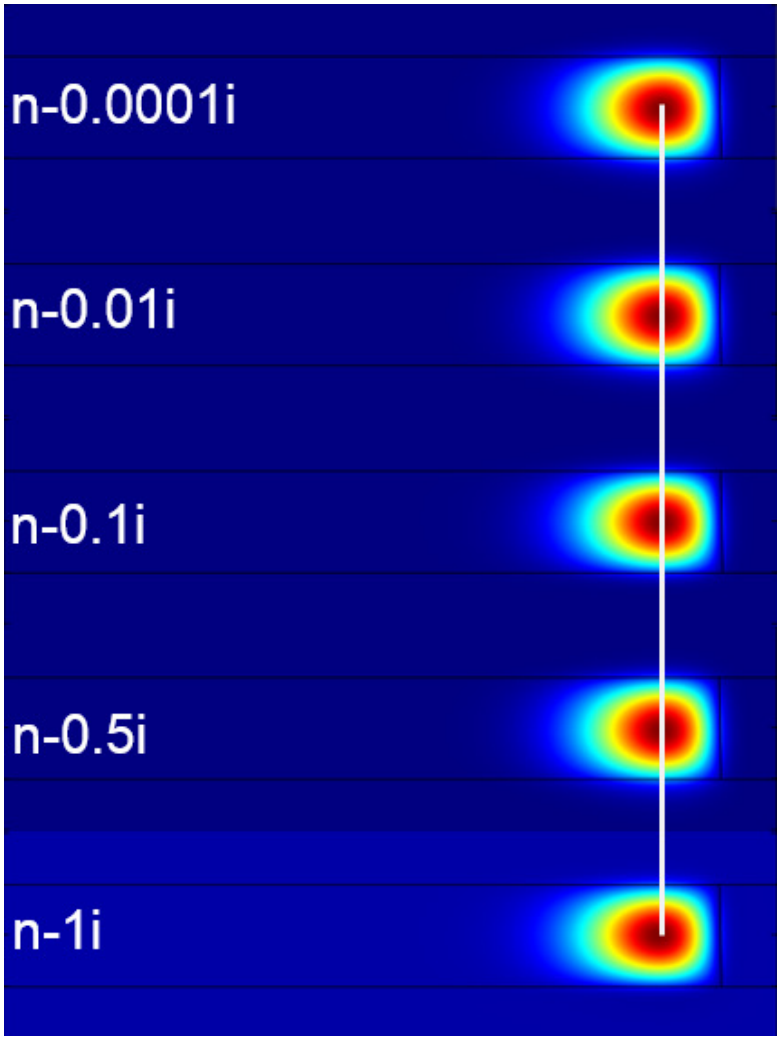

Figure 5.22: Eigenfrequencies of WGWM in a microdisk (89° edge angle)under different excitation power.

5.5. Summary

In this chapter, it was demonstrated by a numerical simulation that the WGWM spatial position moves to the inside of the cavity with the increasing of the gain when the WGWM is unbalanced in the sidewall loss. Firstly, the results of experiment and calculation show that the anomalous dispersion is not enough to cause such a large spectral shift. Secondly, a long-durability on-chip QDs microring laser by virtue of the annular groove etched in the fused-silica substrate was realized, and a long-durability ink-jet printed QDs doped polymeric microdisk was realized. The lasing spectrum of the QDs microdisk still had blue shifts with the increasing of excitation intensity even no effects of dye degradation is exist. Finally, we have successfully demonstrated that the spectral shift origins from WGWM spatial modification with the changing of excitation power, and the modification was caused by interaction between the sharpened-edge with increased the optical gain. We believe that this phenomenon can not only help us better understand the nature of WGWM in active cavity, but also make it possible to control the spatial position of WGWM. If the WGWM spatial location can be controlled, more applications will be realized, especially the sensing applications, because controlling the WGWM spatial position can help to reveal more evanescent field.

Chapter 6

Conclusion

6.1. Achievements

In this thesis, the author demonstrated that the spatial position of WGWM could be moved by some effects of several external factors. The effects of edge angles on the spatial position of WGWM were theoretically demonstrated with ink-jet printed microdisk lasers. Based on the above results, a normal WGM reconfigurable microring for high sensitive temperature sensing was demonstrated, and a WGWM ink-jet printed microdisk sensor for absorption of protein was realized. On the other hand, the effects of gain intensity on spatial position of WGWM was demonstrated by experiments of QDs doped microdisk and numerical simulation.

In chapter 3, the effects of edge angles on WGWM in an ink-jet printed microdisk were demonstrated. The LDS798 doped and Rhodamine590 doped microdisk lasers were realized by ink-jet method with the lasing threshold of 2.80 μJ/mm^2 and 2.00 μJ/mm^2, respectively. To explore the causes of lasing wavelength shifts, two disks with different edge angles are experimentally fabricated, and the WGWM field distributions were numerically simulated. As a result, the

spatial position of WGWM moved to inside of disk along the radius direction, and the TM mode moved more significantly than the TE mode.

In chapter 4, a high sensitive temperature sensor with a reconfigurable WGM microring and a non-specific biosensing with a printable WGWM microdisk were demonstrated by lithography groove platform and ink-jet method, respectively. For the temperature sensors, both the R6G-doped SU-8 and R6G-doped TZ-001 WGWM polymer microring lasers were used. The lasing threshold of R6G-doped SU-8 and R6G-doped TZ-001 WGWM polymer microring lasers were 1.28 μJ/mm^2 and 9.28 μJ/mm^2, respectively. The sensitivities of the temperature sensors based on SU-8 ring and TZ-001 ring were 228.6 pm/$^\circ C$ and 85.8 pm/$^\circ C$ in the range of 31$\sim$43 $^\circ C$, respectively. The temperature resolutions of SU-8 ring and TZ-001 ring were 0.13 $^\circ C$ and 0.35 $^\circ C$, respectively. Based on the result of microring sensor, it was proved that the TZ-001 based active microcavity laser can be easily applied for sensor. For the non-specific biosensing, an ink-jet printed R6G doped microdisk successfully detected the BSA solution with a concentration of 100 ppm, and the absorption of BSA molecular with thickness of 10$\sim$15 nm could be calculated. This result not only confirmed that ink-jet printed disk can be used as a non-specific biosensor, but also gave the feasibility of using ink-jet printed disk as a specific sensor.

In the chapter 5, the effects of gain intensity on spatial position of WGWM in an ink-jet printed microdisk were theoretically demonstrated. The spectral shift could be due to anomalous dispersion, effect of gain intensity on spatial position and dye degradation. Firstly, the influence of anomalous dispersion was eliminated by theoretical calculation. Secondly, QDs doped long-durability WGWM microcavities have been successfully developed to eliminate the interference of spectral shifts caused by degradation of dyes. Finally, we successfully verified that the spatial position of WGWM moves inside of disk with the gain intensity

increases by combining the lasing spectral of ink-jet printed QDs microdisk and numerical simulation.

In conclusion, the achievements of this thesis come from three aspects: the effects of cavity edge angle and the gain on spatial position of WGWM, WGWM sensor, and long-durability active WGWM microcavities.

6.2. Future prospects.

As mentioned in section 6.1 the achievements of this thesis are the effects of external factors on spatial position of WGWM, high sensitive sensors, and long-durability QDs doped WGWM microcavities.

For the achievement based on the effects of cavity edge angle and the gain on spatial position of WGWM, it provides feasibility for controlling of spatial position of WGWM. If the spatial position of WGWM can be controlled freely in the future, a sensitivity tunable device can be realized by controlling of evanescent field. In addition, this technology also helps the mode coupling by control the WGWM position.

For the achievement based on WGWM sensor, it provides simple solutions for future advanced sensing applications. Although this thesis realized a non-specific sensor for detecting protein adsorption by ink-jet printed WGWM microdisk, the adsorption thickness of nanometer order proves that this method is feasible to develop as a specific sensor. For example, ink-jet printing technology makes it easy to achieve the specific antigen-antibody sensing by replacing antigen-antibody materials since ink is changeable. In addition, the fabrication condition at room temperature and atmospheric pressure also ensures that biomaterials will not be inactivated.

For the achievement based on long-durability QDs doped WGWM microcavi-

ties, it expands the potential of active WGM cavity applications. QDs dope WGM lasers have a long lifetime due to the absence of photobleaching, so it can be applied to a continuous wave (CW) laser. On the other hand, many sensing required long time and real time sensors. Such long-time and real-time sensor is usually realized by passive cavity, but now the development of QDs doped WGWM lasers makes it possible for active cavity to realize long-term real-time sensing.

In conclusion, this thesis achievement is that for the first time the author discovered that the spatial position of WGWM (a special WGM in a microdisk with a sharp edge) is highly sensitive to external factors, and the mechanism has been analyzed and verified by experiment and simulation. This thesis clarified the knowledge for the spatial control of WGWM, it shows a feasibility that various applications with controllable mode spatial position or tunable physical properties can be realized by using optimized acute edge WGWM microcavities. It can be said that it shows important knowledge about future advanced application based on microdisk laser.

Acknowledgements

First and foremost, I would like to thank my supervisor, Prof. Yuji Oki for his guidance and support in these 5 years. Prof. Yuji Oki not only gave me excellent guidance in science, but also in my life and career. His experience and knowledge have always helped me to overcome difficulties and move forward. I learned a lot of knowledge and abilities from him that I could use all my life. From now on, I will try harder to be a person who can make him proud.

I would also like to thank my thesis committee members: Prof. Kenshi Hayashi, Prof. Kazutoshi Kato and Associate Professor Daisuke Nakamura, for thoughtful comments and questions on my thesis. With the help of their suggestions, I not only improved my thesis, but also learned a lot of knowledge.

I would also like to thank Assistant Professor Hiroaki Yoshioka for his guidance and support in experiment and papers. With his help, I not only grasped the ability to design experiments, but also learned to write academic papers.

I would also like to thank all the members in Oki lab including Previous and present members. In particular, I would like to thank Jifeng Li for his contribution to the experiment of sensor part in my thesis. Thanks to Fan Yang and Zhikun Wu for their help in my first year at Kyushu University, and thanks to Tomoya Ota for his teaching in ink-jet fabrication. Besides, I would also like to thank the present members, K. T. Abdul Nasir and Junfeng Zhu, for their experimental help.

I would also like to thank students, staff and all person related to the Leading program of “Advanced Graduate Course on Molecular Systems for Devices” in Kyushu University. With the help of the Leading program, I learned not only the scientific knowledge of other majors, but also the leadership and management abilities.

I would also like to thank Prof. L.Jay Guo for his host and guidance when I was in University of Michigan. I would also like to thank Dr. Lei Wan, Dr. Hengky Chandrahalim and Jian Zhou for their academic help.

I would also like to thank my Japanese teacher, Xiaohong Shi, for guidance on my career. With his help, I learned Japanese and came to study in Japan. He laid the foundation for all my knowledge and abilities.

Last but not least, I would like to thank my family members. I am very grateful to my grandmother, Xuefen Hua, for bringing me up. Although she is gone, I believe she can see my growth. I will not let her down. I am also very grateful to my parents, Hong Chen and Huoxiang Jiang, for giving me life, education and upbringing. I would also like to thank my aunt, Ling Chen, for raising and educating me as her own son. I will try harder to make her proud of me. Thanks to my brothers, Chao Chen and Biao Zhang, for all the support. Finally, I would like to thank my wife, Na Zhang, for her support and patience in these 6 years. During my PhD study, her meticulous care relieved me a lot of pressure. Without her help, it would be difficult for me to persevere.

I appreciate all my friends and family who have helped me. I will continue to strive to become an outstanding contributor to the world at an early date.

Acronyms

AFM	Atomic force microscope
ASE	Amplified spontaneous emission
BSA	Bovine serum albumin
FEP	Tetrafluoroethylene-hexafluoropropylene copolymer
F-factor	Finesse factor
FWHM	Full width at half maximum
LASER	Light amplification by stimulated rmission of radiation
MASER	Microwave amplification by stimulated radiation
ND filter	Neutral density filter
OPO	Optical parameter oscillator
PET	Polyethylene terephthalate
PML	Perfect matched layer
PS	Polystyrene
Q-factor	Quality factor
QDs	Quantum dots
R6G	Rhodamine 6G
RI	Refractive index
SEM	Scanning electron microscope
WGM	Whispering-gallery mode
WGWM	Whispering-gallery wedge mode

References

[1] A. Einstein, " Zur Quantentheorie der Strahlung," Physikalische Zeitschrift **18**, 121-128 (1917).

[2] J. Gordon, H. Zeiger, and C. Townes, " The Maser-New Type of Microwave Amplifier, Frequency Standard, and Spectrometer," Phys. Rev. **99**(4), 1264 (1955).

[3] A. Schawlow and C. Townes, " Infrared and Optical Masers," Phys. Rev. **112**(6), 1940-1949 (1958).

[4] K. Shimoda, T. Wang, and C. Townes, " Further Aspects of the Theory of the Maser," Phys. Rev. **102**(5), 1308-1321 (1956).

[5] T. H. Maiman, " Stimulated Optical Radiation in Ruby," Nature **187**, 493-494 (1960).

[6] T. H. Maiman, " Stimulated Optical Emission in Fluorescent Solids I: Theoretical Considerations," Phys. Rev. **123**(4), 1145-1150 (1961).

[7] T. H. Maiman, R. H. Hoskins, I. J. D'Haenens, C. K. Asawa, and V. Evtuhov, " Stimulated Optical Emission in Fluorescent Solids II: Spectroscopy and Stimulated Emission in Ruby," Phys. Rev. **123**(4), 1151-1157 (1961).

[8] G. Kotik and M. C. Newstein, " Theory of laser oscillations in Fabry-Perot resonators," J. Appl. Phys. **32**(2), 178-186 (1961).

[9] W. Streifer, " On the integral equation for Fabry-Perot interferometer modes," Phys. Lett. **18**(2), 118-119 (1965).

[10] S. R. Barone, " Resonances of the Fabry-Perot etalon," J. Appl. Phys. **34**(4), 831-843 (1963).

[11] L. Rayleigh, " The Problem of the Whispering Gallery," Phil. Mag. **20**(120), 1001-1004 (1910).

[12] L. Rayleigh, " Further applications of Bessel's functions of high order to the Whispering Gallery and allied problems," Phil. Mag. **27**(157), 100-109 (1914).

[13] G. Mie, " Beitrge zur Optik trber Medien, speziell kolloidaler Metallsungen," Annalen der Physik **330**(3), 377-445 (1908).

[14] P. Debye, " Der Lichtdruck auf Kugeln von beliebigem Material," Annalen der Physik **335**(11), 57-136 (1909).

[15] A. N. Oraevsky, " Whispering-gallery waves," Quantum Electron **32**(5), 377-400 (2002).

[16] K. J. Vahala, " Optical microcavities," Nature **424**, 839-846 (2003).

[17] T. M. Benson, S. V. Boriskina, P. Sewell, A. Vukovic, S. C. Greedy, and A. I. Nosich " Micro-optical resonators for microlasers and integrated opto-electronics," Frontiers in Planar Lightwave Circuit Technology **216**, 39-70 (2006).

[18] L. He, S. K. Ozdemir, and L. Yang, " Whispering gallery microcavity lasers," Laser Photonics Rev. **7**(1), 60-82 (2013).

[19] Y. Yamamoto and R. E. Slusher, " Optical Processes in Microcavities," Physics Today **46**(6), 66-73 (1993).

[20] A. B. Matsko, A. A. Savchenkov, D. Strekalov, V. S. Ilchenko, and L. Maleki, " Review of Applications of Whispering-Gallery Mode Resonators in Photonics and Nonlinear Optics," The Interplanetary Network Progress Report **42**(162), 1-51 (2005).

[21] Estel Green, " The Story of Q," (1985).

[22] R. Paschotta, " Q factor," Encyclopedia of Laser Physics and Technology. RP Photonics, (2008).

[23] R. Henriet, P. Salzenstein, D. Ristic, A. Coillet, M. Mortier, A. Rasoloniaina, K. Saleh, G. Cibiel, Y. Dumeige, M. Ferrari, Y. K. Chembo, O. Llopis, and P. Fron, " High quality-factor optical resonators," Phys. Scr., T162, 014032 (2014).

[24] A. A. Savchenkov, M. L. Gorodetsky and V. S. Ilchenko, " Ultimate Q of optical microsphere resonators," Opt. Lett. **21**(7), 453-455 (1996).

[25] T. Baer, " Continuous-wave laser oscillation in a Nd:YAG sphere," Opt. Lett. **12**(6), 392-394 (1987).

[26] Y. Z. Wang, B. L. Lu, Y. Q. Li, and Y. S. Liu, " Observation of cavity quantum-electrodynamic effects in a Nd:glass microsphere," Opt. Lett. **20**(7), 770-772 (1995).

[27] W. Bogaerts, P. De Heyn, T. Van Vaerenbergh, K. De Vos, S. Kumar Selvaraja, T. Claes, P. Dumon, P. Bienstman, D. Van Thourhout and R. Baets, " Silicon microring resonators," Laser Photonics Rev. **6**(1), 47-73 (2012).

[28] W. Bogaerts, R. Baets, P. Dumon, V. Wiaux, S. Beckx, D. Taillaert, B. Luyssaert, J. V. Campenhout, P. Bienstman, and D. V. Thourhout, " Nanophotonic Waveguides in Silicon-on-Insulator Fabricated With CMOS Technology," J. Lightwave Technol. **23**(1), 401-412 (2005).

[29] J. Heebner, V. Wong, A. Schweinsberg, R. Boyd, and D. Jackson, " Optical transmission characteristics of fiber ring resonators," IEEE J. Quantum Electron. **40**(6), 726-730 (2004).

[30] Z. Tian, C. Chen, and D. V. Plant, " Single- and dual-wavelength fiber ring laser using fiber microdisk resonator," IEEE Photon. Technol. Lett. **22**(22), 1644-1646 (2010).

[31] T. Grossmann, S. Schleede, M. Hauser, T. Beck, M. Thiel, G. Freymann, T. Mappes, and H. Kalt, " Direct laser writing for active and passive high-q polymer microdisks on silicon," Opt. Express **19**(12), 11451-11456 (2011).

[32] T. Grossmann, M. Hauser, T. Beck, C. Gohn-Kreuz, M. Karl, H. Kalt, C. Vannahme, and T. Mappes, " High-q conical polymeric microcavities," Appl. Phys. Lett. **96**(1), 013303 (2010).

[33] S. M. Spillane, T. J. Kippenberg, and K. J. Vahala, " Ultralow-threshold raman laser using a spherical dielectric microcavity," Nature **415**, 621-623 (2002).

[34] T. Grossmann, S. Klinkhammer, M. Hauser, D. Floess, T. Beck, C. Vannahme, T. Mappes, U. Lemmer and H Kalt, " Strongly confined, low-

threshold laser modes in organic semiconductor microgoblets," Opt. Express **19**(10), 10009-10016 (2011).

[35] A. Tulek, D. Akbulut, and M. Bayindir, " Ultralow threshold laser action from toroidal polymer microcavity," Appl. Phys. Lett. **94**(20), 203302 (2009).

[36] J. Pfeifle, V. Brasch, M. Lauermann, Y. Yu, D. Wegner, T. Herr, K. Hartinger, P. Schindler, J. Li, D. Hillerkuss, R. Schmogrow, C. Weimann, R. Holzwarth, W. Freude, J. Leuthold, T. J. Kippenberg, and C. Koos, " Coherent terabit communications with microresonator Kerr frequency combs," Nature photonics **8**, 375-380 (2014).

[37] S. Reinhardt, G. Saathoff, H. Buhr, L. A. Carlson, A. Wolf, D. Schwalm, S. Karpuk, C. Novotny, G. Huber, M. Zimmermann, R. Holzwarth, T. Udem, T. W. Hnsch and G. Gwinner, "Test of relativistic time dilation with fast optical atomic clocks at different velocities," Nature Physics **3**, 861-864 (2007).

[38] Q. Li, X. Chen, J. Song, M. Bi, M. Hu, and S. Li, " Time delay in double micro-ring resonator with grating," Optics Communications **376**(1), 6-13 (2016).

[39] T. Barwicz, M. A. Popovic, P. T. Rakich, M. R. Watts, H. A. Haus, E. P. Ippen, and H. I. Smith, " Microring-resonator-based add-drop filters in SiN: fabrication and analysis," Opt. Express **12**(7), 1437-1442 (2004).

[40] F. Vollmer and S. Arnold, " Whispering-gallery-mode biosensing: label-free detection down to single molecules," Nature methods **5**, 591-596 (2008).

[41] R. Boyd and J. E. Heebner, " Sensitive disk resonator photonic biosensor," Appl. Opt. **40**(31), 5742-5747 (2001).

[42] J. Yang and L. J. Guo, " Optical sensors based on active microcavities," IEEE J. Quantum Electron. **12**(1), 143-147 (2006).

[43] S.-Y. Cho and N. M. Jokerst, " A polymer microdisk photonic sensor integrated onto silicon," IEEE Photon. Technol. Lett. **18**(20), 2096-2098 (2006).

[44] V. Lefvre-Seguin, "Whispering-gallery mode lasers with doped silica microspheres," Opt. Mater. **11**(2-3), 153-165 (1999).

[45] D. K. Armani, T. J. Kippenberg, S. M. Spillane, and K. J. Vahala, " Ultra-high-Q toroid microcavity on a chip," Nature **421**, 925-928 (2003).

[46] C. Y. Chao and L. J. Guo, " Polymer microring resonators fabricated by nanoimprint technique," J. Vac. Sci. Technol. B **20**(6), 2862 (2002).

[47] D. Nakamura, N. Tetsuyama, T. Shimogaki, Y. Sato, Y. Mizokami, M. Higashihata, and T Okada, " Optical Characterization of ZnO Microsphere Produced by Laser Ablation in Air," Journal of Laser Micro Nanoengineering **10**(2), 162-165 (2015).

[48] H. Yoshioka, T. Ota, C. Chen, S. Ryu, K. Yasui, and Y. Oki, " Extreme ultra-low lasing threshold of fullpolymeric fundamental microdisk printed with room temperature atmospheric ink-jet technique," Sci. Rep. **5**, 10623 (2015).

[49] H. Chandrahalim, and X. Fan, " Reconfigurable solid-state dye-doped polymer ring resonator lasers," Sci. Rep. **5**, 18310 (2015).

[50] H. Chandrahalim, S. C. Rand, and X. Fan, " Fusion of Renewable Ring Resonator Lasers and Ultrafast Laser Inscribed Photonic Waveguides," Sci. Rep. **6**, 32668 (2016).

[51] I. H. Agha, J. E. Sharping, M. A. Foster, and A. L. Gaeta, " Optimal sizes of silica microspheres for linear and nonlinear optical interactions," Appl. Phys. B **83**(2), 303-309 (2006).

[52] H. Lee, T. Chen, J. Li, K. Y. Yang, S. Jeon, O. Painter, and K. J. Vahala, " Chemically etched ultrahigh-Q wedge-resonator on a silicon chip," Nature Photonics **6**, 369-373 (2012).

[53] C. Chen, S. Ryu, H. Yoshioka, K. Yasui, and Y. Oki, Low-threshold lasing from organic and polymeric microdisk printed by room temperature atmosphere ink-jet technique", Proc. SPIE **9360**, 936007 (2015).

[54] C. Chen, L. Wan, H. Chandrahalim, J. Zhou, H. Zhang, S. Cho, T. Mei, H. Yoshioka, H. Tian, N. Nishimura, X. Fan, L. J. Guo, and Y. Oki, " The effects of edge inclination angles on whispering-gallery modes in printable wedge microdisk lasers," Opt. Express **26**(1), 233241 (2018).

[55] L. Wan, H. Chandrahalim, C. Chen, Q. S. Chen, T. Mei, Y. Oki, N. Nishimura, L. J. Guo, and X. D. Fan, " On chip, high-sensitivity temperature sensors based on dye-doped solid-state polymer microring lasers," Appl. Phys. Lett. **111**(6), 061109 (2017).

[56] C. Chen, J. Li, S. Mitsui, S. Ryu, Y. Mikami, N. Nishimura, H. Yoshioka, and Y. Oki, " Investigation of protein adsorption for biosensors based on ink-jet printed active microdisk resonator," presented at CLEO/Europe-EQEC 2017, Munich, Germany, 25-29 June 2017.

[57] C. Chen, Jifeng Li, Soichiro Ryu, Hiroaki Yoshioka, Masaaki Ozawa, and Y. Oki, " Spectroscopic behavior in whispering-gallery modes by edge formation of printed microdisk lasers" , Proc. SPIE **9668**, 96685J (2015).

[58] L. Wan, H. Chandrahalim, J. Zhou, Z. Li, C. Chen, S. Cho, H. Zhang, T. Mei, H. Tian, Y. Oki, N. Nishimura, X. Fan, and L. J. Guo, " Demonstration of versatile whispering-gallery micro-lasers for remote refractive index sensing," Opt. Express **26**(5), 5800-5809 (2018).

[59] C. Chen, J. Yuan, L. Wan, H. Chandrahalim, Z. Chen, N. Nishimura, H. Takeda, H. Yoshioka, W. Liu, Y. Oki, X. Fan, and Z. Li, " Demonstration of on-chip quantum dot microcavity lasers in a molecularly engineered annular groove," Opt. Lett. **44**(3), 495-498 (2019).

[60] B.E.A.Saleh and M.C.Teich, " Fundamentals of Photonics (Second Edition)," John Wiley & Sons, Inc. publishing (1991).

[61] T. Grossmann, " Whispering-Gallery Mode Lasing in Polymeric Microcavities," Doctoral Thesis, Karlsruher Institut fur Technologie(KIT) (2012).

[62] J. D. Jackson, " Classical Electrodynamics (Third Edition)," John Wiley & Sons, Inc. publishing (1999).

[63] K. Stelmaszczyk, P. Rohwetter, M. Fechner, M. Queier, A. CzySewski, T. Stacewicz, and L. Wste, " Cavity Ring-Down Absorption Spectrography based on filament-generated supercontinuum light," Opt. Express **17**(5), 3673-3678 (2009)

[64] T. Ling, " High-Q Optical Micro-cavity Resonators as High Sensitive Biochemical and Ultrasonic Sensors," Doctoral Thesis, University of Michigan (2012).

[65] M. Borselli, T. J. Johnson, and O. Painter, " Beyond the Rayleigh scattering limit in high-Q silicon microdisks: theory and experiment," Opt. Express **13**(5), 1515-1530 (2005).

[66] I. S. Grudinin, V. S. Ilchenko, and L. Maleki, " Ultrahigh optical Q factors of crystalline resonators in the linear regime," Phys. Rev. A **74**(6), 063806 (2006).

[67] D. Marcuse, " Bending Losses of the Asymmetric Slab Waveguide," The Bell System Technical Journal **50**, 2551-2563 (1971).

[68] M. L. Gorodetsky, A. A. Savchenkov, and V. S. Ilchenko, " Ultimate Q of optical microsphere resonators," Opt. Lett. **21**(7), 453-455 (1996).

[69] M. H. Bitarafan and R.G. DeCorby, " On-Chip High-Finesse Fabry-Perot Microcavities for Optical Sensing and Quantum Information," Sensors **17**(8), 1748 (2017).

[70] N. Okada and J. B. Cole, " Simulation of whispering gallery modes in the Mie regime using the nonstandard nite-dierence time domain algorithm," J. Opt. Soc. Am. B **27**(4), 631-639 (2010)

[71] M. Oxborrow, " Traceable 2-D nite element simulation of the whispering gallery modes of axisymmetric electromagnetic resonators," IEEE Trans. on Microwave Theory Tech. **55**(6), 12091218 (2007).

[72] M. Oxborrow, " How to simulate the whispering-gallery modes of dielectric microresonators in FEMLAB/COMSOL," Proc. SPIE **6452**, 64520J (2007).

[73] M. I. Cheema and A. G. Kirk, " Accurate determination of the quality factor and tunneling distance of axisymmetric resonators for biosensing applications," Opt. Express **21**(7), 8724-8735 (2013)

[74] M. I. Cheema, and A. G. Kirk. " Implementation of the perfectly matched layer to determine the quality factor of axisymmetric resonators in COMSOL," in COMSOL conference, Boston, Oct 8 2010.

[75] X. Jiang, C. Yang, H. Wu, S. Hua, L. Chang, Y. Ding, Q. Hua, and M. Xiao, " On-Chip Optical Nonreciprocity Using an Active Microcavity," Sci. Rep. **6**, 38972 (2016).

[76] L. He, . K. zdemir, J. Zhu, and L. Yang, " Ultrasensitive detection of mode splitting in active optical microcavities," Phys. Rev. A **82**(5), 053810 (2010).

[77] S. Krmmer, S. Rastjoo, T. Siegle, S. F. Wondimu, C. Klusmann, C. Koos, and H. Kalt, " Size-optimized polymeric whispering gallery mode lasers with enhanced sensing performance," Opt. Express **25**(7), 7884-7894 (2017).

[78] B. Peng, S. K. zdemir, F. Lei, F. Monifi, M. Gianfreda, G. L. Long, S. Fan, F. Nori, C. M. Bender, and L. Yang, " Paritytime-symmetric whispering-gallery microcavities," Nature Physics **10**, 394-398 (2014).

[79] H. Hodaei, M. A. Miri, M. Heinrich, D. N. Christodoulides, and M. Khajavikhan, " Parity-time-symmetric microring lasers," Science **346**(6212), 975-978 (2014).

[80] J. Yang and L. J. Guo, " Optical sensors based on active microcavities," IEEE J. Sel. Top. Quantum Electron. **12**(1), 143-147 (2006).

[81] R. Schilling, H. Schtz, A. H. Ghadimi, V. Sudhir, D. J. Wilson, and T. J. Kippenberg, " Near-field integration of a SiN nanobeam and a SiO2 microcavity for heisenberg-limited displacement sensing," Phys. Rev. Appl. **5**(5), 054019 (2016).

[82] E. Gavartin, P. Verlot, and T. J. Kippenberg, " A hybrid on-chip optomechanical transducer for ultrasensitive force measurements," Nature Nanotechnology **7**, 509-514 (2012).

[83] M. Haraguchi, T. Hirai, M. Ozawa, K. Miyaji and K. Tanaka, " Hydrophobic acrylic hard coating by surface segregation of hyper-branched polymers," Applied Surface Science **266**, 235-238 (2013).

[84] D. Gandolfi, F. Ramiro-Manzano, F. J. Aparicio-Rebollo, M. Ghulinyan, G. Pucker, and L. Pavesi, " Role of edge inclination in an optical microdisk resonator for label-free sensing," Sensors **15**(3), 4796-4809 (2015).

[85] J. Ward and O. Benson, " WGM microresonators: sensing, lasing and fundamental optics with microspheres, Laser Photonics Rev. **5**(4), 553-570 (2011).

[86] L. Viveros, S. Paliwal, D. McCrae, J. Wild, and A. Simonian, " A fluorescence-based biosensor for the detection of organophosphate pesticides and chemical warfare agents," Sensors and Actuators B: Chemical **115**(1), 150-157 (2006).

[87] X. Fan, I. M. White, S. I. Shopova, H. Zhu, J. D. Suter, and Y. Sun, " Sensitive optical biosensors for unlabeled targets: A review," Analytica Chimica Acta **620**(1-2), 8-26 (2008).

[88] L. C. Clark and C. Lyons. " Electrode systems for continuous monitoring in cardiovascular surgery," Annals of the New York Academy of sciences **102**,29-45 (1962).

[89] D. Grieshaber, R. MacKenzie, J. Vrs, and E. Reimhult, " Electrochemical biosensors-sensor principles and architectures," Sensors **8**(3), 1400-1458 (2008).

[90] C. R. Lowe, " Biosensors," Trends in biotechnology **2**(3), 59-65 (1984).

[91] W.-C. Law, P. Markowicz, K.-T. Yong, I. Roy, A. Baev, S. Patskovsky, A. V. Kabashin, H.-P. Ho, and P. N. Prasad, " Wide dynamic range phase-sensitive

surface plasmon resonance biosensor based on measuring the modulation harmonics," Biosensors and Bioelectronics **23**(5), 627-632 (2007).

[92] Y. S. Skibina, V. V. Tuchin, V. I. Beloglazov, G. Shteinmaeer, I. L. Betge, R. Wedell, and N. Langhoff, " Photonic crystal bres in biomedical investigations," Quantum Electronics **41**(4),284-301 (2011).

[93] F. Vollmer, D. Braun, and A. Libchaber, " Protein detection by optical shift of a resonant microcavity," Appl. Phys. Lett. **80**(21), 4057-4059 (2002).

[94] S. M. Grist, S. A. Schmidt, J. Flueckiger, V. Donzella, W. Shi, S. T. Fard, J. T. Kirk, D. M. Ratner, K. C. Cheung, and L. Chrostowski, " Silicon photonic micro-disk resonators for label-free Biosensing," Opt. Express **21**(7), 7994-8006 (2013).

[95] M. A. Santiago-Cordoba, S. V. Boriskina, F. Vollmer, and M. C. Demirel, "Nanoparticle-based protein detection by optical shift of a resonant microcavity," Appl. Phys. Lett. **99**(7), 073701(2011).

[96] J. P. Laine, B. E. Little, D. R. Lim, H. C. Tapalian, L. C. Kimerling, and H. A. Haus, " Microsphere resonator mode characterization by pedestal anti-resonant reflecting waveguide coupler," IEEE Photonics Technol. Lett. **12**(8), 1004-1006 (2000).

[97] V. S. Ilchenko, X. S. Yao, and L. Maleki, " Pigtailing the high-Q microsphere cavity: a simple fiber coupler for optical whispering-gallery modes," Opt. Lett. **24**(11), 723-725 (1999).

[98] Y. L. Pan and R. K. Chang, " Highly efficient prism coupling to whispering gallery modes of a square -cavity," Appl. Phys. Lett. **82**(4), 487-489 (2003).

[99] Z. Guo, H. Quan, and S. Pau, " Near-field gap effects on small microcavity whispering-gallery mode resonators," J. Phys. D Appl. Phys. **39**(24), 5133-5136 (2006).

[100] C. Zhao, Q. Yuan, L. Fang, X. Gan, and J. Zhao, " High-performance humidity sensor based on a polyvinyl alcohol-coated photonic crystal cavity," Opt. Lett. **41**(23), 5515-5518 (2016).

[101] K. Kosma, G. Zito, K. Schuster, and S. Pissadakis, " Whispering gallery mode microsphere resonator integrated inside a microstructured optical fiber," Opt. Lett. **38**(8), 1301-1303 (2013).

[102] Z. P. Liu, X. F. Jiang, Y. Li, Y. F. Xiao, L. Wang, J. L. Ren, S. J. Zhang, H. Yang, and Q. H. Gong, " High-Q asymmetric polymer microcavities directly fabricated by two-photon polymerization," Appl. Phys. Lett. **102**(22), 221108 (2013).

[103] H. L. Liu, Y. Y. Fan, J. H. Wang, Z. S. Song, H. Shi, R. C. Han, Y. L. Sha, and Y. Q. Jiang, " Intracellular Temperature Sensing: An Ultra-bright Luminescent Nanothermometer with Non-sensitivity to pH and Ionic Strength," Sci. Rep. **5**, 14879 (2015).

[104] F. Vetrone, R. Naccache, A. Zamarron, A. J. de la Fuente, F. S. Rodriguez, L. M. Maestro, E. M. Rodriguez, D. Jaque, J. G. Sole, and J. A. Capobianco, " Temperature Sensing Using Fluorescent Nanothermometers," ACS Nano **4**(6), 3254-3258 (2010).

[105] Y. Y. Huang, T. Guo, Z. Tian, B. Yu, M. F. Ding, X. P. Li, and B. O. Guan, " Nonradiation Cellular Thermometry Based on Interfacial Thermally Induced Phase Transformation in Polymer Coating of Optical Microfiber," ACS Appl. Mater. Interfaces **9**(10), 9024-9028 (2017).

[106] J. G. Zhu, S. K. Ozdemir, Y. F. Xiao, L. Li, L. He, D. R. Chen, and L. Yang, " On-chip single nanoparticle detection and sizing by mode splitting in an ultrahigh-Q microresonator," Nature Photonics **4**, 46-49 (2010).

[107] C. Zhang, T. Ling, S. L. Chen, and L. J. Guo, " Ultrabroad Bandwidth and Highly Sensitive Optical Ultrasonic Detector for Photoacoustic Imaging," ACS Photonics **1**(11), 1093-1098 (2014).

[108] C Zhang, S. L. Chen, T. Ling, and L. J. Guo, " Imprinted Polymer Microrings as High-Performance Ultrasound Detectors in Photoacoustic Imaging," IEEE J. Lightwave Technol. **33**(20), 4318-4328 (2015).

[109] B. Peng, S. K. Ozdemir, F. C. Lei, F. Monifi, M. Gianfreda, G. L. Long, S. H. Fan, F. Nori, C. M. Bender, and L. Yang, " Paritytime-symmetric whispering-gallery microcavities," Nature Physics **10**, 394-398 (2014).

[110] C. Zhang, H. Subbaraman, Q. C. Li, Z. Y. Pan, J. G. Ok, T. C. Ling, J. Chung, X. Y. Zhang, X. H. Lin, R. T. Chen, and L. J. Guo, " Printed photonic elements: nanoimprinting and beyond," J. Mater. Chem. C **4**(23), 5133-5153 (2016).

[111] L. H. Yu, Y. L. Yin, Y. C. Shi, D. X. Dai, and S. L. He, " Thermally tunable silicon photonic microdisk resonator with transparent graphene nanoheaters," Optica **3**(2), 159-166 (2016)

[112] Y. G. Zhang and Y. C. Shi, " Temperature insensitive lower-index-mode photonic crystal nanobeam cavity," Opt. Lett. **40**(2), 264-267 (2015).

[113] B. Ozel, R. Nett, T. Weige, G. Schweiger, and A. Ostendorf, " Temperature sensing by using whispering gallery modes with hollow core fibers," Meas. Sci. Technol. **21**(9), 094015 (2010).

[114] G. D. Kim, H. S. Lee, C. H. Park, S. S. Lee, B. T. Lim, H. K. Bae, and W. G. Lee, " Silicon photonic temperature sensor employing a ring resonator manufactured using a standard CMOS process," Opt. Express **18**(21), 22215-22221 (2010)

[115] M. S. Kwon and W. H. Steier, " Microring-resonator-based sensor measuring both the concentration and temperature of a solution," Opt. Express **16**(13), 9372-9377 (2008).

[116] H. Xu, M. Hafezi, J. Fan, J. M. Taylor, G. F. Strouse, and Z. Ahmed, " Ultra-sensitive chip-based photonic temperature sensor using ring resonator structures," Opt. Express **22**(3), 3098-3104 (2014)

[117] L. Zhou, K. Okamoto, and S. J. B. Yoo, " Athermalizing and Trimming of Slotted Silicon Microring Resonators With UV-Sensitive PMMA Upper-Cladding," IEEE Photonics Technol. Lett. **21**(17), 1175-1177 (2009).

[118] B. Guha and J. Cardenas, and M. Lipson, " Athermal silicon microring resonators with titanium oxide cladding," Opt. Express **21**(22), 26557-26563 (2013).

[119] J. Teng, P. Dumon, W. Bogaerts, H. Zhang, X. Jian, X. Han, M. Zhao, G. Morthier, and R. Baets, " Athermal Silicon-on-insulator ring resonators by overlaying a polymer cladding on narrowed waveguides," Opt. Express **17**(17), 14627-14633 (2009).

[120] Y. G. Zhang, P. H. Liu, S. L. Zhang, W. X. Liu, J. Y. Chen, and Y. C. Shi, " High sensitivity temperature sensor based on cascaded silicon photonic crystal nanobeam cavities," Opt. Express **24**(20), 23037-23043 (2016).

[121] B. B. Li, Q. Y. Wang, Y. F. Xiao, X. F. Jiang, Y. Li, L. X. Xiao, and Q. H. Gong, " On chip, high-sensitivity thermal sensor based on high-Q polydimethylsiloxane-coated microresonator, " Appl. Phys. Lett. **96**(25), 251109 (2010).

[122] J. C. Knight, G. Cheung, F. Jacques, and T. A. Birks, " Phase-matched excitation of whispering-gallery-mode resonances by a fiber taper," Opt. Lett. **22**(15), 1129-1131 (1997).

[123] V. M. Lauschke, C. D. Tsiairis, P. Francois, and A. Aulehla, " Scaling of embryonic patterning based on phase-gradient encoding," Nature **493**, 101-105 (2013).

[124] L. Gounaridis, P. Groumas, E. Schreuder, R. Heideman, H. Avramopoulos, and C. Kouloumentas, " New set of design rules for resonant refractive index sensors enabled by FFT based processing of the measurement data," Opt. Express **24**(7), 7611-7632 (2016).

[125] J. T. Li, Y. Lin, J. F. Lu, C. X. Xu, Y. Y. Wang, Z. L. Shi, J. Dai, " Single Mode ZnO Whispering-Gallery Submicron Cavity and Graphene Improved Lasing Performance," ACS Nano **9**(7), 6794-6800 (2015).

[126] Z. H. Liu, L. Liu, Z. D. Zhu, Y. Zhang, Y. Wei, X. N. Zhang, E. M. Zhao, Y. X. Zhang, J. Yang, and L. B. Yuan, " Whispering gallery mode temperature sensor of liquid microresonastor," Opt. Lett. **41**(20), 4649-4652 (2016).

[127] L. Dong, L. Liu, F. Ye, A. Chughtai, S. Popov, A. T. Friberg, and M. Muhammed, " Photostability of lasing process from water solution of Rhodamine 6G with gold nanoparticles," Opt. Lett. **37**(1), 34-36 (2012).

[128] "Fluorescence Microscopy Interactive TutorialsPhotobleaching,"Retrieved from http://micro.magnet.fsu.edu/primer/java/fluorescence/photobleaching/

[129] C. Dang, J. Lee, C. Breen, J. S. Steckel, and S. Coe-Sullivan, " Red, green and blue lasing enabled by single-exciton gain in colloidal quantum dot films," Nature Nanotechnology **7**, 335-339 (2012).

[130] P. T. Snee, Y. H. Chan, D. G. Nocera, and M. G. Bawendi, " Whispering-gallery-mode lasing from a semiconductor nanocrystal/microsphere resonator composite, " Adv. Mater. **17**(9), 1131-1136 (2005).

[131] B. Min, S. Kim, K. Okamoto, L. Yang, A. Scherer, H. Atwater, and K. Vahala, " Ultralow threshold on-chip microcavity nanocrystal quantum dot lasers," Appl. Phys. Lett. **89**(19), 191124 (2006).

[132] B. L. Feber, F. Prins, E. D. Leo, F. T. Rabouw, and D. J. Norris, " Colloidal-quantum-dot ring lasers with active color control," Nano Lett. **18**(2), 1028-1034 (2018).

[133] Y. Wang, V. D. Ta, K. S. Leck, B. H. Tan, Z. Wang, T. He, C. D. Ohl, H. V. Demir, and H. D. Sun, " Robust whispering-gallery-mode microbubble lasers from colloidal quantum dots," Nano Lett. **17**(4), 2640-2646 (2017).

[134] Y. Wang, K. E. Fong, S. C. Yang, V. D. Ta, Y. Gao, Z. Wang, V. Nalla, H. V. Demir, and H. D. Sun, " Unraveling the ultralow threshold stimulated emission from CdZnS/ZnS quantum dot and enabling high-Q microlasers," Laser Photonics Rev. **9**(5), 507-516 (2015).

[135] K. X. Rong, C. W. Sun, K. B. Shi, Q. H. Gong, and J. J. Chen, " Room-temperature planar lasers based on water-dripping microplates of colloidal quantum dots," ACS Photonics **4**(7), 1776-1784 (2017).

[136] A. Kiraz, Q. S. Chen, and X. D. Fan, " Optofluidic lasers with aqueous quantum dots," ACS Photonics **2**(6), 707-713 (2015).

[137] S. Pang, R. E. Beckham, and K. E. Meissner, " Quantum dot-embedded microspheres for remote refractive index sensing," Appl. Phys. Lett. **92**(22), 221108 (2008).

[138] C. Gollner, J. Ziegler, L. Protesescu, D. N. Dirin, R. T. Lechner, G. Fritz-Popovski, M. Sytnyk, S. Yakunin, S. Rotter, A. A. YousefiAmin, C. Vidal, C. Hrelescu, T. A. Klar, M. V. Kovalenko, and W. Heiss, " Random lasing with systematic threshold behavior in films of CdSe/CdS," core/thick-shell colloidal quantum dots, ACS Nano **9**(10), 9792-9801 (2015).

[139] C. Y. Cheng and M. H. Mao," Photo-stability and time-resolved photoluminescence study of colloidal CdSe/ZnS quantum dots passivated in Al_2O_3 using atomic layer deposition, " J. Appl. Phys. **120**(8), 083103 (2016).